國立交通大學

機械工程學系

博士論文

低溫電漿平行化流體程式的發展及其應用

Development of a Parallelized Fluid Modeling Code and Its Applications in Low-temperature Plasmas

研究生：洪捷粲

指導教授：吳宗信博士

西元　2010　年　七　月

低溫電漿平行化流體程式的發展及其應用

Development of a Parallelized Fluid Modeling Code and Its Applications in Low-temperature Plasmas

研 究 生 ： 洪捷粲　　Student: Chieh-Tsan Hung

指 導 教 授 ： 吳宗信博士　　Advisor: Dr. Jong-Shinn Wu

國 立 交 通 大 學

機 械 工 程 學 系

博 士 論 文

A Thesis

Submitted to Department of Mechanical Engineering

National Chiao Tung University

in Partial Fulfillment of the Requirements

for the Degree of

Doctor of Philosophy

in

Mechanical Engineering

July 2010

Hsinchu, Taiwan

西元2010年七月

低溫電漿平行化流體程式的發展及其應用

學生：洪捷粲　　指導教授：吳宗信博士

國立交通大學機械工程學系

摘　　要

本論文研究目的是發展與驗證一個平行化一維/一維軸對稱/二維/二維軸對稱低溫非熱平衡電漿流體模型程式，數值方法主要是使用Fully-Implicit有限差分法以及混和解析解與數值解的Jacobian矩陣，論文將詳細介紹模擬的實作方式。此程式可以廣泛的應用在各種不同的氣壓以及不同的功率輸入頻率(從百萬赫茲射頻到數千赫茲的交流電壓)。模擬的結果將會與實驗結果驗證比較，並且討論其中的電漿物理與化學。

本研究主要可以分成三部份。第一部份，建立並且驗證一個平行化一維/一維軸對稱/二維/二維軸對稱低溫非熱平衡電漿流體模型程式。程式中使用的流體模型是由波茲曼方程式出發，推導出包含所有粒子的連續方程式、所有帶電粒子則使用Drift-Diffusion近似的動量方程式以及電子的能量方程式。Poisson方程式則用來解析空間中的電位分佈。所有的待定變數都經過無因次化，並且使用完全耦合的 Newton-Krylov-Schwarz (NKS) 演算法將方程式離散。其中，Overlapping additive Schwarz 方法被使用來作為 preconditioner，而 Bi-CGStab 及 GMRES 方法被使用來解析線性方程式矩陣。一系列使用氦氣與氮氣以及不同輸入頻率的一維電漿模擬結果與本研究室的實驗結果相互驗證。二維的GEC氦氣電漿模擬結果也與文獻中的實驗數據與數值解析結果互相驗證。平行程式的效率測試則是使用國立中央大學的 V'ger cluster system (Xeon 3GHz dual-core dual-CPU)作為測試平台。測試結果顯示，在使用144個處理器的狀況下，平行效率還可以達到超線性。而最好的平行計算組合是使用LU分解法preconditioner，搭配 GMRES 方法解析線性矩陣。

論文的第二部份：主要是利用第一部份所發展的平行化流體模型程式來研究氦氣DBD在輸入一個變形正弦波下的研究。研究中我們選用了兩組不同氦氣電漿反應方程式，模擬並驗證比較不同的實驗結果。結果顯示使用較為複雜的氦氣電漿反方程式可以如實地得到與實驗接近的計算結果。根據模擬的結果發現電漿在驅動的過程中經歷了複雜的模式轉換：從 long secondary Townsend like 到 dark current like, 接著 short

primary Townsend like 以及類 short secondary Townsend like。

論文的第三部份：主要是模擬研究通入混合著氫氣與矽烷的電漿輔助化學氣相沉積電漿源。為了減少計算耗費的時間，模擬中是用了多尺度時間方法分別處理電子、離子與中性粒子的時間進行。模擬所需要的背景氣體密度分佈以及溫度分佈則是引用一個有限體積法 Navier-Stokes 解析所計算的結果作為電漿模擬的初始條件。氫氣與矽烷的電漿總共使用了15種不同的粒子並引用28個電漿反應方程式。結果顯示SiH_3是最主要的帶矽自由基，結果與文獻相符合。在假設表面反應site的比率為0.015的狀況下，我們可以成功的計算出符合實驗結果的沈積速率與均勻度。

除了總結論文的研究結果之外，同時在論文最後章節亦條列出建議未來應進行研究的研究部分。

關鍵字：電漿; 流體模型; 有限差分法; 平行化; 電漿輔助化學氣相沉積; 介電質放電

Development of a Parallelized Fluid Modeling Code and Its Applications in Low-temperature Plasmas

Student: Chieh-Tsan Hung Advisor: Dr. Jong-Shinn Wu

Submitted to Department of Mechanical Engineering
National Chiao Tung University

ABSTRACT

Development of parallelized 1D/1D-axisymmetric and 2D/2D-axisymmetric fluid modeling codes using fully implicit finite-difference method with hybrid analytical-numerical Jacobian evaluation for low-temperature, non-equilibrium plasma simulation has been reported in this thesis. Implementation and validations against earlier simulations and experimental data are described in detail. Applications with wide range of pressures and frequencies (radio frequency in mega Hertz and alternating current in kilo Hertz) are demonstrated, compared with experimental data wherever possible, and related plasma physics and chemistry are discussed therein. Research in this thesis is divided into three major phases, which are briefly described in the following in turn.

In the first phase, parallelized 1D/1D-axisymmetric and 2D/2D-axisymmetric fluid modeling codes based on distributed memory framework were developed and verified. Fluid modeling equations, resulting from the velocity moments of Boltzmann equation, include continuity equations for all species, momentum equations with drift-diffusion approximation for all charged species, diffusion approximation for neutral species, energy density equation for electrons and Poisson's equation for electrostatic potential distribution. All model equations were nondimensionalized and discretized using fully coupled Newton-Krylov-Schwarz (NKS) algorithm, in which the overlapping additive Schwarz method and Bi-CGStab/GMRES scheme were used as the preconditioner and linear matrix equation solver, respectively. An atmospheric 1D helium dielectric barrier discharge (DBD) (driven by 13.56 MHz and 20 KHz power sources) and an atmospheric nitrogen 1D DBD (driven by 60 KHz power source) are simulated and validated by excellent agreement of discharged currents with experimental results obtained in our laboratory. In addition, a 2D-axisymmetric RF driven GEC chamber with helium discharge (capacitively

coupled plasma) was simulated and the results agree reasonably well with previously reported experimental data. Then, parallel performance of the fluid modeling code was investigated using the same GEC case, which was simulated on a PC cluster system (V'ger cluster system with Xeon 3GHz dual-core dual-CPU, the Center for Computational Geophysics, National Central University, Taiwan.) up to 144 processors. The parallel performance showed superlinear speedup up to 144 processors with the GMRES as the matrix solver combining with LU as the preconditioner.

In the second phase, a one-dimensional helium DBD driven by 20 KHz distorted sinusoidal voltages was investigated in detail using the developed fluid modeling code. Effect of selecting plasma chemistry on simulations of helium DBD was investigated by comparing simulations with experiments. Results show that the simulations, which include more helium related reaction channels, could faithfully reproduce the measured discharged temporal current quantitatively. Based on the simulated discharge properties, we have found that there is complicated mode transition of discharges from the long secondary Townsend like to the dark current like, then to short primary Townsend like and to short secondary Townsend like. Related plasma physics and chemistry are described in detail.

In the third phase, a chamber-scale gas discharge of plasma enhanced chemical vapor deposition (PECVD) with silane/hydrogen as the precursors, which was used for depositing hydrogenated amorphous silicon thin film, was simulated. A multiscale temporal marching scheme for electron, ion and neutral species is designed to reduce the computational cost. Neutral flow and thermal field obtained by a finite-volume Navier-Stokes equation solver was used as the background gas. The plasma chemistry includes 15 species and 28 reaction channels. Results show that SiH_3 is the most dominating radical species with silicon that is directly related to silicon film deposition, which agree with previous experiments and simulations. The deposition rate and uniformity evaluated from the simulation results agree with experiment data if the fraction of reaction sites is assumed to be 0.015.

Recommendations of future research are also outlined at the end of this thesis.

Keyword: plasma; fluid modeling; finite difference method; parallel; PECVD; dielectric

barrier discharge

誌　　謝

A-má, lí-ê sun ū chit-kóa-á han-bān, iû-gôan sī pit-giap theh-tioh phok-sū a. lí-teh thi$^{n̄}$-téng ē-sái hòng-sim.

感謝論文指導教授吳宗信教授這些年的指導與幫忙，除了學術研究之外，這些年生活經驗得到的啟發更甚於學業。

最辛苦的還是我的母親李瑞娟與父親洪清源，在我的求學生涯中從未間斷支持，這博士學位是父母親的成就。 感謝三舅李逢輝與三舅媽劉淑娥，二舅李逢裕，你們的支持讓一個外地遊子這些年來可以無後顧之憂，專心求學。

感謝中央大學黃楓南教授在數值方法的指導。也感謝口試委員傅武雄教授、陳慶耀教授、洪哲文教授、陳彥升博士、溫志湧教授與徐振哲助理教授提供的建議與論文的補正。

一本論文的完成並不是一個人做到的，感謝研究室的夥伴們，不管是在研究上或是生活上：邵雲龍、許國賢、曾坤樟、連又永這幾位學長，允民、孟樺、凱文、穎志、明鴻、正勤、雅茹、玟琪、必任、志良、逸民、昆模、子豪、其璋、皓遠、沅明、欣芸。 學校庶務方面也感謝王翠華女士、渝瑄與于恩兩姊妹、劉惠云小姐的幫忙與照顧。

近年生活於新竹一直受到郭惠美女士的照顧以及眾位姊妹黃雅君、黃雅弟及其夫婿，還有黃任廷幫助，讓我在這個城市有了第二個家。

寥寥數字實不足言謝! 或有遺漏，但涓滴心頭。

Âng Chiat Chhàn

2010 July 28

Table of Contents

List of Tables

List of Figures

Nomenclature

Chapter 1

Introduction

1.1 Background and Motivation

Gas discharge (or low-temperature plasma) plays an important role in modern industrial applications such as display technologies, lighting sources, materials processing, environmental protection and surface treatment, to name a few [Lieberman and Lichtenberg, 1994; Meyyappan, 1994]. Understanding of the plasma physics and chemistry employed in these applications has been generally difficult because it requires the multidisciplinary knowledge, which may include advanced mathematics, electromagnetic theory, fluid mechanics, gas kinetic theory, plasma physics and plasma chemistry, among others. Modeling of the gas discharges is generally not an easy task essentially. Due to its intrinsic complexity, most researches in non-thermal, non-equilibrium gas discharges are strongly relied on experimental observation or trial-and-error approaches, which are often very expensive and time-consuming.

Recently, simulation has become an important method in understanding the plasma physics and chemistry of gas discharges since the direct quantitative measurements inside the discharge volume are either very difficult or very costly. Not only can an efficient and accurate modeling provide detailed plasma physics and chemistry within complex gas discharges, but also may it be used as an optimization tool for designing a new plasma source.

Among these developed numerical tools for gas discharges simulation, fluid modeling is one of the fastest yet accurate methods, if the pressure is not too low (e.g., $>$50 mtorr), which can greatly help the understanding of the plasma physics and chemistry. However, to cope with practical gas discharge problems, multidimensional simulations (2 to 3 spatial dimensions) using complex plasma chemistry (large number of species and reaction channels) are often required to understand the insight of the plamas. However, it often takes up to weeks or even months to complete a meaningful fluid modeling simulation, which is of course unacceptable from the practical viewpoint of being a useful tool. In addition, developed fluid modeling codes were often lack of extensive experimental validations, which may further prevent its use in

industry from being a practical tool in helping the design of gas discharge related devices.

Fortunately, recent rapid advance in computer hardware and parallel computing (multicore CPU and GPU) over the past two decades may help to reduce the runtime of a typical plasma simulation. In addition, complex yet flexible software design has become possible by taking advantage of different programming approaches such as OpenMP and MPI through high-level computer languages like C/C++ and Fortran. Concept like object-oriented design pattern further aids in the task of designing of complex software. Excellent performance capability has been demonstrated through the development of efficient numerical schemes, such as the finite difference, finite element, and finite volume methods, and algorithms, such as Krylov subspace method for iteratively solving discretized equations. Combining progress in plasma physics, scientific computing, storage capacities and calculation speeds, could lead to the development of a simulation tool to help researchers understand the physics and chemistry of plasmas, design plasma equipment and to reduce costs associated with the current trial-and-error approach. However, very few fluid modeling tools had taken advantage of these developments to further speed up the simulation. In this thesis, as a first step, we intend to develop a parallelized fluid modeling code for general gas discharge problems to brideg this gap in the plasma research community.

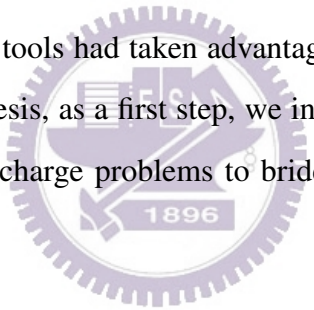

1.2 Literature Survey

Since this thesis is concerned about the development of a simulation tool for gas discharges, in the following we focus on introducing the available simulation methods in the literature and some examples of plasma applications, which is relevant to the present study.

1.2.1 Numerical Approaches for Plasma Simulation

Generally speaking, there are four different types of approaches to plasma simulation, which can be applied in different plasma conditions. They include: (1) direct Boltzmann equation solver, (2) Particle-in-Cell with Monte-Carlo collision method (PIC-MCC), (3) fluid modeling, and (4) hybrid fluid-PIC method. They are introduced in the following in turn.

1.2.1.1 Boltzmann Equation Solver

Generally the transport phenomena for all kinds of gas discharges are governed by the Bolztmann equation [Boltzmann, 1872]. If the Boltzmann equation, including the Lorentz force term, can be directly solved to obtain the velocity distribution, then all the macroscopic properties (mass, momentum and energy) related to gas discharges can be readily obtained. However, this is a integrodifferential equation which has six-dimensional phase space (3 velocity and 3 configuration spaces) plus one-dimensional time space along with a very complex collision integral which is very hard to solve. Approximations must be applied to make the equation tractable for numerical simulation The 'two-term' spherical harmonics approximation is the most popular method for reducing the problem into a four-dimensional Fokker-Planck equation [Kolobov and Arslanbekov, 2006]. The multi-term analysis also has been studied to distinguish between electrons and ions [White et al., 2003]. In brief summary, there are two major drawbacks in this approach. The first is its very high computational cost, while the second is that these approximations of the collision integral are generally not realistic for most of the cases. Thus, most researches do not adopt this approach.

1.2.1.2 Particle-in-Cell Monte Carlo Method

The Particle-in-Cell with Monte-Carlo Collision Method (PIC-MCC) is a kinetic particle-based approach which yields the distribution functions as an output of the simulation, in which each computational particle represents a large number of real particles with specific weights. The results provide the positions and velocities of a representative set of particles, from which the quantities of interest (i.e. densities, velocities, mean energy, and distribution function) can be obtained directly. Alternatively, the Monte-Carlo technique can be used to obtain the transport and rate coefficients of plasmas, which is needed in a continuum model. This method is highly suitable for discharges at very low pressure (e.g., sputtering plasma), in which the energy distribution function is far from equilibrium and cannot be modeled by continuum fluid modeling. Some well-established studies using PIC-MCC include [Birdsall and Langdon, 1991] and [Vahedi et al., 1993]. However, PIC-MCC required a sufficiently high number of particles for tracking, making it much more computationally intensive than the fluid model, which is introduced next.

1.2.1.3 Fluid Modeling

Fluid model of plasma is based on partial differential equations which describe the macroscopic quantities such as density, flux, average velocity, pressure, temperature or heat flux. The governing equations can be derived from the Boltzmann equation by taking velocity moments of the Boltzmann equation with some assumptions [Meyyappan, 1994; Gogolides and Sawin, 1992; Pitaevskii and Lifshitz, 1981] including the continuity equation, momentum equation and energy equation. The fluid descriptions break down for highly rarefied plasma, or intense non-local effect induced by strongly electric filed. Related publications of fluid modeling could be found in numerous articles, e.g. [Ventzek et al., 1993; Lymberopoulos and Economou, 1995; Bukowski et al., 1996, and references cited therein], and are not reported here.

There are generally two types of fluid modeling techniques: (1) local field approximation (LFA) and (2) local-mean-energy approximation (LMEA). The former assumes the input electric power into the plasma is fully balanced by the power dissipated by ionization, while the later solves the electron energy density equation directly. Although the transport and rate coefficients of electrons are obtained from the solution of stationary spatially homogeneous Boltzmann equation, the consequences are quite different. It has been shown that the use of LMEA is generally much better than the LFA because of the former considers non-local effect of electron energy distribution [Grubert et al., 2009].

There are two important numerical issues in plasma fluid modeling technique. First, the model equations are often solved sequentially or partly coupled based on explicit or semi-implicit scheme, which may constraint size of the time step or reduce the accuracy of the solution at each time step. This is mainly due to either the constraint of available memory or very expensive calculation of Jacobian in a fully coupled scheme, which is now either untrue or can be handled rather efficiently on modern computers. Until very recently, in computational fluid dynamics (CFD) people began to develop so-called Newton-Krylov-Schwarz type scheme for solving the inviscid compressible and viscous incompressible NS equations using the inexact Newton iterative scheme [Cai et al., 1994]. Second, almost no scalable parallelized version of plasma fluid modeling code on parallel distributed-memory machine is available for attacking more realistic problems. For realistic simulation of gas discharges fairly complex plasma chem-

istry has to be considered that is very time-consuming. This unavailability probably stems from the fact that model equations are solved sequentially as mentioned in the above which renders the performance of parallel computing unattractive. However, simulations for several practical gas discharges at atmospheric pressure require efficient parallel computing, which is otherwise impractical to do the simulations on a single computer.

1.2.1.4 Hybrid Model

Hybrid modeling techniques can take advantages of Boltzmann solver, particle method, and fluid model, which can have compromise between computational cost and accuracy. A general introduction to the hybrid model is provided by Kushner in his review paper [Kushner, 2009]. He discussed how a self-consistent modeling plasma can be decomposed into a set of sub-tasks, and introduced algorithms for carrying these tasks in Hybrid Plasma Equipment Model (HPEM), which was developed by author and his co-workers. The implementations using HPEM, such as Electron Cyclotron Resonance Source (ECR), magnetically enhanced reactive ion etching (MERIE), magnetron, Capacitively Coupled Plasma (CCP), Inductively Coupled Plasma (ICP) and so on, are also demonstrated. Another contribution by Van Dijk *et al* [van Dijk et al., 2009] described the various options for simulating plasmas on the Plasimo modeling platform, which includes electromagnetic modules, Navier-Stokes solvers using SIMPLE algorithm, transport coefficients modules and radiation trapping in an ortho-curvilinear coordinate system. Studies using Plasimo toolkits are concerned with low/high pressure plasma lighting, spectrochemistry, plasma display technology, biomedical applications and other plasma sources. The Plasimo toolkit was written in C++ and uses modern language features in object-oriented sense such as templates through a graphical user interface (GUI). VORPAL is another commercial package using a hybrid model which combines the particle-in-cell and fluid modeling [Nieter and Cary, 2004; Messmer and Bruhwiler, 2004]. It is designed in both serial and parallel code using MPI, and the large sparse system of linear equations is solved by Krylov subspace and algebraic multigrid methods. However, the fluid modeling is relatively simple with many approximations as compared to the other two codes (HPEM and Plasimo).

1.2.2 Examples of Modern Plasma Applications Using Fluid Modeling

In the following sections, we only present two typical examples of modern plasma applications which applied fluid modeling, which we are interested in the current thesis, although the fluid modeling code developed here is not only limited to deal with these problems.

1.2.2.1 Atmospheric Pressure Plasma

Recently, atmospheric-pressure plasma (APP) has attracted considerable attention, mainly because, unlike low-pressure plasmas, APP does not require the use of vacuum equipment and it is increasingly used in modern science and technology applications. Many studies have been conducted into simulations of the aerodynamic actuator using DBD to connect the flow field and plasma discharge, but very few numerical studies have been done concerning both the flow field and plasma discharge for industrial applications. Kim *et al* introduced a hybrid simulation of a spray-type DBD reactor, including a discharge module using fluid model and a flow module by solving Navier-Stokes equations [Kim et al., 2009]. In the fluid model, only charged particles were calculated by solving continuity equations with reduced fluxes without considering diffusion. An explicit upwind scheme in a structured non-uniform grid was used in the discharge with a mixture ofN_2 and additive SF_6 chemistry including 26 species and 59 reactions. However, for a thermal equilibrium discharge in a high pressure DBD, it was irrelevant to neglect diffusion effect. The flow module assumed an incompressible flow, which was questionable since the heat conduction effect was important in DBD discharge and the gas density would not be spatially constant. Using limited computing equipment (i.e. Pentium-4 2.8GHz single processor), a spray jet simulation has been reduced to a single spray hole problem with a total computation time of 10 hours for $10\mu s$ marching time in the simulation. Although the simulation is based on a realistic chamber, no experimental results were available for validation.

Rare gases like helium and argon have generally been used in RF atmospheric-pressure plasma jets, which dramatically increases operating costs [Walsh et al., 2006; Jung and Choi, 2007]. Thus, the efficient use of cheaper gases, such as nitrogen or air, has become an important issue in the development and testing of practical applications. Nitrogen DBD is much easier to sustain than those of air or oxygen since the latter is basically an electronegative discharge,

which is comparably difficult to sustain. Several numerical studies have used one-dimensional fluid modeling to simulate a nitrogen DBD, showing that mode transition from Townsend-like to glow-like could be achieved by increasing the gap distance [Choi et al., 2006]. However, the simulations were not validated by measurements, leading to questions as to whether their descriptions are physically realistic. Of course, there exist tons of related studies in the literature using fluid modeling technique, which we do not repeat here for brevity.

1.2.2.2 Silane Plasma Enhanced Chemical Vapor Deposition

Hydrogenated amorphous silicon (a-Si:H) thin films are commonly produced by plasma enhanced chemical vapor deposition (PECVD) and have been the subject of considerable research over the last decade. Aside from its uses in the fabrication of thin film solar cells, a-Si:H has is also extensively used in a broad in other devices, such as thin film transistors, liquid crystal displays, light emitting diodes, etc. In the recent decade, numerical studies on silane plasma usually focused on the details of the chemistry occurring during deposition and especially on the formation of nano-particles. Gallagher [Gallagher, 2000] presented a simple homogeneous plasma-chemistry model where particles primarily grow from SiH_3^- anions and SiH_m radicals, which play important roles in growth. Bhandarkar et al. [Bhandarkar et al., 2000] developed a zero-dimensional chemical kinetic nucleation model in which linear and cyclic silicon hydride species containing up to ten silicon atoms were considered with the assumption of a constant positive ion density proportional to the rf power. An 1D fluid model for describing a silane/hydrogen discharge was developed by Nienhuis et al [Nienhuis et al., 1997; Nienhuis, 1998], in which a one-dimensional fluid model is used incorporating silicon hydrides Si_nH_m containing up to 12 silicon atoms. A set of 68 species, including neutrals, radicals, ions, and electrons, was taken into account. Similar studies using the 1D fluid model include [Bleecker et al., 2004a,b]. There are relatively few studies focusing on 2D fluid modeling of the silane discharge [Salabas et al., 2002]. It is thus one of the objectives to present the simulation using the developed parallelized fluid modeling code in this thesis.

1.2.2.3 Summary

By directly solving the Boltzmann equation we calculate the distribution function $f(\mathbf{r}, \mathbf{c}, t)$ and hence obtain quantities of physical interest. Even if theoretical assumptions can reduce the number of dimensions, a huge effort is still required to deal with the collision integral, thus rendering it impractical. PIC-MCC can evaluate $f(\mathbf{r}, \mathbf{c}, t)$ through tracking super particles. However, a recognized disadvantage of the PIC-MCC method is its long calculation time, especially where statistical noise needs to be minimized and a high spatial resolution is required, which is nearly impossible to implement for atmospheric pressure problems if the physical size is not small. In addition the PIC-MCC method is very difficult to deal with problems with very complex plasma chemistry because of very high computational cost.

In the fluid equation approach, we can obtain these moments without knowing the $f(\mathbf{r}, \mathbf{c}, t)$. The high order moment truncation is assumed either to vanish or to be expressible in terms of lower-order moments, and the collisions are obtained by a specific $f(\mathbf{r}, \mathbf{c}, t)$ or by swarm data from experiments. The fluid modeling fails when the system cannot reach an equilibrium state, usually in low pressure. The hybrid model can take advantages of all the models above to deal with different problems.

It is clear that atmospheric pressure discharges incur lower costs and can be used in a broader range of applications than traditional low-pressure plasma using nitrogen or air as an inlet gas, also larger scale chamber such as PECVD with good uniformity is needed. Most numerical research still uses zero or 1-dimensional simulations to compromise for the large number of species and the complex chemistry reaction channels. These issues can be resolved through the use of modern computational techniques and advanced numerical schemes, but there are still few parallel implementations for realistic physical problems available in the community.

1.3 Specific Objectives

Fluid modeling, which describes discharges based on number density, mean velocity and mean energy of the charged and neutral species, is often used to model low-temperature plasmas by self-consistently coupling with Maxwell equations. Compared with the computationally-

demanding particle-in-cell method, the fluid modeling approach allows the consideration of more complex and realistic plasma chemistry, which is important in practical applications. However, numerical simulation based on fluid modeling is still very time-consuming, especially for large-scale 2D or 3D computation involving more chemical reactions. Resolving these problems with a reasonable runtime, while maintaining acceptable accuracy, requires parallelization of the fluid modeling code. Based on these, the specific objectives of this thesis can be summarized as follows:

1. To develop a parallelized fluid modeling code using LMEA approximation;
2. To validate the developed fluid modeling code under low- and atmospheric-pressure gas discharges by comparing with experiments and previous simulations wherever possible;
3. To study the details of plasma physics and chemistry of a helium dielectric barrier discharge driven by distorted sinusoidal voltages and compare with available experimental data;
4. To simulate the silane/hydrogen discharge inside a typical PECVD chamber and compare with available experimental data.

1.4 Organization of the Thesis

The chapters of this thesis are organized as follows:

Chapter 2 will start with the Boltzmann equation and derive the moment equations including the continuity equation, the momentum equation and the energy balance equation of charged particles. Then, fluid modeling equation with approximations are derived and related transport coefficients and rate constants are discussed. Practical implementation of numerical schemes, methods or toolkits are introduced.

Chapter 3 details series cases including 1-D Helium RF discharge, 1-D Helium DBD discharge, 1-D Nitrogen DBD discharge, 2-D Helium GEC discharge and validate by experimental results.

Chapter 4 discusses the effects of selecting plasma chemistry in simulations of helium DBD by comparing simulations with experimental results.

Chapter 5 demonstrates a large-scale realistic PECVD using the mixture Silane/Hydrogen gas and validates the deposition rate by experimental results.

Chapter 6 is the conclusions of this work and some possible directions for the future research work are presented.

Chapter 2

The Plasma Fluid Modeling

This chapter will start with the Boltzmann equation and derive the moment equations including the continuity equation, the momentum equation and the energy balance equation of charged particles. After the theoretical derivation, drift-diffusion approximation is introduced. The empirical assumptions for collision terms in moment equations and the heat flux of energy equation for truncation are employed. All the electron rate constants and transport coefficients can be obtained from the Boltzmann equation solver BOLSIG+ [Hagelaar, 2009], integrated by cross-section from experiments or swarm data. The transport coefficient of neutral will also be introduced. Numerical methods will introduce the Sharfetter-Gummel scheme, nondimensional coefficients, the discretization of fluid equations and boundary conditions. This chapter will also introduce the Newton-Krylov-Schwarz method, pre-conditioners, linear equation solvers, and domain decomposition algorithm which is implemented by means of PETSc toolkit [Balay et al., 2001].

2.1 Boltzmann Equation and Fluid approximation

The Boltzmann kinetic equation for each charged component α of weakly ionized gas under the influence of electromagnetic field can be written as [Pitaevskii and Lifshitz, 1981]

$$\left(\frac{\partial}{\partial t}+\mathbf{c}\cdot\frac{\partial}{\partial \mathbf{r}}+\frac{q_\alpha}{m_\alpha}\left(\mathbf{E}+\mathbf{c}\times\mathbf{B}\right)\cdot\frac{\partial}{\partial c}\right)f_\alpha=-J(f_\alpha,F_0)-\sum_{\alpha'}J(f_\alpha,f_{\alpha'}) \tag{2.1}$$

, where q_α and m_α are charge and mass of species α, and $f_\alpha(\mathbf{r},\mathbf{c},t)$ is the phase distribution function at the position $\mathbf{r}$ and velocity $\mathbf{c}$. $\mathbf{E}$ and $\mathbf{B}$ are electric field and magnetic field respectively. $J(f_\alpha,F_0)$ and $J(f_\alpha,f_{\alpha'})$ denote to the collision terms for charged-neutral species collision and charged-charged species interactions, respectively. F_0 is the velocity distribution of neutral gas. The charged-neutral species collision term may include elastic collisions and important conservative inelastic collision, for example, the excitation or dissociation process of the electrons in collisions with the ground state atoms or molecules of the gas. The term $J(f_\alpha,f_{\alpha'})$ describes the interaction between charged-particles via Coulomb force, which can be ignored in the current thesis since we only deal with the problems of weakly ionizaed plasma.

The macroscopic property can be obtained as the velocity moments of the distribution function as

$$< \varphi(\mathbf{c}) >_{\alpha} = \frac{\int d\mathbf{c}\, \varphi(\mathbf{c}) f_{\alpha}(\mathbf{r}, \mathbf{c}, t)}{\int d\mathbf{c} f_{\alpha}(\mathbf{r}, \mathbf{c}, t)} \tag{2.2}$$

, where $\varphi(\mathbf{c}) = 1, m\mathbf{c}, \frac{1}{2}m\mathbf{c}^2$ leads to number density n_{alpha}, average velocity $\mathbf{v}_{\alpha}$ and average energy ϵ_{α}. Starting with the number density,

$$n_{\alpha}(\mathbf{r}, t) = \int d\mathbf{c}\ f_{\alpha}(\mathbf{r}, \mathbf{c}, t). \tag{2.3}$$

The average velocity can be written as

$$\mathbf{v}(\mathbf{r}, t) = \frac{\int d\mathbf{c}\ \mathbf{c} f(\mathbf{r}, \mathbf{c}, t)}{\int d\mathbf{c}\ f_{\alpha}(\mathbf{r}, \mathbf{c}, t)}. \tag{2.4}$$

Finally, the average energy can be written as

$$\varepsilon_{\alpha}(\mathbf{r}, t) = \frac{m}{2} \frac{\int d\mathbf{c} c^2 f(\mathbf{r}, \mathbf{c}, t)}{\int d\mathbf{c} f(\mathbf{r}, \mathbf{c}, t)}.. \tag{2.5}$$

A set of moment equations can be readily obtained by multiplying (2.1) by $\varphi(\mathbf{c})$ and integrating over all velocity space. In other words, the continuity, the momentum and energy density equations of the plasma fluid modeling equations can be obtained by set $\varphi(\mathbf{c}) = 1$, $m\mathbf{c}$, and $\frac{1}{2}mc^2$, respectively. Now, for later convenience we define $C_{\varphi(\mathbf{c})}$, the integral related to general collision term as

$$C_{\varphi(\mathbf{c})} = -\int d\mathbf{c}\ \varphi(\mathbf{c}) J(f_{\alpha}, F_0). \tag{2.6}$$

For $\varphi(\mathbf{c}) = 1$, the first term of Boltzmann equation yields

$$\int d\mathbf{c}\ \frac{\partial}{\partial t} f_{\alpha}(\mathbf{r}, \mathbf{c}, t) = \frac{\partial}{\partial t} \int d\mathbf{c}\ f_{\alpha}(\mathbf{r}, \mathbf{c}, t) = \frac{\partial}{\partial t} n(\mathbf{r}, t). \tag{2.7}$$

The second term is then written as

$$\int d\mathbf{c}\ \mathbf{c} \cdot \nabla_r f_{\alpha}(\mathbf{r}, \mathbf{c}, t) = \nabla_r \int d\mathbf{c}\ \mathbf{c} f_{\alpha}(\mathbf{r}, \mathbf{c}, t) = \nabla_r (n_{\alpha}(\mathbf{r}, t) \mathbf{v}(\mathbf{r}, t)). \tag{2.8}$$

The rest terms on the left hand side vanish upon performing the integration over velocity space and the result is the exact species continuity equation that is written as

$$\frac{\partial}{\partial t} n_{\alpha}(\mathbf{r}, t) + \nabla_r \cdot (n_{\alpha}(\mathbf{r}, t) \mathbf{v}(\mathbf{r}, t)) = C_1. \tag{2.9}$$

where

$$C_1 = -\int d\mathbf{c} J(f_{\alpha}, F_0). \tag{2.10}$$

For $\varphi(\mathbf{c}) = m\mathbf{c}$, the momentum equation is obtained by $m\mathbf{c}$ and integrating over the velocity space. Here I keep the particle mass m_α in the denominator for derivation convenience and yield

$$\frac{\partial}{\partial t}\int d\mathbf{c}\ \mathbf{c} f_\alpha + \frac{\partial}{\partial t}\int d\mathbf{c}\ \mathbf{cc}\cdot\nabla_r f_\alpha + \frac{q_\alpha}{m_\alpha}\int d\mathbf{c}\ \mathbf{c}\,(\mathbf{E}+\mathbf{c}\times\mathbf{B})\cdot\nabla_c f_\alpha = C_{m\mathbf{c}} \tag{2.11}$$

The first term in the left hand side is

$$\frac{\partial}{\partial t}\int d\mathbf{c}\ \mathbf{c} f_\alpha = \frac{\partial}{\partial t} n_\alpha \mathbf{v}. \tag{2.12}$$

The integrand of the second term is rearranged as $\mathbf{c}\ \mathbf{c}\cdot\nabla_\mathbf{r} f_\alpha = \nabla_\mathbf{r}\cdot(\mathbf{cc} f_\alpha)$ and thus the second term becomes

$$\frac{\partial}{\partial t}\nabla_r \int d\mathbf{c}\ \mathbf{cc}\cdot f_\alpha = \frac{\partial}{\partial t}\nabla_r\cdot(n_\alpha < \mathbf{cc} >) \tag{2.13}$$

where

$$< \mathbf{cc} >= \frac{\int d\mathbf{c}\ \mathbf{cc} f_\alpha}{n_\alpha}. \tag{2.14}$$

The third term is

$$\begin{aligned}\int d\mathbf{c}\ \mathbf{c}(\mathbf{E}+\mathbf{c}\times\mathbf{B}) f_\alpha = &\int d\mathbf{c}\ \nabla_\mathbf{c}\cdot(f\ \mathbf{c}(\mathbf{E}+\mathbf{c}\times\mathbf{B})) \\ &- \int d\mathbf{c}\ f_\alpha \mathbf{c}\nabla_\mathbf{c}\cdot(\mathbf{E}+\mathbf{c}\times\mathbf{B}) - \int d\mathbf{c}\ f_\alpha(\mathbf{E}+\mathbf{c}\times\mathbf{B})\cdot\nabla_\mathbf{c}\mathbf{c}.\end{aligned} \tag{2.15}$$

The first integral in the right had side of eq. (2.15) can be further converted into a surface integral using divergence theorem. Here we would like to remind that the developed moments are multiplied by the powers of the velocity vector and integrating over whole velocity space. To complete the integrations we need to know the behavior of the distribution function at large $\mathbf{c}$ value. From physical viewpoint, no particle can have infinite velocity and it's reasonable to assume the surface integral will be vanished while the distribution function $f_\alpha(\mathbf{r}, \mathbf{c}, t)$ falls off faster then the integrand in the velocity space as $\mathbf{c} \to \infty$. The second term in the right hand side would also vanish because the electric field is not a function of velocity $\mathbf{c}$ and $\mathbf{c}\times\mathbf{B}$ is always perpendicular to $\nabla_\mathbf{c}$. The $\nabla_\mathbf{c}\mathbf{c}$ in the third term in the right hand side is obviously a unit tensor. Thus, eq. (2.15) can be rewritten as

$$\frac{q_\alpha}{m_\alpha}\int d\mathbf{c}(\mathbf{E}+\mathbf{c}\times\mathbf{B}) f_\alpha = -\frac{q_\alpha}{m_\alpha}\int d\mathbf{c}\ f_\alpha(\mathbf{E}+\mathbf{c}\times\mathbf{B})\cdot\nabla_\mathbf{c}\mathbf{c} = -\frac{q_\alpha}{m_\alpha} n_\alpha(\mathbf{E}+\mathbf{v}\times\mathbf{B}). \tag{2.16}$$

By substituting eqs. (2.12-2.15) into eq. (2.11), then we can have the momentum equation as

$$\frac{\partial}{\partial t} n_\alpha \mathbf{v} + \nabla_r\cdot(n_\alpha < \mathbf{cc} >) - \frac{q_\alpha}{m_\alpha} n_\alpha(\mathbf{E}+\mathbf{v}\times\mathbf{B}) = \frac{C_{m\mathbf{c}}}{m_\alpha}. \tag{2.17}$$

Multipling m_α, the mometum equation can be obtained as

$$\frac{\partial}{\partial t} m_\alpha n_\alpha \mathbf{v} + \nabla_r \cdot (m_\alpha n_\alpha < \mathbf{cc} >) + q_\alpha n_\alpha (\mathbf{E} + \mathbf{v} \times \mathbf{B}) = C_{m\mathbf{c}}. \tag{2.18}$$

Next we define $\mathbf{c} = \mathbf{v} + \mathbf{w}$, where $\mathbf{v}$ is the mean velocity and $\mathbf{w}$ is the random thermal velocity on the top of the mean velocity. Thus, the second term in the left hand side of eq. (2.18) can be rewritten as

$$\nabla_r \cdot (n_\alpha < \mathbf{cc} >) = \nabla_r \cdot (n_\alpha \mathbf{vv}) + \nabla_r \cdot (n_\alpha < \mathbf{ww} >) + 2\nabla_r \cdot (n_\alpha \mathbf{u} < \mathbf{w} >). \tag{2.19}$$

, where the last term vanishes because $< \mathbf{w} >$ is obviously zero. The quantity $m_\alpha n_\alpha < \mathbf{ww} >$ is denoted by a stress tensor $\overleftrightarrow{P}$, which leads to

$$\begin{aligned} \nabla_r \cdot (n_\alpha < \mathbf{cc} >) &= \nabla_r \cdot (n_\alpha \mathbf{vv}) + \frac{1}{m_\alpha} \nabla \cdot \overleftrightarrow{P}_\alpha & (2.20) \\ &= \mathbf{v}_\alpha \nabla_r \cdot (n_\alpha \mathbf{v}) + n_\alpha (\mathbf{v}_\alpha \cdot \nabla_r)\mathbf{v} + \frac{1}{m_\alpha} \nabla_r \cdot \overleftrightarrow{P} & (2.21) \end{aligned}$$

Thus, the eq. (2.18) can be represented as

$$\frac{\partial}{\partial t} m_\alpha n_\alpha \mathbf{v}_\alpha + m_\alpha \mathbf{u} \nabla_r \cdot (n_\alpha v_\alpha) + m_\alpha n_\alpha (\mathbf{v}_\alpha \cdot \nabla_r)\mathbf{v}_\alpha + \nabla_r \cdot \overleftrightarrow{P}_\alpha - q_\alpha n_\alpha (\mathbf{E} + \mathbf{v}_\alpha \times \mathbf{B}) = C_{m\mathbf{c}}. \tag{2.22}$$

If we substitute the continuity eq. (2.9) into eq. (2.22), we can have the momentum equation as

$$m_\alpha n_\alpha \frac{\partial}{\partial t} \mathbf{v}_\alpha + m_\alpha n_\alpha (\mathbf{v}_\alpha \cdot \nabla_r)\mathbf{v}_\alpha + \nabla_r \cdot \overleftrightarrow{P}_\alpha - q_\alpha n_\alpha (\mathbf{E} + \mathbf{v}_\alpha \times \mathbf{B}) = C'_{m\mathbf{c}}. \tag{2.23}$$

, where $C'_{m\mathbf{c}} = C_{m\mathbf{c}} - m_\alpha C_1$.

For $\varphi(\mathbf{c}) = \frac{1}{2} m c^2$, the conservation of energy can be obtained similarly after tedious algebraic arrangement as

$$\frac{\partial}{\partial t} n_\alpha < \frac{1}{2} m_\alpha c^2 > + \nabla_r \cdot (n_\alpha < \frac{1}{2} m_\alpha c^2 \mathbf{c} >) - q_\alpha n_\alpha \mathbf{E} \cdot \mathbf{v} = C_{\frac{1}{2}mc^2} \tag{2.24}$$

where the third term can be derived through the following steps,

$$\begin{aligned} q_\alpha \int d\mathbf{c}\, \frac{1}{2} c^2 (\mathbf{E} + \mathbf{c} \times \mathbf{B}) \nabla_{\mathbf{c}} f_\alpha &= -q_\alpha \int d\mathbf{c}\, \frac{1}{2} (\mathbf{E} + \mathbf{c} \times \mathbf{B}) f_\alpha \nabla_{\mathbf{c}} c^2 & (2.25) \\ &= -q_\alpha \int d\mathbf{c}\, (\mathbf{E} + \mathbf{c} \times \mathbf{B}) f_\alpha \cdot \mathbf{c} & (2.26) \\ &= -q_\alpha n_\alpha \mathbf{E} \cdot \mathbf{v}. & (2.27) \end{aligned}$$

The resulting energy balance equation without including kinetic energy is written as

$$\frac{3}{2}n_\alpha k_B\left(\frac{\partial T_\alpha}{\partial t}+\mathbf{v}_\alpha\cdot\nabla_r T_\alpha\right)+\nabla_r\cdot J_{q,i}+\overleftrightarrow{P}_\alpha:\nabla_r\mathbf{v}-q_\alpha n_\alpha\mathbf{E}\cdot\mathbf{v}=C_{\frac{1}{2}mc^2} \tag{2.28}$$

, where k_B is the Boltzmann constant, and the heat flux and pressure tensor are, respectively, expressed as

$$J_{q,i}=\frac{1}{2}n_\alpha m_\alpha<w^2\mathbf{w}> \tag{2.29}$$

and, as mentioned before, the pressure tensor

$$\overleftrightarrow{P}=n_\alpha m_\alpha<\mathbf{ww}>. \tag{2.30}$$

Note that all the n^{th} order velocity moments of the Boltzmann equations of $\mathbf{c}$ will lead to $n+1$ order of $\mathbf{c}$ in the moment equations. Thus, to obtain a complete description of gas discharges, we need an infinite number of moment equations derived from the Boltzmann equation. Of course we can move on to derive the higher moment equations; however, in practice, the moment equations must be "closed" with some approximation based on physical argument. In many practical problems this is made in the first order by substituting the energy equation by an equation of the state, and in the second order by using algebraic expression for the heat flux as closure approximation. Similarly, the evaluation of the respective collision term in practical way usually needs cross section from experiments or *ab initio* calculations. Moreover, to complete the derivation of the system of governing equations and to obtain a self-consistent descriptions of gas discharges, we need to include the Maxwell equations describing the electromagnetic behavior of charged particles. The derivation of fluid modeling employed in this study will be discussed next.

2.2 Plasma Fluid Modeling Equations

Recalling the fluid modeling equations for a charged species α derived from the Boltzmann equations, they include: Continuity equation as

$$\frac{\partial}{\partial t}n_\alpha(\mathbf{r},t)+\nabla_r\cdot(n_\alpha(\mathbf{r},t)\mathbf{v}(\mathbf{r},t))=C_1.$$

momentum equation as

$$m_\alpha n_\alpha\frac{\partial}{\partial t}\mathbf{v}_\alpha+m_\alpha n_\alpha(\mathbf{v}_\alpha\cdot\nabla_r)\mathbf{v}_\alpha+\nabla_r\cdot\overleftrightarrow{P}_\alpha-q_\alpha n_\alpha(\mathbf{E}+\mathbf{v}_\alpha\times\mathbf{B})=C'_{m\mathbf{c}}.$$

and energy equation as

$$\frac{3}{2}n_\alpha k_B\left(\frac{\partial T_\alpha}{\partial t}+\mathbf{v}_\alpha\cdot\nabla_r T_\alpha\right)+\nabla_r\cdot J_{q,i}+\overleftrightarrow{P}_\alpha:\nabla_r\mathbf{v}-q_\alpha n_\alpha\mathbf{E}\cdot\mathbf{v}=C_{\frac{1}{2}mc^2}.$$

However, the above fluid modeling equations are not used in practice and required some approximations which are shown next.

2.2.1 Drift-Diffusion Approximation

Start from the momentum equation, the divergence of pressure tensor $\overleftrightarrow{P}$ contains information of inhomogeneity and viscosity of the gas discharges. Considering sufficient collisions among particles, they will reach equilibrium with a velocity distribution close to Maxwellian and the pressure tensor becomes a diagonal one, or even isotropic as

$$\nabla\cdot\overleftrightarrow{P}\rightarrow\nabla P. \tag{2.31}$$

To form a closed set of moment equations, we use a thermodynamic equation of state to relate P and n_α as

$$P=n_\alpha k_B T_\alpha \tag{2.32}$$

In addition, assume temperature equilibrates in slow time variation, which leads to the following form

$$\nabla P=k_B T_\alpha\nabla n_\alpha. \tag{2.33}$$

The collision term in momentum equation mainly includes momentum transfer collision and inelastic collisions and is expressed as follows

$$C'_{m\mathbf{c}} = C_{m\mathbf{c}}-mC_1 \tag{2.34}$$

$$= -\sum m_\alpha n_\alpha\nu_{\alpha\beta}(\mathbf{u}-\mathbf{u}_\beta)-m\mathbf{u}(G-L) \tag{2.35}$$

, where G and L are rates of generation and destruction of species α, respectively. $\nu_{\alpha\beta}$ is momentum transfer frequency for α particles collisions with β particles and $\mathbf{u}_\beta$ is the mean velocity of species β. The contribution of the inelastic collision to the collision term, as compare to that of momentum transfer collision, is small and can be ignored for most of the cases. Thus, for slow time variation $\mathbf{u}_\beta\rightarrow 0$, the collision term can be rewritten as

$$C'_{m\mathbf{c}}=-m_\alpha n_\alpha\nu_m\mathbf{u} \tag{2.36}$$

where ν_m is the momentum transfer collision frequency.

If we neglect the unsteady term and inertial term and consider the gas discharges only influenced by electric field, then the momentum equation can be further reduced to

$$0 = q_\alpha n_\alpha \mathbf{E} - \nabla P - m_\alpha n_\alpha \nu_m \mathbf{u}. \tag{2.37}$$

By solving for $\mathbf{u}$, we can obtain

$$\mathbf{u} = \frac{q_\alpha \mathbf{E}}{m_\alpha \nu_m} - \frac{k_B T_\alpha}{m_\alpha \nu_m} \frac{\nabla n_\alpha}{n_\alpha}. \tag{2.38}$$

Farther, we can obtain the particle flux Γ as

$$n_\alpha \mathbf{u}_\alpha = \Gamma_\alpha = \pm \mu_\alpha n_\alpha \mathbf{E} - D_\alpha \nabla n_\alpha \tag{2.39}$$

where the direction of drift is decide by the particles' charge, and the macroscopic mobility and diffusion coefficients are, respectively, expressed as

$$\mu_\alpha = \frac{|q_\alpha|}{m_\alpha \nu_m} \tag{2.40}$$

and

$$D_\alpha = \frac{k_B T_\alpha}{m_\alpha \nu_m}. \tag{2.41}$$

Note eq. (2.39) is the so-called drift-diffusion approximation for the momentum equation, and the coefficients of mobility μ and diffusion D are input parameters required in a typical plasma simulation.

2.2.2 Electron Impact Reaction Rate Coefficients and Electron Transport Coefficient

Electrons always play a key role in gas discharges with much higher energy than other heavy species in the non-thermal (non-equilibrium) plasma. Accordingly, electron impact reactions are always the key issues in understanding the discharge behavior using analytical or numerical approaches. Assuming an electron colliding with neural species, the source term for generation or loss in the electron continuity equation can be evaluated as

$$C_1 = \sum_r k_r(T_e) n_e n_g \tag{2.42}$$

where T_e is the electron temperature, and k_r is the reaction rate constant of collision type r. The approximation of the collision term in the momentum transport equation leads to the resulting

transport coefficient by a momentum collision frequency ν_m The related electron energy lost because of momentum transfer to neutral species can then be derived as

$$C_{mc^2,\text{momentum transfer}} = 3\frac{m_e}{M} n_e k_B \nu_m (T_e - T_g) \tag{2.43}$$

where ν_m is written as

$$\nu_m = k_m(T_e) n_g \tag{2.44}$$

where k_m is the momentum transfer reaction rate constant. As compare to the momentum transfer, the inelastic collision is generally negligible in the momentum equation. However, the electron energy consumption by electron impact inelastic collision is too significant to be ignored and the corresponding energy lost can be written as

$$C_{mc^2,\text{in}} = \sum_{r=\text{in}} \epsilon_{\text{in}} k_r(T_e) n_e n_g \tag{2.45}$$

where the subscript "in" denotes to the inelastic reaction and ϵ_{in} is the threshold energy which is the energy barrier required for the electrons to overcome in the inelastic reaction process.

2.2.2.1 Calculation of Rate and Transport Coefficients

The rate coefficient, i.e. k_r and k_m discussed in Section 2.2.2, can be obtained by experimental measurement or theoretical calculation through swarm data or experimental or numerical cross section. Swarm data usually provide the relation to connect transport coefficient and rate constant with a reduced electric field($\mathbf{E}/p$). The velocity distribution is usually assumed to be equal to that of a particle swarm in a spatially uniform effective electric field that gives the same mean energy as determined by the energy balance equation. This means we do not have to solve the energy balance equation directly, which is often not a trivial task. On the other hand, to find the rate constant through cross section data, we can calculate rate coefficient by integrating over the electron energy ε

$$k_\lambda = \int \left(\frac{2\varepsilon}{m_e}\right)^{\frac{1}{2}} f(\varepsilon)\sigma_\lambda(\varepsilon) d\varepsilon \tag{2.46}$$

where $\sigma_\lambda(\varepsilon)$ is the cross section of reaction λ, which can be either momentum transfer reaction or inelastic reactions such as ionization and excitation, to name a few. $f(\varepsilon)$ is the electron energy distribution function (EEDF) which we will discuss in detail next.

2.2.2.2 Electron Energy Distribution

The electron energy distribution function (EEDF) $f(\varepsilon)$ (or $f(\mathbf{c})$) is generally unknown when we derived the moments of the Boltzmann equation. In order to calculate the transport and reaction parameters, the EEDF must be known. In thermal equilibrium, most common approach is to assume Maxwellian energy distribution for the electrons. But in low-pressure plasmas, the EEDF has been confirmed it is not a Maxwellian through several experiments and numerical simulations (Particle-in-Cell) [Vahedi et al., 1993]. However, it could be approximated by some special form such as the Druyvesteyn distribution function [Lieberman and Lichtenberg, 1994]. No matter what form of electron energy distribution function we adopt, we can readily calculate the reaction rates and the transport coefficients through eq. (2.46).

One of the most well-known approach in the fluid modeling community is the so-called local field approximation (LFA) The implicit assumption in this approach is that the energy gained by charged particles from the electric field is locally balanced by the loss in various collisional processes. Further, the energy distribution function in time and space is assumed to be the equilibrium velocity distribution of the particles in a uniform dc electric field and the value of electric field equal to that at their location and time in the discharge. Therefore, the energy balance equation does not need to be explicitly solved when local field approximation is enforced. This leads to that the rate constants determining the species generation, loss, and transport can be expressed as a local function of the reduced electric field $\frac{\mathbf{E}(\mathbf{r})}{n(\mathbf{r})}$. However, the local field approximation fails in regions of strong electric field gradient when non-local charged particle flux is important in determining the discharge properties. In practice, at least the electron energy equation has to be considered since the electrons are the most important charged species in sustaining a plasma.

The electron transport coefficients and electron impact reaction rate constants are calculated through a Boltzmann equation solver BOLSIG+ [Hagelaar, 2009] Prior to the fluid modeling, all the necessary transport and rate constants are organized as function of electron temperature in a lookup table.

2.2.3 Neutral Species Transport Coefficient

The diffusion coefficient D of neutral species, which is a function of both temperature and pressure, can be calculated between any two components (binary pair) of a mixture as

$$D_{\eta,\xi} = \frac{3k_B T_{gas}\sqrt{\frac{2\pi T_{gas}}{\tau_{\eta,\xi}}}}{16 P_{total}\pi\sigma_{\eta\xi}^2\Omega_D(\psi)} \tag{2.47}$$

where T_{gas} is the gas temperature, P_{total} is the total pressure, $\tau_{\eta,\xi}$ is the reduced mass as

$$\tau_{\eta,\xi} = \frac{m_\eta m_\xi}{m_\eta + m_\xi} \tag{2.48}$$

and $\sigma_{\eta,\xi}$ is binary "collision diameter", which is a Lennard-Jones parameter that can be expressed as

$$\sigma_{\eta,\xi} = \frac{\sigma_\eta + \sigma_\xi}{2} \tag{2.49}$$

Ω_D is collision integral in a form written as

$$\Omega_D = \frac{A}{\psi^B} + \frac{C}{e^{D\psi}} + \frac{E}{e^{F\psi}} + \frac{G}{e^{H\psi}} \tag{2.50}$$

where ψ is

$$\psi = \frac{k_B T_{gas}}{\epsilon_{\eta,\xi}} \tag{2.51}$$

in which reduced energy $\epsilon_{\eta,\xi}$ is expressed as

$$\epsilon_{\eta,\xi} = \sqrt{\epsilon_\eta \epsilon_\xi}. \tag{2.52}$$

, and $A = 1.06036$, $B = 0.15610$, $C = 0.19300$, $D = 0.47635$, $E = 1.03587$, $F = 1.52996$, $G = 1.76474$, and $H = 3.89411$. Then, the diffusivity of a species η can be expressed as

$$D_\eta = \frac{P_{total}}{\sum_{\xi=background}\frac{P_\xi}{D_{\eta,\xi}}} \tag{2.53}$$

, where P_ξ is the partial pressure of species ξ.

2.2.4 Ion Species Transport Coefficient

Similar to neutral species, the mobility of an ion also can be applied between any two components

$$\mu_{\eta,\xi} = 0.514\frac{T_{gas}}{P_{total}\sqrt{\tau_{\eta,\xi}\alpha_\eta}} \tag{2.54}$$

where α_η is the polarizability of ion η. Thus, mobility of species η can be written as

$$\mu_\eta = \frac{P_{total}}{\sum_{\xi=background} \frac{P_\xi}{\mu_{\eta,\xi}}}. \tag{2.55}$$

The ion diffusivity coefficient can then be obtained by Einstein relation

$$D_\eta = \frac{k_B T_{ion}}{q} \mu_\eta. \tag{2.56}$$

2.2.5 Fluid Modeling Equations

Summarizing the fluid modeling equation used in this thesis as presented in the above with some approximations, we can write them in simplified forms in the followings in turn. The electron continuity equation is expressed as

$$\frac{\partial}{\partial t} n_e + \nabla \cdot \mathbf{\Gamma}_e = S_e \tag{2.57}$$

where the flux is estimated using drift-diffusion approximation as

$$\mathbf{\Gamma}_e = -D_e \nabla n_e - n_e \mu_e \mathbf{E}. \tag{2.58}$$

The ion continuity equation is expressed as

$$\frac{\partial}{\partial t} n_i + \nabla \cdot \mathbf{\Gamma}_i = S_i \tag{2.59}$$

where the flux is estimated using drift diffusion approximation as

$$\mathbf{\Gamma}_i = -D_i \nabla n_i + sign(q_i) Z n_i \mu_i \mathbf{E}. \tag{2.60}$$

where Z the number of charges carried by ion. The neutral species continuity equation is expressed as

$$\frac{\partial}{\partial t} n_p + \nabla \cdot \mathbf{\Gamma}_p = S_p \tag{2.61}$$

where the flux is expressed as

$$\mathbf{\Gamma}_p = -D_p \nabla n_p. \tag{2.62}$$

Finally, the electron energy density equation is expressed as

$$\frac{\partial}{\partial t} n_\epsilon + \nabla \cdot \mathbf{\Gamma}_\epsilon = -e\Gamma_e \cdot \mathbf{E} - S_\epsilon \tag{2.63}$$

where $n_\epsilon = \frac{3}{2} n_e k_B T_e$ and the energy flux is written as

$$\mathbf{\Gamma}_\epsilon = \frac{5}{2} T_e \Gamma_e - \frac{5}{2} n_e D_e \nabla T_e. \tag{2.64}$$

Note that in the current thesis we do not consider the ion energy density equation like others in the fluid modeling community since it is comparatively unimportant as compared to the electron energy density in most gas discharges.

2.3 Numerical Methods and Algorithms

2.3.1 Sharfetter-Gummel Scheme for Mass Flux

It is well-known that it required very fine grid sizes for the convection-diffusion type PDE to be numerically stable if standard finite-difference method is employed. The Scharfetter-Gummel (SG) scheme, which originally had been developed for semiconductor device simulations, provides an optimum way to discretize the drift-diffusion equation for particle transport [Scharfetter and Gummel, 1969]. The idea of SG scheme is to approximate the flux by a boundary value problem along each edge in a given grid, which yields an exponential approximation to the potential distribution. Therefore, it's also called an exponentially fitted method.

To demonstrate how the SG scheme works, we derive the corresponding formulation using a one-dimensional example. Assume there are two grid points i and $i+1$, and the flux between the grids is $\Gamma_{i+\frac{1}{2}}$. The drift-diffusion equation of positive charged particle can be written as

$$\Gamma_{p,i+\frac{1}{2}} = -D_{p,i+\frac{1}{2}} \frac{\partial n_p}{\partial x} - \mu_{p,i+\frac{1}{2}} \frac{\partial \phi}{\partial x} n_p. \tag{2.65}$$

where the first and second terms in the RHS represent the diffusion and drift fluxes, respectively. By the change of variables from position to potential through chain rule, we can obtain

$$\frac{\partial \phi}{\partial x} \frac{\partial}{\partial \phi} n_p + \frac{\mu_{p,i+\frac{1}{2}}}{D_{p,i+\frac{1}{2}}} \frac{\partial \phi}{\partial x} n_p = -\frac{\Gamma_{p,i+\frac{1}{2}}}{D_{p,i+\frac{1}{2}}} \tag{2.66}$$

in which assume that $\frac{\partial \phi}{\partial x}$ is independent of potential. After rearrangement, we can have the first order ordinary differential equation as follows:

$$\frac{\partial}{\partial \phi} n_p + \frac{\mu_{p,i+\frac{1}{2}}}{D_{p,i+\frac{1}{2}}} n_p = -\frac{\Gamma_{p,i+\frac{1}{2}}}{D_{p,i+\frac{1}{2}} \frac{\partial \phi}{\partial x}}. \tag{2.67}$$

The solution of above ODE is readily obtained as

$$n_p(\phi) = Ce^{-\frac{\mu_{p,i+\frac{1}{2}}}{D_{p,i+\frac{1}{2}}}\phi} - \frac{\Gamma_{p,i+\frac{1}{2}}}{\mu_{p,i+\frac{1}{2}}\frac{\partial\phi}{\partial x}} \tag{2.68}$$

By applying the boundary condition $n_i = n_i(\phi_i)$ and $n_{i+1} = n_{i+1}(\phi_{i+1})$, the constant C and flux $\Gamma_{p,i+\frac{1}{2}}$ can be found easily as,

$$C = \frac{n_i - n_{i+1}}{e^{-\frac{\mu_{p,i+\frac{1}{2}}}{D_{p,i+\frac{1}{2}}}\phi_i} - e^{-\frac{\mu_{p,i+\frac{1}{2}}}{D_{p,i+\frac{1}{2}}}\phi_{i+1}}} \tag{2.69}$$

and

$$\Gamma_{p,i+\frac{1}{2}} = -\frac{D_{p,i+\frac{1}{2}}}{\Delta x}\left[\frac{-\frac{\mu_{p,i+\frac{1}{2}}}{D_{p,i+\frac{1}{2}}}(\phi_{i+1}-\phi_i)}{e^{-\frac{\mu_{p,i+\frac{1}{2}}}{D_{p,i+\frac{1}{2}}}(\phi_{i+1}-\phi_i)}-1}n_{i+1} - \frac{\frac{\mu_{p,i+\frac{1}{2}}}{D_{p,i+\frac{1}{2}}}(\phi_{i+1}-\phi_i)}{e^{\frac{\mu_{p,i+\frac{1}{2}}}{D_{p,i+\frac{1}{2}}}(\phi_{i+1}-\phi_i)}-1}n_i\right] \tag{2.70}$$

or

$$\Gamma_{p,i+\frac{1}{2}} = -\frac{D_{p,i+\frac{1}{2}}}{\Delta x}\left[n_{i+1}B(-X) - n_iB(X)\right] \tag{2.71}$$

, where $X = \frac{\mu_{p,i+\frac{1}{2}}}{D_{p,i+\frac{1}{2}}}(\phi_{i+1} - \phi_i)$, and B is Bernouli function expressed as

$$B(x) = \frac{X}{e^X - 1}. \tag{2.72}$$

Similarly we can write the electron flux equation as

$$\Gamma_e = -\frac{1}{m_e\nu}\nabla(n_ek_BT_e) - \frac{qn_e}{m_e\nu}\vec{E} \tag{2.73}$$

$$= -\frac{n_e}{m_e\nu}\nabla(k_BT_e) - \frac{k_BT_e}{m_e\nu}\nabla n_e - \frac{qn_e}{m_e\nu}\vec{E} \tag{2.74}$$

The corresponding ODE for electrons can be written as

$$\frac{k_BT_e}{m_e\nu}\nabla n_e + \left(\frac{\nabla(k_BT_e)}{m_e\nu} + \frac{q}{m_e\nu}\vec{E}\right)n_e = -\Gamma_e \tag{2.75}$$

or

$$\nabla n_e + \left(\frac{\nabla(k_BT_e)}{k_BT_e} + \frac{q}{k_BT_e}\vec{E}\right)n_e = -\frac{\Gamma_e}{\frac{k_BT_e}{m_e\nu}} \tag{2.76}$$

Again, for one-dimensional case, we can obtain the solution of the above ODE for electrons as

$$n_e(\phi) = Ce^{-\frac{a}{\frac{\partial\phi}{\partial x}}\phi} + \frac{b}{a} \tag{2.77}$$

where C is a constant. a and b are defined, respectively, as

$$a = \frac{\nabla(k_BT_e)}{k_BT_e} + \frac{q}{k_BT_e}\vec{E}, \tag{2.78}$$

$$b = -\frac{\Gamma_e}{\frac{k_B T_e}{m_e \nu}}. \tag{2.79}$$

The constant C and the flux $\mathbf{\Gamma}_e$ can be readily obtained from the boundary conditions. They are written as

$$C = \frac{n_{i+1} - n_i}{e^{-a'\phi_{i+1}} - e^{-a'\phi_i}} \tag{2.80}$$

$$\Gamma_{e,i+\frac{1}{2}} = -\frac{1}{\Delta x}\frac{k_B T_e}{m_e \nu}\left[B(-X)n_{i+1} - B(X)n_i\right] \tag{2.81}$$

where $X = a'(\phi_{i+1} - \phi_i)$ and $a' = \frac{a}{\frac{\partial \phi}{\partial x}}$. Or equivalently, the electron flux can be expressed as

$$\Gamma_{e,i+\frac{1}{2}} = -\frac{D_{e,i+\frac{1}{2}}}{\Delta x}\left[n_{i+1}B(X) - n_i B(-X)\right] \tag{2.82}$$

2.3.2 Non-dimensionalization

Let n_0 denote the background gas density. The dimensionless potential, length, time, and velocity are defined as follows:

$$\phi' = \frac{e\phi}{k_B T_0} = \frac{\phi}{\phi_0}, \tag{2.83}$$

$$u_p' = \frac{u_p}{u_0}, \tag{2.84}$$

$$u_e' = \frac{u_e}{u_0}, \tag{2.85}$$

where u_0 is defined as

$$u_0 = \left(\frac{k_B T_0}{m_p}\right)^{\frac{1}{2}}. \tag{2.86}$$

$$n_{\epsilon,0} = \frac{n_\epsilon}{n_0 k_B T_0}. \tag{2.87}$$

The dimensionless electron energy density is defined as

$$\epsilon' = \frac{e}{k_B T_0}\epsilon \tag{2.88}$$

, which the ϵ is in unit of eV.

$$x' = \frac{x}{\lambda} \tag{2.89}$$

, where the characteristic length is the mean free path

$$\lambda = \frac{1}{n_0 \sigma_p}. \tag{2.90}$$

The characteristic time scale is thus defined as

$$t' = \frac{u_0}{\lambda}t. \tag{2.91}$$

The dimensionless diffusion and mobility coefficient are, respectively, defined as

$$D' = \frac{D}{\lambda u_0}, \tag{2.92}$$

and

$$\mu' = \frac{m_p u_0}{e\lambda}\mu \tag{2.93}$$

The ion flux, eq (2.65) , with drift-diffusion approximation can thus be non-dimensionalized as

$$\Gamma_{p,i+\frac{1}{2}} = -\frac{\lambda u_0 D'_{p,i+\frac{1}{2}}}{\lambda \Delta x'}\left[n_0 n'_{i+1}B(-X) - n_0 n'_i B(X)\right]. \tag{2.94}$$

$$\Gamma'_{p,i+\frac{1}{2}} = -\frac{D'_{p,i+\frac{1}{2}}}{\Delta x'}\left[n'_{i+1}B(-X) - n'_i B(X)\right]. \tag{2.95}$$

Similarly, the electron flux, eq (2.74), can be non-dimensionalized as

$$\Gamma'_{e,i+\frac{1}{2}} = -\frac{D'_{e,i+\frac{1}{2}}}{\Delta x'}\left[n'_{i+1}B(X) - n'_i B(-X)\right]. \tag{2.96}$$

With the above dimensionless expression for the flux, the general continuity equation can be non-dimensionalized as

$$\frac{n_0 u_0}{\lambda}\frac{\partial n'_{e,p}}{\partial t'} + \frac{1}{\lambda}\nabla' \cdot n_0 u_0 \mathbf{\Gamma'_{e,p}} = \frac{n_0 u_0}{\lambda} S'_{e,p}, \tag{2.97}$$

or

$$\frac{\partial n'_{e,p}}{\partial t'} + \nabla' \cdot \mathbf{\Gamma'_{e,p}} = S'_{e,p}. \tag{2.98}$$

The dimensionless electron energy density equation can e written as

$$\frac{u_0}{\lambda} n_0 k_B T_0 \frac{\partial n'_\epsilon}{\partial t'} + \frac{1}{\lambda} n_0 k_B T_0 u_0 \Gamma'_\epsilon = n_0 k_B T_0 \frac{u_0}{\lambda} S'_\epsilon \tag{2.99}$$

or

$$\frac{\partial n'_\epsilon}{\partial t'} + \nabla' \cdot \Gamma'_\epsilon = S'_\epsilon \tag{2.100}$$

where the dimensionless electron energy density source term is written as

$$S'_\epsilon = -\frac{\epsilon'}{e} S'_e - \Gamma_e \mathbf{E} \tag{2.101}$$

Finally, the dimensionless Poisson's equation is expressed as

$$\frac{1}{\lambda^2}\nabla'^2 \frac{k_B T_0}{e}\phi' = -\frac{1}{\epsilon_0}\sum_s q_s n_0 n_s \tag{2.102}$$

or

$$\nabla'^2\phi' = -\frac{\lambda^2 e^2 n_0}{\epsilon_0 k T_e}\sum_s (sign) n'_s \tag{2.103}$$

or

$$\nabla'^2\phi' = -\frac{1}{\epsilon'}\sum_s (sign) n'_s \tag{2.104}$$

where the dimensionless electron energy density is expressed as

$$\epsilon' = \frac{\epsilon_0 u_0^2 m_p}{\lambda^2 e^2 n_0} \tag{2.105}$$

2.3.3 Finite-difference Discretization

Finite differences method (FDM) is widely used in the field of Computational Fluid Dynamics (CFD), which is based on results of Taylor series expansion. One of the advantages of FDM is that it could be implemented easily, especially in the case of simple geometry. The error caused by the discretization process depends on the number of terms in the Taylor series which are kept. Generally, we can solve a PDE or a set of PDEs using the finite-difference method with dependent variables as functions of spatial coordinates and time in implicit, explicit, or semi-implicit approaches. The explicit approaches are relatively simple to implement; however, it is often suffered by the stability constraint, which is known as the Courant-Friedrichs-Lewy (CFL) condition, resulting in very small computational time step. In contrast, the implicit approaches are stable even for larger values of the time step. However, a system of algebraic equations must be solved at each time step using implicit techniques which is more complicated to implement and possibly more time-consuming. In this thesis, we descritize the fluid modeling equations through the use of finite-difference method. Since continuity equations for different species are similar, we only present the discretizations for the eqs. (2.57), (2.59), (2.61) in the following in turn . By employing the backward Euler scheme for time integration and the Sharfetter-Gummel scheme for representing the particle flux and after tedious algebraic rearrangement, the resulting discretized equation of a species continuity equation on a typical grid point (m, n) can be written as,

$$\frac{n^{t+\Delta t}_{\alpha,m,n} - n^{t}_{\alpha.m.n}}{\Delta t} + \frac{\gamma}{x_m}\Gamma^{t+\Delta t}_{\alpha,m,n} + \frac{\Gamma^{t+\Gamma t}_{\alpha,m+\frac{1}{2},n} - \Gamma^{t+\Delta t}_{\alpha,m-\frac{1}{2},n}}{\Delta x_m} + \frac{\Gamma^{t+\Gamma t}_{\alpha,m,n+\frac{1}{2}} - \Gamma^{t+\Delta t}_{\alpha,m,n-\frac{1}{2}}}{\Delta y_n} = \sum_{i=1}^{s_\alpha} S^{t+\Delta t}_{\alpha,m,n} \tag{2.106}$$

where α can be electrons, ion, and uncharged species, x_m is the distance from original point to grid point m, Δx_m and Δy_n are the step length at grid (m,n), γ is a factor using to deal with the coordinate system (for cylindrical coordinate is 1 and for Cartesian coordinate is 0) and Γ_α are the flux defined between grids which can be expressed in Scharfetter-Gummel form as,

$$\Gamma_{\alpha,m+\frac{1}{2}} = -\frac{D_{m+\frac{1}{2}}}{\Delta x_{m+\frac{1}{2}}}\left[n_{\alpha,m+1}B\left(-sign(q_\alpha)X_{m+\frac{1}{2}}\right) - n_{\alpha,m}B\left(sign(q_\alpha)X_{m+\frac{1}{2}}\right)\right] \quad (2.107)$$

$$\Gamma_{\alpha,n+\frac{1}{2}} = -\frac{D_{n+\frac{1}{2}}}{\Delta x_{n+\frac{1}{2}}}\left[n_{\alpha,n+1}B\left(-sign(q_\alpha)X_{n+\frac{1}{2}}\right) - n_{\alpha,n}B\left(sign(q_\alpha)X_{n+\frac{1}{2}}\right)\right] \quad (2.108)$$

where X is a non-dimensional variable define as,

$$X_{m+\frac{1}{2}} = \frac{\mu_{m+\frac{1}{2}}}{D_{m+\frac{1}{2}}}\left(\phi_{m+1} - \phi_m\right) \quad (2.109)$$

$$X_{n+\frac{1}{2}} = \frac{\mu_{n+\frac{1}{2}}}{D_{n+\frac{1}{2}}}\left(\phi_{n+1} - \phi_n\right) \quad (2.110)$$

and B is the Bernoulli function which is defined as

$$B(x) = \frac{x}{e^x - 1}. \quad (2.111)$$

The electron energy equation is descritized as

$$\frac{3}{2}\frac{n^{t+\Delta t}_{e,m,n}T^{t+\Delta t}_{m,n} - n^{t}_{e,m,n}T^{t}_{m,n}}{\Delta t} + \frac{\Gamma}{x_m}\Gamma^{t+\Delta t}_{e,m,n} + \frac{\Gamma^{t+\Delta t}_{e,m+\frac{1}{2},n} - \Gamma^{t+\Delta t}_{e,m-\frac{1}{2},n}}{\Delta x_m} + \frac{\Gamma^{t+\Delta t}_{e,m,n+\frac{1}{2}} - \Gamma^{t+\Delta t}_{e,m,n-\frac{1}{2}}}{\Delta y_n} =$$
$$-\vec{\Gamma}^{t+\Delta t}_{e,m,n}\cdot\vec{E}^{t+\Delta t}_{m,n} - \sum_{i=1}^{S_\epsilon}\epsilon_i S^{t+\Delta t}_{\epsilon_i,m,n} + 3\frac{m_e}{M}n_e k_B\nu_m\left(T^{t+\Delta t}_{e,m,n} - T_g\right) \quad (2.112)$$

where T_e and ϵ_i are in unit of eV, ν_m is the electron collision frequency, and the descretized form energy fluxes Γ_ε are expressed as

$$\Gamma_{\varepsilon,m+\frac{1}{2},n} = \frac{5}{2}T_{e,m+\frac{1}{2},n}\Gamma_{e,m+\frac{1}{2},n} - \frac{5}{2}\frac{n_{e,m+\frac{1}{2},n}T_{e,m+\frac{1}{2},n}}{m_e\nu_m}\frac{T_{e,m+1,n} - T_{e,m,n}}{\Delta x_m} \quad (2.113)$$

$$\Gamma_{\varepsilon,m,n+\frac{1}{2}} = \frac{5}{2}T_{e,m,n+\frac{1}{2}}\Gamma_{e,m,n+\frac{1}{2}} - \frac{5}{2}\frac{n_{e,m,n+\frac{1}{2}}T_{e,m,n+\frac{1}{2}}}{m_e\nu_m}\frac{T_{e,m,n+1} - T_{e,m,n}}{\Delta y_n}. \quad (2.114)$$

Finally, the Poisson's equation is discretized as

$$\frac{\gamma\varepsilon_m}{2x_m\Delta x_m}\left(\phi^{t+\Delta t}_{m+1} - \phi^{t+\Delta t}_{m}\right) + \frac{1}{\Delta x^2_m}\left(\varepsilon_{m+\frac{1}{2}}\left(\phi^{t+\Delta t}_{m+1} - \phi^{t+\Delta t}_{m}\right) - \varepsilon_{m-\frac{1}{2}}\left(\phi^{t+\Delta t}_{m} - \phi^{t_\Delta t}_{m-1}\right)\right)$$
$$+ \frac{1}{\Delta y^2_n}\left(\varepsilon_{n+\frac{1}{2}}\left(\phi^{t+\Delta t}_{n+1} - \phi^{t+\Delta t}_{n}\right) - \varepsilon_{n-\frac{1}{2}}\left(\phi^{t+\Delta t}_{n} - \phi^{t_\Delta t}_{n-1}\right)\right)$$
$$= -\sum_{i=1}^{n_\alpha} sign(q_\alpha)q_\alpha n_\alpha \quad (2.115)$$

2.3.4 Boundary Conditions

Boundary condition for electrons is applied on the electron flux to the wall as

$$\mathbf{\Gamma}_{e,BC} = \frac{1}{4} n_e v_{e,th} - D_e \nabla n_e - n_e \mu_e \mathbf{E} - \sum_i \gamma_i \mathbf{\Gamma}_i \tag{2.116}$$

where γ_i is the secondary emission coefficient when ion species i bombarding on the wall and the electron thermal velocity

$$v_{e,th} = \sqrt{\frac{8 k_B T_e}{\pi m_e}}. \tag{2.117}$$

The diffusion and drift terms of electron are considered only when the flux direction is to the wall. The electrons moving to the wall are removed while on the dielectric wall the charges are added to the net charge and are accumulated during runtime. Boundary condition for ions is also applied on the ion flux to the wall

$$\mathbf{\Gamma}_{i,BC} = -D_i \nabla n_i - n_i \mu_i \mathbf{E} \tag{2.118}$$

where drift term of ion is considered only when the direction is to the wall. Similarly, the ion moving to the conductor wall are removed while on the dielectric wall the charge are added to the net charge and are accumulated during runtime.

For the non-excited and non-radical neutral species, Neumann boundary condition is employed at all solid walls. However, boundary condition for the excited or radical species is assumed to be

$$\mathbf{\Gamma}_{p,BC} = -D_p \nabla n_p \tag{2.119}$$

where the resulting species on the wall is removed. Finally, the boundary condition of electron energy density equation is expressed as

$$\mathbf{\Gamma}_{\epsilon} = 2 k_B T e \mathbf{\Gamma}_e. \tag{2.120}$$

2.3.5 Newton-Krylov-Schwarz (NKS) Algorthm

In this thesis, the parallel fully coupled Newton-Krylov-Swartz(NKS) algorithm [Cai et al., 1998a] was employed to solve the large sparse system of nonlinear discretized equations, which were derived in the previous section. All the functionals for each dependent variables form a

global functional vector. Jacobian matrix is then computed based on this global vector. Nevertheless, this treatment results in a fully implicit scheme, which may allow larger time step as compared to semi-implicit or explicit scheme. Another advantage of solving the coupled equations directly, rather than solving the equations one by one or some heuristic way of coupling, is that it can have better time accuracy with appreciable time-step size and much better parallel performance since the grain size is much larger. In this method, an inexact Newton method is used to solve the coupled nonlinear discretized equations at each time step. The resulting Jacobian system computed by using a hydrid analytical and numerical (finite difference) for the Newton corrections are solved with a preconditioned Krylov subspace type method, relying directly only on iterative operations. With the use of hybrid analytical and numerical scheme, the time required for evaluating Jacobian matrix is reduced greatly. The Krylov method requires preconditioning for achieving acceptable convergence speed of inner interactions. A good preconditioner saves time and memory by allowing small number of iterations in the Krylov loop and smaller storage for the Krylov subspace. In this study, we have utilized a parallel additive Schwarz(AZ) type preconditioner with an inexact or exact solver such as incomplete LU(ILU) or LU factorizations in each subdomain. It was shown that this AS preconditioner can greatly reduce the runtime required for inner iterations in an inexact Newton method [Hwang and Cai, 2005]. This results from that the smaller subdomain blocks maintain better cache residency and shorter convergence time for an approximate solver. In addition, either scheme was used to solve the preconditioned matrix equation at each time step. By combining the AS preconditioner with Krylov type subspace method BiCG-STAB(or BCGS) [van der Vorst, 1992] or GMRES [Saad and Schultz, 1986] in the present study within an inexact Newton method leads to a coherent fully parallel solver: Newton-Krylov-Schwarz(NKS) algotithm [Cai et al., 1998b].

In practical implementation, we employed the PETSc package [Balay et al., 2001], which features distributed data structure - index sets, vectors, and matrices - as functional objects. Iterative linear and nonlinear solvers are combined modularly, recursively, and extensively through a uniform application programmer interface. In addition, the Jacobian system within the inexact Newton method can be computed automatically by the finite-difference scheme within the PETSc framework or by the user himself/herself. Portability is achieved through MPI, which is a standard in message passing among processors nowadays, although the details are not requires

in practical coding. All the codes were programmed in C/C++.

Chapter 3

Verifications and Parallel Performance of the Fluid Modeling Code

To validate the developed fluid modeling code, we have conducted several simulations in one-dimensional and two-dimensional cases and results were compared with experimental data and previous simulations wherever possible. For the one-dimensional cases, they include: (1) helium discharge driven by RF power source, (2) helium discharge driven by AC power source and (3) nitrogen discharge driven by AC power source. For the two-dimensional case, a GEC chamber-scale simulation was conducted. At the end of Chapter 3, parallel performance of the developed parallel fluid modeling code is presented using the 2D-axisymmetric GEC chamber-scale simulation. These validations and parallel performance were described in the following in turn.

3.1 One-Dimensional Simulation of Helium Discharge Driven by a Radio-Frequency Power Source (13.56 MHz)

3.1.1 Simulation Conditions

A one-dimensional fluid modeling which mimics a parallel-plate atmospheric-pressure driven by a radio-frequency power source (13.56 MHz) was conducted and validated with experimental data obtained in our group. Corresponding test conditions include: two electrodes of area $25\ cm^2$ covered by dielectric layers with thickness of $1\ mm$ each and relative permittivity of 11.63, power electrode applying a sinusoidal voltage waveform having frequency of 13.56 MHz and peak-to-peak voltage of $496\ V$, discharge gap of $1\ mm$, and background gas pressure of $760\ Torr$.

3.1.2 Plasma Chemistry

This simulation employed a "complex" set of Helium reaction channels as summarized in Table 4.1, which includes 7 species (electron, He_m^*, He_{ex}^{**}, He_2^*, He^+, He_2^+, He) and 27

reaction channels. This set of helium plasma chemistry includes momentum transfer collision (0), electron impact excitations (1)-(7), direct ionization (8)-(9), electron impact de-excitation (10), electron impact dissociation (11), electron-ion recombination (12) (15)-(16), electron-ion dissociative recombination (13)-(14), Hombeck-Molnar associative ionization (17), metastable - metastable associative ionization(18), metastable - metastable ionization (19), ion conversion (20), metastable - induced association (21), metastable - induced dissociative ionization (22), metastable-induced ionization (23), dimer - induced dissociative ionization (24), dimer-induced ionization (25), helium-atom induced dissociation (26).

3.1.3 Validation with Experiment Results

Figure 3.1 shows the comparison of the simulated discharged currents with the measured data that was obtained in our group. It clearly shows that the present fluid modeling code using the complex helium plasma chemistry can predict quantitatively the temporal evolution of discharge current of helium RF discharge very well.

3.2 One-Dimensional Simulation of Helium Dielectric Barrier Discharge Driven by AC Realistic Distorted Sinusoidal Voltages

3.2.1 Simulation Conditions

A one-dimensional fluid modeling which mimics a parallel-plate atmospheric-pressure driven by a distorted sinusoidal AC power source was conducted and validated with experimental data obtained in our group. Corresponding test conditions include: two electrodes of area $25\ cm^2$ covered by dielectric layers with thickness of $1\ mm$ each and relative permittivity of 12, power electrode applying a distorted sinusoidal voltage waveform having frequency of 60 KHz and peak-to-peak voltage of 14000 V, discharge gap of $2.5\ mm$, and background gas pressure of $760\ Torr$.

3.2.2 Plasma Chemistry

Again, we have applied the same set of "complex" Helium plasma chemistry as the previous RF helium discharge.

3.2.3 Validation with Experiment Results

Figure 3.2 shows the comparison of the simulated discharged currents with the measured data that was obtained in our group. It clearly shows that the present fluid modeling code using the complex helium plasma chemistry can predict quantitatively the temporal evolution of discharge current of helium DBD very well.

3.3 One-Dimensional Simulation of Nitrogen Dielectric Barrier Discharge Driven by AC Realistic Distorted Sinusoidal Voltages

3.3.1 Simulation Conditions

Similar to those test conditions as described in Section 3.1.1 for the helium RF discharge, one-dimensional fluid modeling is conducted for the same configuration using pure nitrogen gas, which was driven by a distorted sinusoidal power source (60 kHz) with a gap distances of $0.5\ mm$.

3.3.2 Plasma Chemistry

The nitrogen plasma chemistry employed in the present study includes 9 species (electron, N_2, N_2^+, N_4^+, $N_2(X^1\Sigma_g^+, \nu = 1-8)$, $N_2(A^3\Sigma_u^+)$, $N_2(B^3\Pi_g)$, $N_2(C^3\Pi_u)$, and $N_2(a'^1\Sigma_u^-)$), and 31 reaction channels, which are summarized in Table 3.1. This set of nitrogen plasma chemistry includes direct ionization (1), excitation into excited, metastable and vibration states (5), de-excitation (6), recombination (3), associative ionization (3), light emission from excited, metastable states (4) and excitation into vibration states (10). Note we have ignored the N^+ and N_3^+ in the simulation since they have been found to unimportant in nitrogen plasma simulation [Choi et al., 2006].

3.3.3 Validation with Experiment Data

Figure 3.3 shows that comparison of simulated and measured discharged currents of nitrogen DBD driven by a quasi-pulsed power (60 kHz) for different gap distances (0.5, 0.7, 1.0 and 1.2 mm) along with the experimental photo images (0.2 sec exposure time) of discharge

on the right. Note the measured relative permittivity and thickness of the ceramic material is 11.63 and $1\ mm$, respectively. In general, the simulations agree very well quantitatively with the experimental data for the cases of $d = 0.5\ mm$ and $0.7\ mm$, but begin to deviate slightly from the measurements as $d = 1.0\ mm$ and exhibit large discrepancy with the measurements as $d = 1.2\ mm$. For the cases of smaller gap (0.5, 0.7 and 1.0 mm), the simulations demonstrate they are typical homogeneous Townsend-like discharges with much fewer electrons than ions (not shown here). For the case of larger gap ($d = 1.2\ mm$), the simulation shows it is a glow-like discharge (quasi-neutral in the bulk) with very high current density during the breakdown phase. However, this is obviously against the measurements. This is attributed to the fact that the discharge has transitioned from Townsend-like to filamentary-like (microdischarge), as shown in the photo images in Figure 3.3, which makes the one-dimensional fluid modeling invalid. This shows that one has to be very cautious about the use of one-dimensional fluid modeling for simulating parallel-plate nitrogen DBD. In ref. [Choi et al., 2006], the conclusion of transition from Townsend-like to glow-like discharge was misleading without the validation of experiments. To capture the correct physics with a larger gap, one should employ at least two-dimensional fluid modeling, which is currently in progress and will be reported elsewhere in the near future.

Figure 3.4 shows the spatial-average temporal discharge properties as $d = 0.7mm$. Results clearly demonstrate that the total number density of ions (N_2^+ and N_4^+) is always larger than electron number density throughout a cycle. The simulated electric field across the gap is almost linear without any distortion by the charge density at all times during a cycle (not shown here). Both the above two phenomena show that this is a typical Townsend-like discharge. In addition, N_2^+ is found to be most abundant during the breakdown process (same period of those current peaks in Figure 3.3), while N_4^+ is found to be dominant after the breakdown caused by the associative ionization of excited/metastable nitrogen species.

3.4 Two-dimensional Helium Discharge Simulation in a Gaseous Electronics Conference (GEC) Reference Cell

3.4.1 Simulation Conditions

A GEC discharge simulation is conducted for validating the two-dimensional fluid modeling code as developed in the thesis. The simulation conditions are summarized as follows. The power and grounded electrodes are both 2 inches in radius, the electrode gap is 1 inch in length, the applied peak-to-peak voltage is 150 V, the radio frequency is 13.56 MHz, and the background gas is pure helium at 500 mTorr. This validation employed a "complex" set of Helium reaction channel listed in Table 4.1, in which the details are discussed in Chapter 4. Gas temperature is assumed to be $400\ K$. A non-uniform grid and the total of 200 time steps per RF cycle are employed. Additive Swartz with a minimal overlapping and LU as a subdomain solver were used. The relative stopping condition of the Newton method and the Krylov subspace method were $10\times^{-5}$ and $10\times^{-4}$, respectively.

3.4.2 Validation with Experimental Data

The numerical simulations of the cycle averaged parameters are shown in Figure 3.5, including (a) electron, (b) He^+, (c) He_2^+, (d) He_2^*, (e) He^*, and (f) He_{meta}. The results indicate that the maximum value occur near the outer edge between two electrode gaps, where the electric field is the strongest. In addition, the dominant ion species are the molecular ions, rather than the atomic ions. Similar observations were found in the previous study [Martens et al., 2007b].

Figure 3.6 shows a comparison of the simulated peak electron densities with the theoretical prediction and the experimental data [Riley et al., 1994] for various applied voltages. Note that only the 1-D electron Boltzmann equation was used for the theoretical prediction, which was questionable for the present 2-D case. Thus, the data were included for reference only. In general, the simulation data followed the trend of the measurements reasonably well, except for the lowest (50 V) and the highest (200V) cases. Note that the electron densities were measured by a microwave interferometer probing through the center along the radial direction at the midpoint between the electrodes by integrating the data along the line-of-sight path. The data were only

correct if the densities were uniform throughout the microwave path, which was obviously not true for the current test cases. Nevertheless, the simulated data were in reasonable agreement with the measurements.

3.5 Parallel Performance Test of Fluid Modeling Code

3.5.1 Test Conditions

The simulation conditions used for parallel performance studies are similar to those for the validation of the parallel 2D-axisymmetric fluid modeling code, except that we now consider a 122×123 uniform grid and $200\ V$ of peak-to-peak value of applied voltage. 400 timesteps per RF cycle were used throughout the simulation. We investigated the parallel performance of the solver by using two types of Krylov subspace method, GMRES and BiCGStab in conjunction with standard AS preconditoners, where the subdomain problems were solved by either the LU decomposition or ILU(0) (incomplete LU decomposition with zero level fill in). All the calculations were done on the V'ger cluster system (Xeon 3GHz, dual core, dual CPU) at the Center for Computational Geophysics, National Central University, Taiwan.

3.5.2 Results and Discussion

Figure 3.7 illustrates the parallel performance including speedup analysis and runtime per time step as a function of the number of processors. In the parallel computing we have applied either GMRES or BiCGStab as the KSP solve and LU of iLU as sub-domain solve. Runtime per timestep was calculated by averaging the total time of 5000 timesteps. The cases of 96 processors using GMRES or BiCGStab with iLU combination performs the best. Generally, resulting speedup shows a typical super-linear behavior when the number of processors is in the range of 32$\tilde{1}$44 except the case of BiCGStab linear solve with LU preconditioner.

3.6 Brief Summary of This Chapter

In Chapter 3, several validations of the fluid modeling codes by comparing with experimental data or previous simulations and parallel performance were presented. Results show that the developed fluid modeling code is able to predict one- and two-dimensional atmospheric-

and low-pressure gas discharges very accurately. Superlinear speedup up to 144 processors of the parallel fluid modeling code with proper selection of the simulation parameters was also demonstrated.

Chapter 4

One-Dimensional Simulation of Helium Dielectric Barrier Discharge Driven by AC Realistic Distorted Sinusoidal Voltages

This chapter discusses the effects of selecting plasma chemistry in simulations of helium DBD by comparing simulations with experimental results. Simulated temporal discharged currents using the complex plasma chemistry are in excellent agreement with the measurements obtained in the present study, which validates the fluid modeling code. It also indicates that the inclusion of heavy particle related reactions is critical in accurately predicting the helium DBD because of the slow varying electric field in the range of the tens of kilohertz. Detailed temporal variations of spatial-average plasma properties are discussed by partitioning in time.

4.1 Background and Motivation

Atmospheric-pressure plasmas (APP) have attracted tremendous attention in the past two decades mainly because of: (1) without the use of vacuum equipment, and (2) increasingly numerous applications in modern science and technology. The former drives the cost down dramatically as compared to those which have been using in materials processing and also offer the possibility of in-line processing in industry. The latter may include surface cleaning, surface modification, thin film deposition, etching, biological decontamination, ozone generation, pollution control, flat plasma display panels, and gas lasers, to name a few.

Types of APP are generally classified based on the power sources, which may include radio frequency (RF) capacitively coupled discharge, AC dielectric barrier discharge (DBD) and microwave discharge. Among these, helium DBD may represent one of the most popular discharges because of their easier implementation and numerous applications. In addition to experimental diagnostics, the fluid modeling has been proved to be a very useful tool in understanding the plasma physics and chemistry of helium discharges. Indeed, the outcome of fluid modeling strongly depends on the selection of the plasma chemistry and other parameters such as transport coefficients, in addition to the numerical accuracy of the simulation itself. Thus, in this chapter we intend to present the effect of selecting simple and complicated plasma chemistry

on simulating helium DBD driven by a realistic bipolar pulsed power supply using fluid modeling by comparing with experimental data and to elucidate the underlying physics based on the simulation data.

In this chapter, the parallel-plate helium dielectric barrier discharge (DBD) driven by a realistic 20 KHz bipolar quasi-pulse voltage waveform has been investigated by means of simulations and compared with experimental data obtained in-house from our group. A self-consistent one-dimensional fluid modeling code considering the non-local electron energy balance was applied to simulate the helium DBD. Effect of selecting plasma chemistry on simulations of helium DBD was investigated by comparing simulations with experiments. Results show that the simulations, which include more helium related reaction channels, can faithfully reproduce the measured discharged temporal current quantitatively. Based on the simulated discharge properties, we have found that there is complicated mode transition of discharges from the long secondary Townsend like to the dark current like, then to short primary Townsend like and to short secondary Townsend like forthe helium DBD that is driven by a realistic bipolar AC quasi-pulsed power source.

Types of APP are generally classified based on the power sources, which may include radio frequency (RF) capacitively coupled discharge, AC dielectric barrier discharge (DBD) and microwave discharge. Among these, helium DBD may represent one of the most popular discharges because of their easier implementation and numerous applications. In addition to experimental diagnostics, the fluid modeling has been proved to be a very useful tool in understanding the plasma physics and chemistry of helium discharges. Indeed, the outcome of fluid modeling strongly depends on the selection of the plasma chemistry and other parameters such as transport coefficients, in addition to the numerical accuracy of the simulation itself. Thus, in this paper we intend to present the effect of selecting simple and complicated plasma chemistry on simulating helium DBD driven by a realistic bipolar pulsed power supply using fluid modeling by comparing with experimental data and to elucidate the underlying physics based on the simulation data.

In the literature, there are many fluid modeling studies on the topics of helium DBD under atmospheric-pressure condition. On one hand, in the case of RF AP discharge, one-dimensional

fluid modeling was often used to elucidate the plasma physics by varying parameters such as gap distance, amplitude of sinusoidal voltage, frequency of sinusoidal voltage, mixture of impurities and secondary electron emission coefficient [Park et al., 2001; Yuan and Raja, 2003, 2002; Shang et al., 2008; Chirokov et al., 2009; Wang et al., 2006]. In these studies, very simplified helium plasma chemistry was used and generally was in reasonable agreement with experimentally measured discharge currents. On the other hand, in the case of AC DBD, one-dimensional fluid modeling was also often used to study the discharge physics by parametric studies. These include changes of gap distance, dielectric thickness, dielectric permittivity, amplitude and frequency of sinusoidal voltage in the range of 10-130 kHz, mixture of impurities, voltage waveform (e.g., pulsed or others), and secondary electron emission, among others [Kanazawa et al., 1988; Massines et al., 1998; FumiyoshiTochikubo et al., 1999; Mangolini et al., 2004; Golubovskii et al., 2003; Bartnikas et al., 2007; Martens et al., 2007a,b; Wang et al., 2009]. In these studies, relatively complicated helium plasma chemistry was adopted to simulate the discharge physics. These plasma chemistries generally included more reaction channels related to excited and metastable helium. Results generally followed the trends of the experimental data, although quantitative comparison is still not favorable to the best knowledge of the authors.

There seems no previous study focusing on the detailed comparison of the selection of plasma chemistry in fluid modeling of helium DBD driven by a realistic quasi-pulsed power source and its direct validation by comparing with the experimental data, although this is important in conducting useful fluid modeling for this type of discharge. Thus, it is the objective of this present study to present effect of selecting plasma chemistry in helium DBD simulations and to compare the simulation with experimental data. In this chapter, we will show the simulation of helium plasmas DBD driven by bipolar quasi-pulsed 20 kHz power source using simple and complicated plasma chemistry, respectively, and compare with experimental discharge currents obtained in the present study. In addition, several temporal and spatial distributions of important properties are presented to explain in detail the effect of selecting helium plasma chemistry. Results show that inclusion of more excited and metastable species related channels into the plasma chemistry is critical in predicting the correct discharge currents in the fluid modeling of helium DBD.

4.2 Helium Plasma Chemistry

For the simulation, we have considered two sets of plasma chemistry (termed as "simple" and "complicated"), which are summarized in Table 4.1 and schematically sketched in Figure 4.1 for easy visualization. For the simple plasma chemistry, we have considered 6 species and 10 reaction channels, which have been used frequently and successfully for RF discharge simulations. They include 6 species (electron, He_m^*, He_2^*, He^+, He_2^+, He) and 10 reaction channels. For the complicated plasma chemistry, we have considered 7 species (electron, He_m^*, He_{ex}^{**}, He_2^*, He^+, He_2^+, He) and 27 reaction channels, with one more species (He_{ex}^{**}) as compared to the simple one. In general, the complicated plasma chemistry includes more reaction channels related to heavy particles, referring to Table 4.1, such as Ion-e recombination (12), ion-electron dissociative recombination (14), ion-electron recombination (15,16), Hornbeck-Molnar associative ionization (17), metastable-metastable associative ionization (18), metastable-induced dissociative association (22), Metastable-induced association (23), dimer-induced dissociative ionization (24), dimer-induced ionization (25), He-atom induced dissociation (26). The transport coefficients and the rate constants related to electron are calculated by solving the Boltzmann equation (BOLSIG+). Note these coefficients were predicted and stored in a lookup table as a function of electron temperature. The transport coefficients (mobility and diffusivity) of ions (H^+ and He_2^+) are adopted from those experiments by Mason et al. (1976) as a function of reduced field (E/N) and are calculated assuming species transport in helium background gas at a temperature $400\ K$. As for the diffusion coefficient of neutral species (atomic and molecular helium), they are the same as [Yuan and Raja, 2003].

4.3 Simulation Conditions

A planar atmospheric-pressure DBD as the sketch in Figure 4.2 conducted by our group member consists of two parallel copper electrodes (50 × 50 × 8 mm each) and each of the electrodes was covered with a 70 × 70 × 1 mm ceramic plate with measured relative permittivity of 11.63. Distance between the two dielectric plates was kept at 1 mm throughout the study. This DBD assembly was driven by a quasi-pulsed power supply (Model Genius-2, EN technologies Inc.) at a fixed frequency of 20 kHz and input power from the power supply

was fixed at 500 W. Input voltage and output current waveforms across the electrodes of the parallel-plate discharge were measured by a high-voltage probe (Tektronix P6015A) and a Rogowski coil (IPC CM-100-MG, Ion Physics Corporation Inc.), respectively, through a digital oscilloscope (Tektronix TDS1012B). The measuremented voltage waveform was obtained and then used as input condition in the fluid modeling. Pure helium gas is at pressure $760\ Torr$ with the reaction channels and species introduced in Section 4.2.

4.4 Results and Discussion

4.4.1 Comparison of Discharged Current between Simulation and Experiment

The input voltage waveform for simulations was obtained by Fourier series expansion of the measured voltage waveform across the electrodes using 50 terms of sine and cosine functions with 20 KHz as the fundamental frequency. In general, this fitting method can be applied to any arbitrary realistic voltage waveform. The simulated temporal discharge currents along with the measurements are presented in Figure 4.3. Results show that the predicted temporal currents using the complex plasma chemistry are in excellent agreement with the measurements; while those using the simple plasma chemistry fail to reproduce the measurements during some periods in a cycle. These regions of discrepancy include over-prediction of major discharge current peaks and under-prediction between major current peaks. This implies that inclusion of the excited and metastable helium related reaction channels is responsible for the successful fluid modeling of the helium AC DBD, which is different from the simulation of the helium RF discharge under atmospheric-pressure condition that application of the simple plasma chemistry was able to reproduce the experimental data under similar geometry ($1\ mm$ gap with $1\ mm$ ceramic dielectrics). In the Figure 4.4a shows that, in the helium RF discharge, most of the electrical power input is absorbed by the electrons in the plasma bulk region, similar to that in low-pressure condition, since the oscillating frequency of the voltage is very fast and the electrons are unable to drift to the dielectric surfaces in such a short period of time before applied voltage changes direction. However, in the helium AC DBD, it is a typical Townsend discharge most of the time during a cycle period (current density $\sim 10 mA/cm^2$ in Figure 4.3 and in Figures 4.5-4.8), because most of the electrons are able to drift away in the gap to hit

the dielectric surfaces with a small gap ($1\ mm$) during a half cycle. This makes most of the electrical power absorbed by the ions (He_2^+), rather than by the electrons as in helium RF case. In brief summary, the present fluid modeling code using the complex plasma chemistry can predict quantitatively the temporal evolution of discharge current of helium DBD driven by an AC bipolar quasi-pulsed power source very well, which is rarely reported in the literature. This quantitative validation provides us the confidence in interpreting the discharge physics of helium DBD based on the simulations using the complex plasma chemistry, which are presented next.

4.4.2 Spatial Profiles of Cycle-averaged Plasma Properties

Figure 4.9 shows the cycle-average spatial power absorption by the plasma, respectively, through various mechanisms. It shows that the molecular ions (He_2^+) absorb much more power than the electrons do near both the dielectric surfaces, which is caused by the much higher concentration of the molecular ions than that of the electrons, as can be seen clearly in Figure 4.10. Figure 4.10 illustrates the cycle-average spatial distribution of various plasma properties. It shows that the cycle-average number density of He_2^+ is much higher than that of the electrons ($\sim$ 1 order) and He^+ (2-3 orders), which leads to the observation that power absorption by the electrons and He^+ is very small and essentially negligible, respectively. This also confirms that it is a typical Townsend discharge in the average sense. This was also obtained by the early high pressure helium experiments. The abundant He_2^+ is formed through ion conversion channel ($He^+ + 2He \rightarrow He_2^+ + He$) which was first found by Phelps and Brown [Phelps and Brown, 1952]. The average electron temperature is nearly uniform across the gap and is as high as $5.4\ eV$. The two most populated neutral species are He_m^* and He_2^* ($He_2^* > He_m^* >> He_{ex}^{**}$) mainly due to a series of ion-electron recombination, in addition to the direct electron-impact excitation, as shown in Table 4.1.

4.4.3 Temporal Variation of Spatial-average Plasma Properties

Figure 4.11 shows the temporal variation of the power absorption through various mechanisms similar to those presented in Figure 4.9. Again it shows that molecular helium ions absorb most of the electrical power input the quasi-pulsed power source at any instant during a

typical cycle. Figure 4.12 shows a series of temporal variation of several important discharge parameters in a cycle, which include: a) the applied voltage, discharge current, dielectric voltage, gap voltage, and accumulated charge densities on both power and ground electrodes using the complex plasma chemistry, b) the spatial-average concentrations of charged particles and electron temperature using the complex plasma chemistry, and c) the spatial-average concentrations of charged particles and electron temperature using the simple plasma chemistry. We have divided the first half cycle (rising voltage period) into several distinct modes of discharge, which include long Towsend like region (region A), dark current like (region B), primary short Towsend like discharge (region C), and secondary short Towsend like discharge (region D), for the convenience of discussion described next. Figure 4.12a shows that the gap voltage has very strong "memory effect" because of the shielding caused by the accumulated charges on the dielectric surfaces. Also the dielectric voltage is almost the same across both dielectrics, in which we have plotted only one for clarity. It is also clear that the temporal variation of the accumulated charges on the ground electrode correlate very well with the change of dielectric voltage. This is attributed to the linearity of the electrostatic Poisson equation. The surface charges at the dielectric surface of the ground electrode contribute to the volumetric charge density (source term of the Poisson equation) and thus influence the potential distribution near the interface in a linear fashion. Interestingly, the magnitudes of the surface charges at both dielectric surfaces are almost the same with opposite signs. In Figure 4.12b, they show that the molecular helium ions (max. $10^{17}m^{-3}$) are the most dominant species at any instant (regions A, C and D), instead of the atomic helium ions, except in the early stage of region B, where the electrons are approximately the same amount as the molecular helium ions. This is attributed to the pronounced Hornbeck-Molnar associative ionization (No. 17 in Table 1). However, in Figure 4.12c (simple plasma chemistry), the concentration of the molecular helium ions in region A becomes much smaller than that by using the complex plasma chemistry. This reduces the discharge current as shown earlier in Figure 4.3 by using the simple plasma chemistry, which deviates very much with the experimental data in this region. Reason behind this observation will be explained later. In regions A, C and D, they are all typical Townsend-like discharges, in which the concentration of the ions are much more than that of the electrons with very high electron temperature of $\sim$7 eV. In addition, region B is termed as dark current like region because of the quasi-neutrality

in the plasma bulk, the very low discharge current ($< 1mA/cm^2$) and the very low electron temperature. Typical detailed distribution of the discharge parameters in each region will be presented next to elucidate the underlying physics.

4.4.3.1 Region A - Long Townsend like region

In this region A, the gap voltage decreases with time because of the memory effect as mentioned earlier, although the applied voltage increases with time (Figure 4.12a). The magnitude of maximum current density is $\sim 2mA/cm^2$, which is a typical characteristics of Townsend discharge and the temporal width is $\approx 15\ \mu s$ in region A. It is termed as "long" because it lasts for $15\ \mu s$ for a cycle period of $50\ \mu s$. Snapshots of plasma properties and source/sink terms of electron related channels are shown in Figure 4.5a and Figure 4.5b, respectively, as the applied voltage reaches 1,150 volts. At this instant, the electrons and ions are attracted to the anode and cathode, respectively, and the average electron temperature is as high as 7 eV (Figure 4.12). In general, the electron density is far less than the molecular helium ion density across the gap, except in the small region near the anode, which is a typical characteristic of a Townsend like discharge. Similar to those presented in Figure 4.10 for the cycle-average data, the densities of excimer (He_2^*) and metastable (Hem*) helium are in the range of $10^{18} - 10^{19}m^{-3}$, which are 2 and 3-4 orders of magnitude larger than the density of molecular helium ions and electrons, respectively. However, the excited atomic helium (He_{ex}^{**}) is much smaller and in the order of $10^{14}m^{-3}$. Note the life time of the excited atomic helium is very short and is easily de-excited which can emit visible fluorescence. In Figure 4.5b, source terms of the heavy particle related channels are presented, which show that abundant electrons can be produced through these channels. In turn, these electrons generate abundant molecular helium ions through channels like the electron impact and the Hornbeck-Molnar associative ionization, which are otherwise impossible by using the simple plasma chemistry (comparing Figure 4.12b and Figure 4.12c). The electron impact channels generate abundant excited and metastable helium, while the Hornbeck-Molnar associative ionization leads to the creation of plenty molecular helium ions as found in this region. Thus, the use of complex plasma chemistry by including more heavy particle related channels in the fluid modeling can faithfully reproduce the experimental discharge current in the region A.

4.4.3.2 Dark current like discharge

In region B, the gap voltage decreases decreasing applied voltage and the magnitude of maximum current density is only ¡ 1mA/cm2, which is even smaller than the current in the previous long secondary Townsend-like discharge (Figure 4.12a). This region lasts for only $\approx 4\ \mu s$. Snapshots of plasma properties and source/sink terms of electron related channels are shown in Figure 4.6 as the applied voltage reaches $\approx 2,000\ volts$. At this instant, a clear quasi-neutral plasma bulk region with very high plasma density in the order of $10^{17} m^{-3}$ having $\approx 0.5\ mm$ in width is formed in the center of the gap; however, the electron temperature becomes very low, except near the sheath ($\approx 2\ eV$). The sheath potential is very small since the positive charge density is very low resulting from the very low ion density (e.g., $10^{17} m^{-3}$ at the cathode side). The electrons in the bulk are not accelerated to gain energy because the electric field across the gap is very small (Figure 4.6a) at this instant. This leads to the rapid disappearance of short-lived excited helium (He^{**}_{ex}), which requires energetic electrons to "pump up" their population at higher energy states (Figure 4.6a). However, the metastable and excimer helium are still as abundant as those in region A because they are relatively long-lived as compared to the excited helium. After this instant, the recombination of electrons and molecular ions depletes their population very soon, as can be seen in the later half of this period in region B (Figure 4.12b). In addition, Figure 4.6b shows that the electron impact related reactions and the Hornbeck-Molnar associative ionization become unimportant because of very low-energy electrons. By summing up the above observations, we can conclude that it is a dark current like, instead of a glow like, discharge in region B because of the very small discharge current, the very small amount of short-lived excited helium and the very low electron temperature, although abundant charged species still exist in the gap.

4.4.3.3 Primary short Townsend like discharge

In region C, the gap voltage increases rapidly initially from -250 volts up to ≈ 750 volts and remain at this voltage for a period of $2 - 3\mu s$ because of shielding from the negative and positive accumulated charges on dielectric surface of anode and cathode, respectively, although the applied voltage keeps increasing with time (Figure 4.12a). The magnitude of the maximal discharge current is about $\sim$8 mA/cm2 and the electron density is much less than the ion density

(especially the molecular ion); while the electron temperature is relatively high (∼7 eV on the average) (Figure 4.12b). Snapshots of plasma properties and source/sink terms of electron related channels are shown in Figure 4.7a as the applied voltage is at $\sim 3,000\ volts$, where the discharge current is peaked. The discharge phenomena are very similar to those described in region A; however, this is termed as "primary short" because of the period of the discharge is shorter ($3-4\mu s$) and the discharge current is much larger. This short and large discharge current is mainly caused by the very large rate of increase of the applied voltage (pulse; from ∼1,500 to ∼3,000 volts in less than $1\ \mu s$), which in turn causes the gap voltage increases in a similar fashion. This rapid increase of the voltage attracts a large amount of electrons and molecular ions to move very fast towards the anode and cathode, respectively. The rapid drop of the discharged current is mainly because faster accumulation of electrons at the dielectric surface (anode side), which quickly shields the applied voltage and then after this short current peak the gap voltage keeps at approximately constant by the balance of electron accumulation (slowing decrease of the gap voltage) and increase of applied voltage. Note that accumulation of electrons and dielectric voltage at the anode side still increase slightly even if the applied voltage begins to decrease at the end of region C until the secondary short Townsend like discharge appears, which is described next.

4.4.3.4 Secondary short Townsend like discharge

In region D, a secondary short Townsend like discharge ($\approx\ 1-2\ \mu s$) is induced as the applied voltage rapidly decrease from ≈ 3500 down to ≈ 2400 volts within $1\ \mu s$ (the gap voltage reverses from positive to negative). The maximal current density is only $\approx 5mA/cm^2$. Because of the polarity change of the gap voltage the ions rapidly accumulate on the dielectric surface of the power electrode, which reduces the magnitude of negative surface charges accordingly, as shown in Figure 4.12a. In contrast, the electrons rapidly accumulate on the ground side, which reduces the magnitude of positive surface charges. When this short secondary Townsend like discharge occurs, the dielectric voltage decreases dramatically. In other words, this short secondary Townsend like discharge is formed due to the gap voltage reversing. The snapshots of plasma properties and source/sink terms of electron related channels are shown in Figure 4.8 where the discharge current is at the peak value. Again these data show that it is a typical

Townsend like discharge. In addition, Figure 4.8b shows that the inclusion of heavy particle related channels in the fluid modeling can reproduce quantitatively the measured discharge current as shown in Figure 4.3 in region D, in which the simple plasma chemistry fails to do so.

4.4.3.5 Phase diagram of discharge properties

To better elucidate and to have an overview of the helium DBD, we present spatial-temporal phase diagrams of several important discharge properties next. Figure 4.13, Figure 4.14 and Figure 4.15 illustrates the phase diagram of the electron density, He_2^+ density and electron temperature distribution respectively along with the vertically placed temporal simulated discharge current in the center for better visualization. As can be seen, in the long Townsend like discharge region (region A), most of the electrons are distributed close to the anode, while the He_2^+ mainly dominates in the region close to the cathode (grounded). Also the ions outnumber electrons across the gap, except in the region very close to the anode. Electron temperatures are generally very high in the order of $7-8\ eV$ close to the cathode side. In the dark current like region (region B), both the distributions of electrons and He2+ are very similar, which form a quasi-neutral zone near the center. This quasi-neutral zone moves from the anode side towards the cathode side at a slow speed of $\sim$100 m/s. At the same time, the electron temperatures are nearly zero in the most central part of the gap, except the narrow regions very close to the two dielectric surfaces. This results in the rapid disappearance of excited atomic helium (He_{ex}^{**}) (also shown in Figure 4.6a) and thus almost no fluorescence is emitted. Thus, we term this region as the dark current like region. After the dark current region, i.e., in the primary short Townsend like discharge (region C), similar to region A, the electrons move to the region close to the anode side, while the ions move to the cathode side with much higher concentration as compared to region A. Also the electron temperatures are much higher in the region close to the cathode in the range of $8-10\ eV$. In region D, the secondary short Townsend like discharge region, the electrons move to the cathode side, while the ions move to the anode side since the current is reversed as compared to that in regions A and C. The electron temperatures are also high close to the powered electrode side (left-hand). After this region, the discharge repeats the region A-D, but with opposite polarity because of the reversed applied voltage. One interesting thing to be noticed in Figure 15 is that there are two very short regions (less than $0.3\ \mu s$; in the

early stage of region C, and between regions C and D), in which the electron temperatures are nearly zero across the gap, except the regions close to the dielectrics. In these two regions, all data show that they are also typical dark current like discharges, although very short in time.

4.5 Conclusion and Brief Summary of This Chapter

In this chapter, we have investigated in detail the non-equilibrium helium dielectric barrier discharge driven by a realistic bipolar quasi-pulse power source (20 KHz) using a self-consistent one-dimensional fluid modeling code. Two sets of helium plasma chemistry which are often found in the literature were used to model the helium DBD. Simulated temporal discharged currents using the complex plasma chemistry are in excellent agreement with the measurements obtained in the present study, which validates the fluid modeling code. It also indicates that the inclusion of heavy particle related reactions (especially the Hornbeck-Molnar associative ionization) is critical in accurately predicting the helium DBD because of the slow varying electric field in the range of the tens of kilohertz. Based on the simulations, the helium DBD with $1\ mm$ in width shows several interesting mode transitions, which can be classified into long secondary Townsend like (region A), dark current like (region B), short primary Townsend like (region C), and shortsecondary Townsend like discharges (region D), based on predicted discharged properties. In addition, the externally supplied electrical power is absorbed mostly by the molecular helium under the frequency of 20 KHz, rather than by the electrons like in a RF discharge.

Chapter 5

Two-dimensional Simulation of Silane/Hydrogen Gas Discharge in a Plasma Enhanced Chemical Vapor Deposition Chamber

This chapter demonstrates a large-scale realistic PECVD using the mixture Silane/Hydrogen gas. A multiscale temporal marching scheme is employed to obtain a quasi-steady gas discharge with a steady neutral diffusion flow field in several thousands of RF cycles. The spatial plasma parameters of electron density, electron temperature and plasma potential are demonstrated in difference phase of a RF cycles. The cycle averaged prosperities of ion and neutral densities are presented. The a-Si:H deposition rate evaluated from radical species upon substrate is shown and compared with experimental results.

5.1 Background and Motivation

Hydrogenated amorphous silicon (a-Si:H) thin films are commonly produced by plasma enhanced chemical vapor deposition (PECVD) and have been the subject of many researches over the last decade. Not only being used in the fabrication of thin film solar cells, a-Si:H has also an extensive field of applications in other devices, such as thin film transistors used in liquid crystal displays, light emitting diodes, etc. In the recent decade, numerical studies on SiH_4 plasma usually focused on the details of the chemistry occurring during deposition and especially of the nano-particles formation. Most of the recent studies focused on the zero-dimensional chemical kinetic study or 1-D fluid modeling study with complex chemistry considered. To understand the deposition uniformity on a substrate, a 2-D fluid modeling of the PECVD is necessary. In this chapter, we demonstrate a 2-D silane/hydrogen fluid modeling with complex chemistry and validate the inferred deposition date with experiment results.

5.2 Silane/Hydrogen Plasma Chemistry

In the simulation, we hav employed a set of silane/hydrogen plasma chemistry, which consists of 15 species and 28 reaction channels [Nienhuis, 1998], which is summarized in Table 5.1. This set of plasma chemistry include: electron inpact dissociative ionization (1) (2), electron im-

pact vibrational excitation (3) (4) (10) (11) (12), electron impact dissociation (5) (6) (7) (13), electron attachment (8), electron impact ionization (9), and we consider the species Si_nH_m containing up to 4 silicon atoms. Note that the vibrational excited state species ($SiH_4^{(1\sim3)}$, $SiH_4^{(2\sim4)}$, and $H_2^{v\neq0}$) in this study are assumed to be back to ground state immediately and are not solved in the fluid modeling.

5.3 Simulation Conditions

Figure 5.1 shows the schematic diagram of the PECVD chamber. Simulation conditions include: (1) chamber pressure ($600\ mtorr$); (2) a square glass plate ($20 \times 20\ cm$); (3) substrate temperature (250^oC); (4) gap distance between shower-head and substrate ($10\ mm$) and (5) inflow rate ratio of silane to hydrogen ($80 : 50\ sccm$). A multi-scale temporal simulation algorithm is proposed to speed up the simulation caused the wide range of time scales present in the discharge, which include those of electron ($10^{-10}\ s$), positive and negative ions ($10^{-7}\ s$) and neutral radicals ($10^{-4}\ s$). In addition, a neutral Navier-Stokes solver with automatic slip boundary conditions was used to obtain the background gas distributions including the number density, temperature and mass-averaged velocities. These properties were then used in the plasma fluid modeling as the background gas properties. Note the flow solver, which is a pressure-based, SIMPLE-like, all-speed code, was developed by another group member [Hu, 2010].

5.4 Multiscale Temporal Marching Scheme

To ease the computational cost caused by the large disparity of the time scales for electrons, ions and neutral species, we have designed a multiscale temporal marching scheme, which is sketched in Figure 5.2. In this special temporal marching scheme, we only implicitly solve the electron continuity equation, electron energy density equation and the Poisson's equation together at each electron time step to obtain the instantaneous electric field and electron temperature. The electron time step usually decide by the minimum value of reciprocal plasma frequency or plasma relaxation time. Take the advantage of ion's larger characteristics time than electron, we solve ions fluid equations after electrons march some number of steps, usually is 10 in this study. In the small electron time step, the force induced by the variation of

electric field is generally small for ions since ions have larger inertia than electrons. Thus, we only record the data of the last electron time step and obtain the instantaneous transport coefficients of ions using the latest electric field. At the same time, neutral species and ion densities are solved implicitly with much larger neutral time step size (10,000 electron time step size). By using this strategy, a quasi-steady gas discharge with a steady neutral diffusion flow field can be obtained after several thousands of RF cycles.

5.5 Results and Discussion

Figure 5.3 shows the initial background density of H_2 and SiH_4, gas temperature, and flow velocity. Results show that the temperature distribution across the electrode gap is almost linear, which means that it is conduction dominated. This is reasonable since the chamber is under low-pressure condition (600 mtorr), which leads to low Reynolds number gas flows. In this case, the Reynolds number is only 0.035 with inflow velocity of silane/hydrogen and gap distance as the characteristic velocity and length, respectively. In addition, the density near the substrate surface decreases greatly because of the heated substrate at elevated temperature (250^oC). Non-uniform background density is important in determining the ionization rate during the simulation.

Figure 5.4 shows the plasma potential at difference phase (a) $\phi = 0$ (b) $\phi = 0.5\pi$, $\phi = 1.5\pi$ and (d) $\phi = 2\pi$. Results show that in most of the region between the electrodes the potential distribution is similar to a quasi-1D case. Electric field is found to be very strong near the edge of guard ring close to the ground electrode (e.g., $x = 13\ cm$ and $y = 1\ cm$), although the corners of the guard rings were rounded.

Figure 5.5 show that the time-average potential distribution across the electrode gap at the center of the chamber, in which the plasma potential is 48.82 V. There is a 20 V averaged potential drop $y = 0\ 0.7\ cm$ due to the negative net charges accumulated on the glass surface, which provides protections from ion bombarding at the substrate surface.

Figure 5.6 and Figure 5.7 shows the electron and related electron temperature at difference phases respectively, which also shows high peak value close to the corner, where the strong electric field is induced. Apart from the corner of guard ring close to power electrode where plasma

properties are strongly related to edge electric field, electron density and electron temperature show the homogeneity between the electrodes. It's the benefit that a large scale PECVD can simplify the two or three dimensional effects into a pure one dimensional behavior. Thus, homogeneous distribution of species densities above substrate glass are observed which help the uniformity of deposition. However, the non-uniformity of large scale PECVD with very high frequency (VHF) power source (i.e. microwave) are limited due to standing waves generated on the electrode surfaces [Schade et al., 2006], which needs further study in the future. Figure 5.8 shows the ion species densities include positive ions (a) H_2^+ (b) SiH_2^+ (c) $Si_2H_4^+$ and negative ion (d) SiH_3^-. The dominated positive ion is SiH_2^+, and negative charged species is SiH_3^-. Figure 5.9 show that the time-average charged densities distribution across the electrode gap at the center of the chamber. It shows that a quasi-neutral region is form in the center part of the gap with positive charge density in the sheath close to the electrodes. The bulk dominated by SiH_2^+ and SiH_3^- at $y = 0.85\ cm$, while electron density shows pick value of $5.2 \times 10^{14} m^{-3}$ at $y = 0.64\ cm$. $Si_2H_4^+$ species density is three order smaller than the density of SiH_2^+.

Figure 5.10 shows a series of time-average spatial distribution of several important radical species related to the a-Si deposition in the PECVD chamber. These include: (a) H (b) SiH_2 and (c) $SiH3$. Note their concentrations are almost stationary and do not move with the oscillating field because they are neutral species. It is clear that SiH_3 is the most dominant radical species include silicon atom, which is important in film deposition, as found in earlier simulations and experiments [Bleecker et al., 2004a]. The predicted uniform radical density distribution above the substrate glass can lead to a uniform a-Si deposition rate over the glass, which will be shown later. Figure 5.9 show that the time-average radical densities distribution across the electrode gap at the center of the chamber. H and SiH_3 radical have peak value at $y = 0.85\ cm$ of $2.9 \times 10^{18} m^{-3}$ and $2.02 \times 10^{18} m^{-3}$ respectively, while SiH_2^+ has $8.7 \times 10^{15} m^{-3}$ at $y = 0.64\ cm$.

Figure 5.12 present the comparison of deposition rate from numerical simulation and experimental data as well as SiH_3 radical species flux to the glass. The numerical deposition rate is estimated by combining the simulated SiH_3 density and the deposition rate coefficient [Lin,

2010],

$$SiH_{3(g)} + db \rightarrow SiH_{3(a)} \tag{5.1}$$

with its reaction rate coefficient

$$k_{gas} = 6.39 \times 10^{-7} T_g^{-1.2} exp(\frac{-159.62}{T_g}) \tag{5.2}$$

where the gas temperature is assumed $500\ K$. The surface rate coefficient can be expressed as

$$k_{surface} = \frac{k_{gas}}{A_s} \tag{5.3}$$

where A_s is the area of the gas on the site which is assumed as $10^{15} cm^2$, and θ is the fraction of available surface sites. The numerical deposition rate can obtain by

$$\frac{d[X]_{surface}}{dt} = k_{surface}[X]_g \tag{5.4}$$

While the fraction θ is assumed as 0.015 in order to coincide the experimental result. In conclusion, both numerical and experimental results qualitatively and quantitatively show the uniform deposition rate on the glass with the choosing of relevant number fraction θ.

Figure 5.12 shows that, with the present simulation data, the calculated deposition rate agrees very well with the experimental data under the same test conditions [provided by Prof. Tsai at NCTU], if the fraction θ is assumed as 0.015. In addition, the deposition rates of both the simulation and experiment at the edge increase slightly probably due to the enhanced electric field as shown in Figure 5.4.

5.6 Brief Summary of This Chapter

In this chapter, we have demonstrated a 2D-axisymmetric chamber-scale simulation of a realistic silane/hydrogen PECVD chamber using the developed parallel fluid modeling based on a set of fairly complicated plasma chemistry. Major finding of this chapter can be summarized as follows:

1. In most of the region between the electrodes, the plasma can be approximated by a quasi-1D discharge, in which a quasi-neutral region in the center is formed with sheaths near the electrodes.

2. SiH_3 is the most dominant radical species include silicon atom predicted in the simulation, which coincides with previous findings using simulations and experiments.

3. Calculated deposition rate on the substrate agree very well with the measured value if the fraction of available reaction site is set to 0.015.

4. Slightly increased deposition rate at the edge of the substrate was found due to the enhanced electric field in this region, which also have been observed in the experiments.

Chapter 6

Conclusion and Recommendations for Future Study

6.1 Summaries of the Thesis

In this thesis, development of parallelized 1D/1D-axisymmetric and 2D/2D-axisymmetric fluid modeling codes using fully implicit finite-difference method with hybrid analytical-numerical Jacobian evaluation for low-temperature, non-equilibrium plasma simulation has been reported. Implementation and validations against earlier simulations and experimental data are described in detail. Applications with wide range of pressures and frequencies (radio frequency in mega Hertz and alternating current in kilo Hertz) are demonstrated, compared with experimental data wherever possible, and related plasma physics and chemistry are discussed therein. Validated codes are the applied to simulate one-dimensional helium dielectric barrier discharge driven by realistic distorted sinusoidal voltages and two-dimensional silane/hydrogen gas discharge in an PECVD chamber. Major findings of the thesis can be summarized as follows:

1. Parallelized 1D and 2D fluid modeling code using finite-difference method was developed and validated against experiments and previous simulations. (Chapter 3)

2. Parallel speedup was demonstrated to be super-linear for the number of processors up to 144 using a GEC chamber-scale simulation with 120,048 degrees of freedom with a suitable combination of preconditioning and matrix solvers. (Chapter 3)

3. Major Towsend-like behavior along with complicated mode transitions were found for a helium dielectric barrier discharge driven by a 20 KHz distorted sinusoidal power source under atmospheric-pressure condition. (Chapter 4)

4. In the silane/hydrogen gas discharge in a low-pressure PECVD chamber driven by a RF power source (27.12 MHz), SiH3 was found to be the most dominant radical species with silicon atom, which leads to the deposition of silicon film on the substrate. Relatively uniform film deposition rate was found across the substrate, except slightly increased value near the edge. (Chapter 5)

6.2 Recommendations for Future Work

Base on the viewpoint for improving the fluid modeling code, there are several possible directions of research are recommended for further studies and are summarized as follows:

1. To apply the fluid modeling code for simulating several challenging gas discharge problems in the frequency range of RF and AC.

2. To further reduce the computational time in larges-scale low-pressure (or diffusion dominated) fluid modeling problem that may involve large number of ion and neutral species, we may adopt the following multiscale temporal marching scheme:

   (a) Solve the electron continuity equation, electron energy density equation and Poisson's equation together with fully implicit scheme with an electron time step and repeat until an ion time step size ($\sim$10-50 electron time steps) is reached.

   (b) Solve the (linearized) continuity equations for all ion species implicitly one by one using the most updated (or mean) electric field for evaluating the transport coefficients of ions.

   (c) Repeat Step **a** and Step **b** until a neutral time step size ($\sim$10,000-100,000 electron time steps) is reached.

   (d) Solve the (linearized) continuity for all neutral species implicitly one by one using the most updated (or mean) electric field for evaluating the transport coefficients of ions.

   (e) Repeat Steps **a** through **d** until the preset steady-state condition is reached.

   In Step **b**, the steady-state continuity equation for each neutral species may be solved at each time step to further reduce the computational cost to reach steady-state flow condition.

3. For treating gas discharges at higher pressure, in which the convection by the neutral flow is important, the Navier-Stokes equation needs to be solved at each neutral time step in the above after Step **d**.

4. For treating gas discharged with complex geometry, the fluid modeling equations need to be solved in the curvilinear coordinate frame.

5. To develop a Maxwell equation solver for solving discharge involving EM waves such as high-frequency and large-area PECVD and inductively coupled plasma (ICP) problems.

6. To incorporate an automatic DC-bias adjustment function into the fluid modeling code.

7. To couple an external circuit module with the fluid modeling code.

8. To extend the fluid modeling code into a three-dimensional version and couple with a time-dependent Maxwell equation solver (e.g., time-dependent finite-difference, TDFD) for several realistic PECVD cases, such as solar cell film deposition.

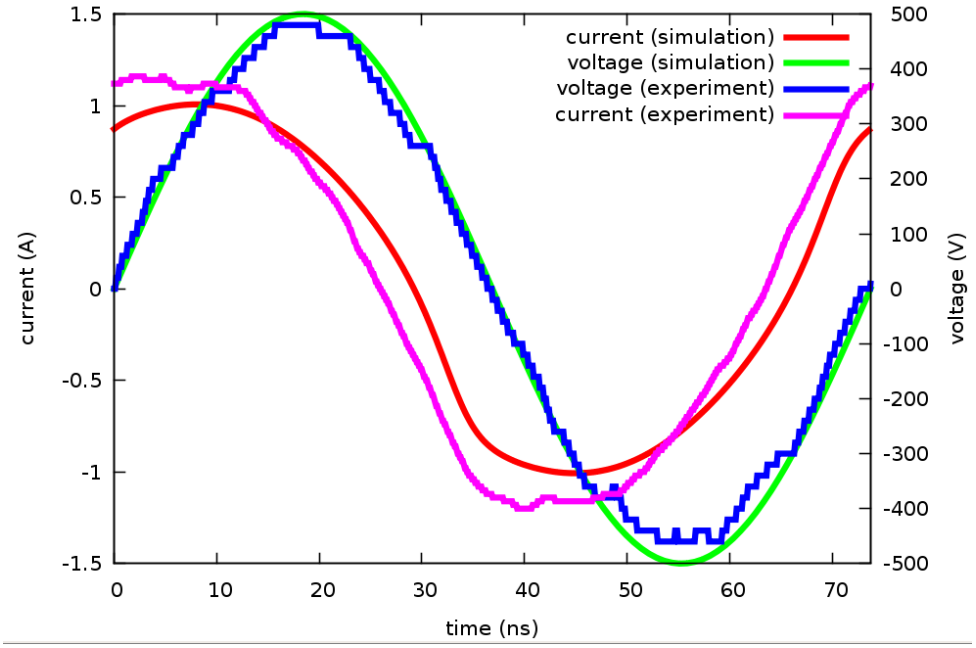

Figure 3.1: Comparison of simulated and experimental voltages and currents for atmospheric-pressure discharge with $1\ mm$ gap spacing using sinusoidal $13.56\ MHz$ power source.

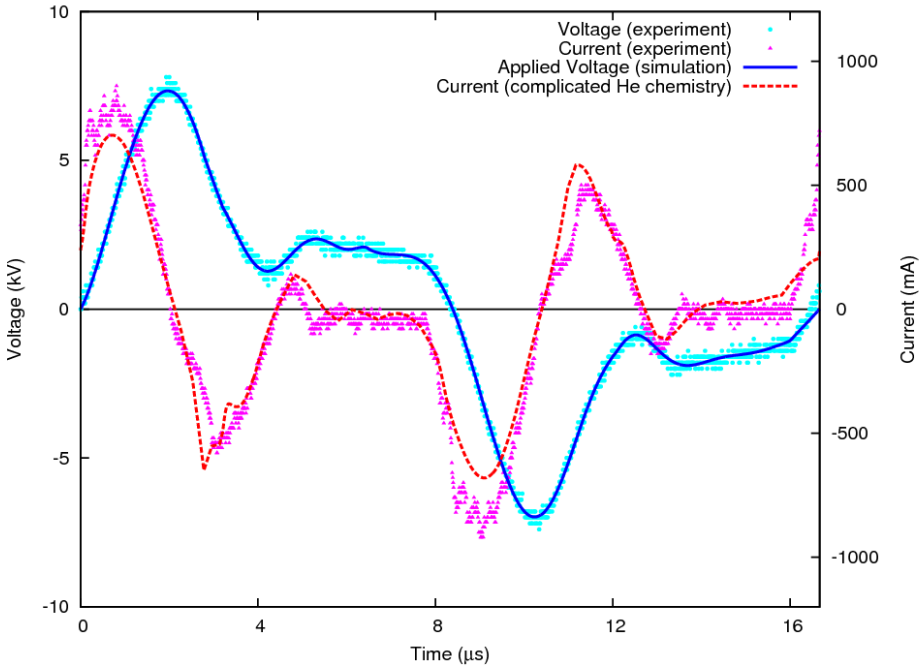

Figure 3.2: Current-voltage characteristic of numerical results and experimental data, using helium gas dielectric barrier discharge at 760 torr, applied wave frequency 60 KHz.

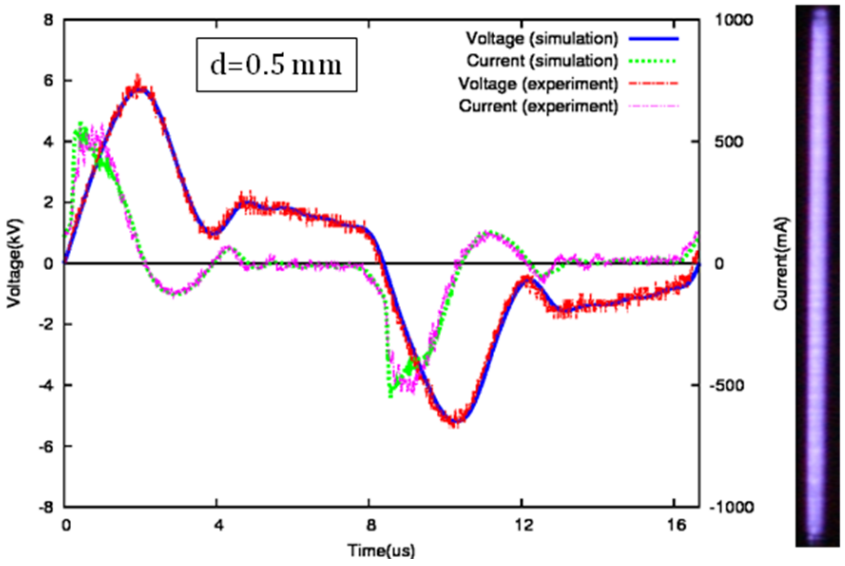

(a)

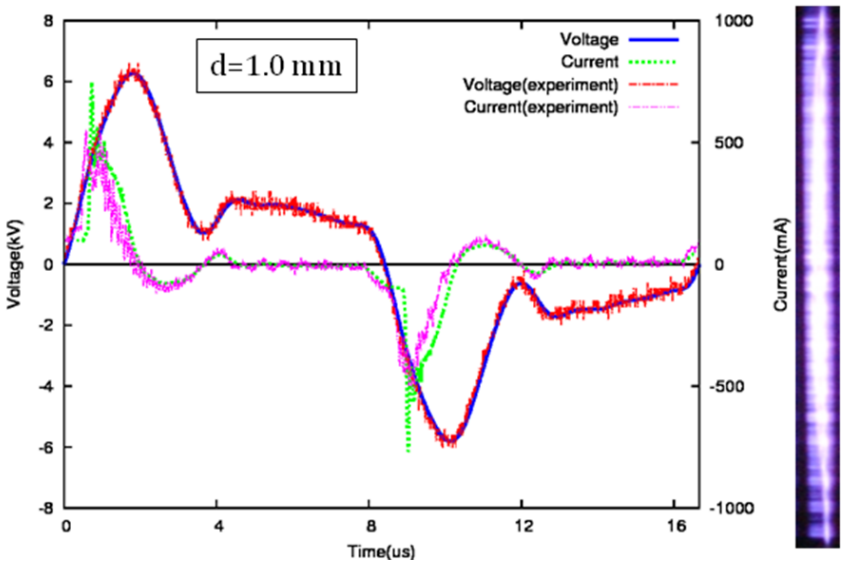

(b)

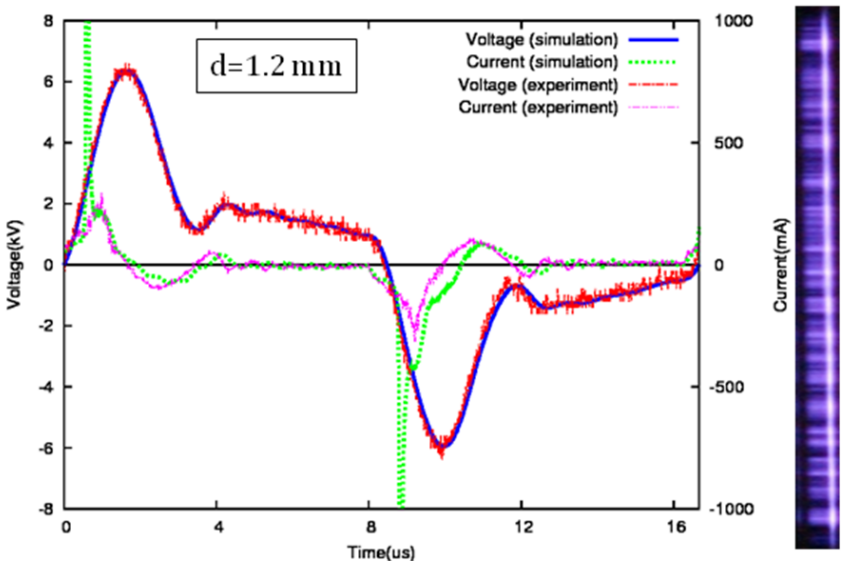

(c)

Figure 3.3: Comparison of simulated and measured discharged currents along with photo images of discharge at the right.

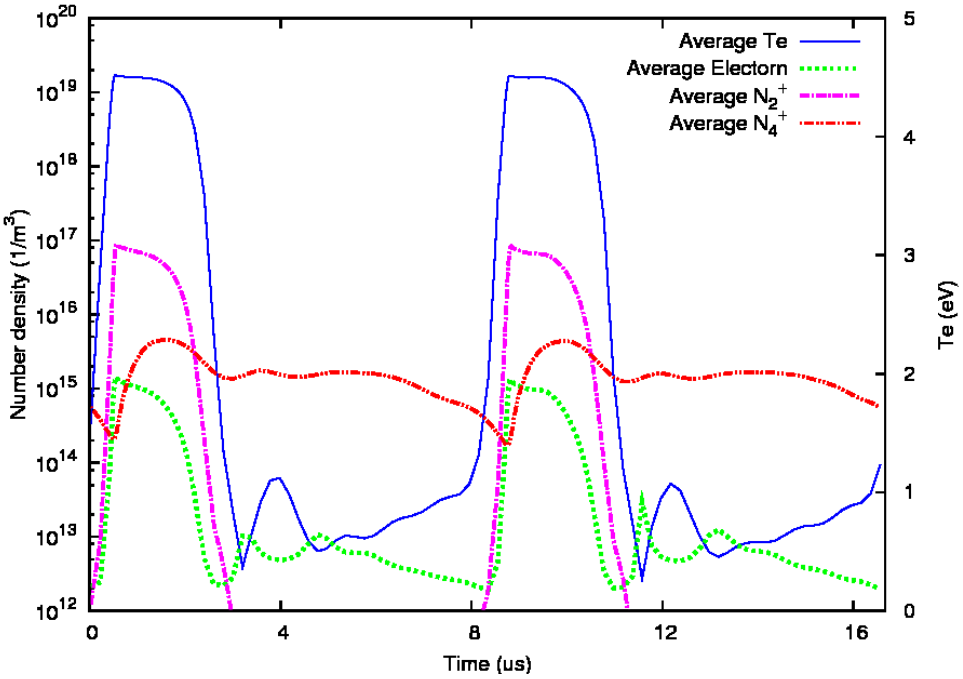

Figure 3.4: Spatial-average temporal discharge properties of nitrogen DBD ($60\ kHz$, $d = 0.7\ mm$).

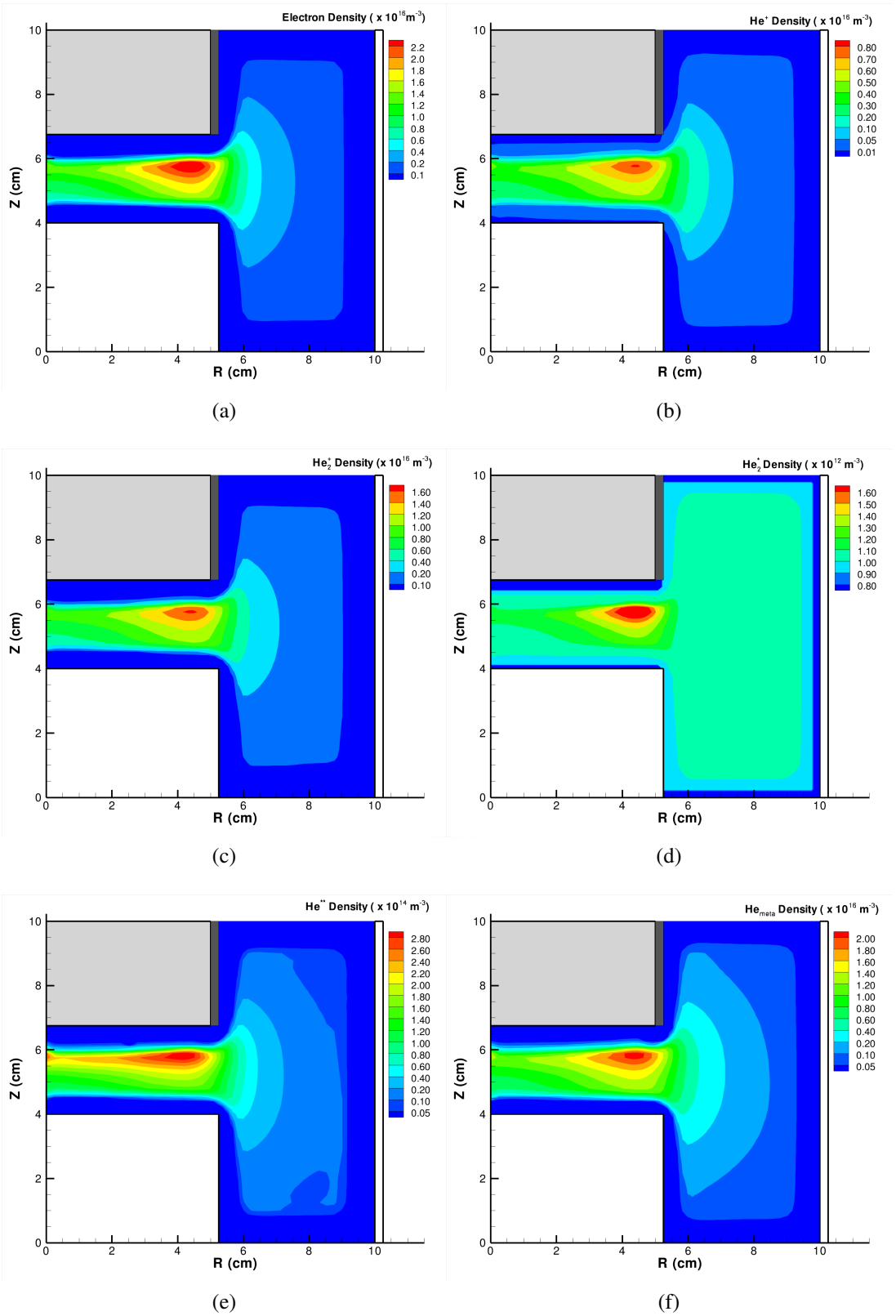

Figure 3.5: Simulated cycle averaged plasma properties of helium GEC including (a) electron, (b) He^+, (c) He_2^+, (d) He_2^*, (e) He^*, and (f) He_{meta}.

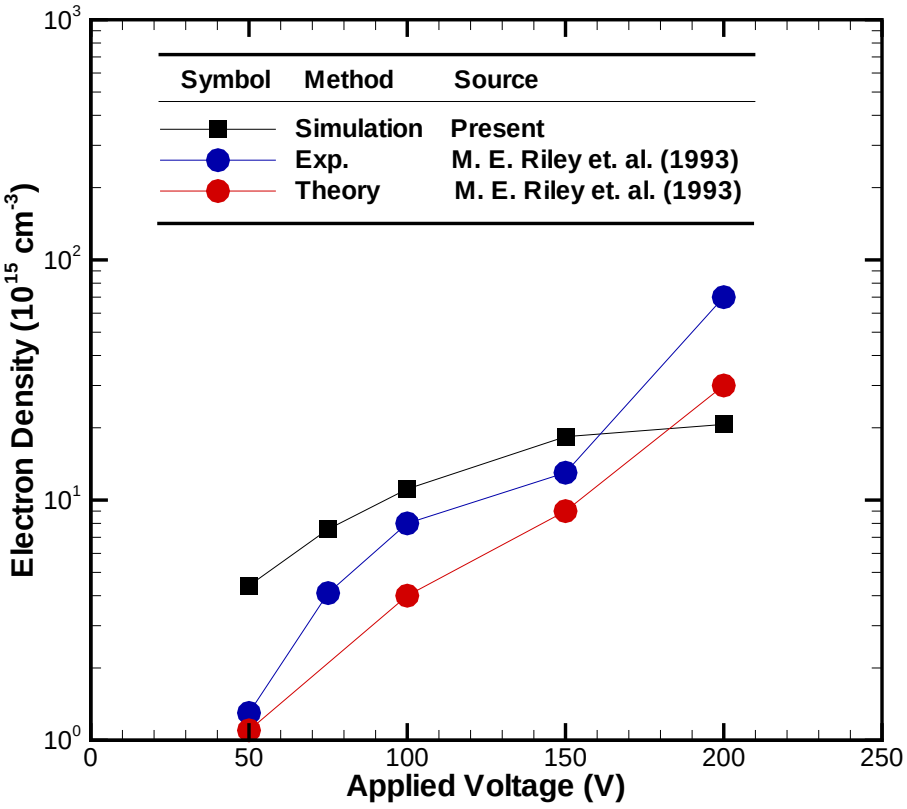

Figure 3.6: A comparison of the simulated peak electron densities with the theoretical prediction and the experimental data [Riley et al., 1994] for various applied voltages

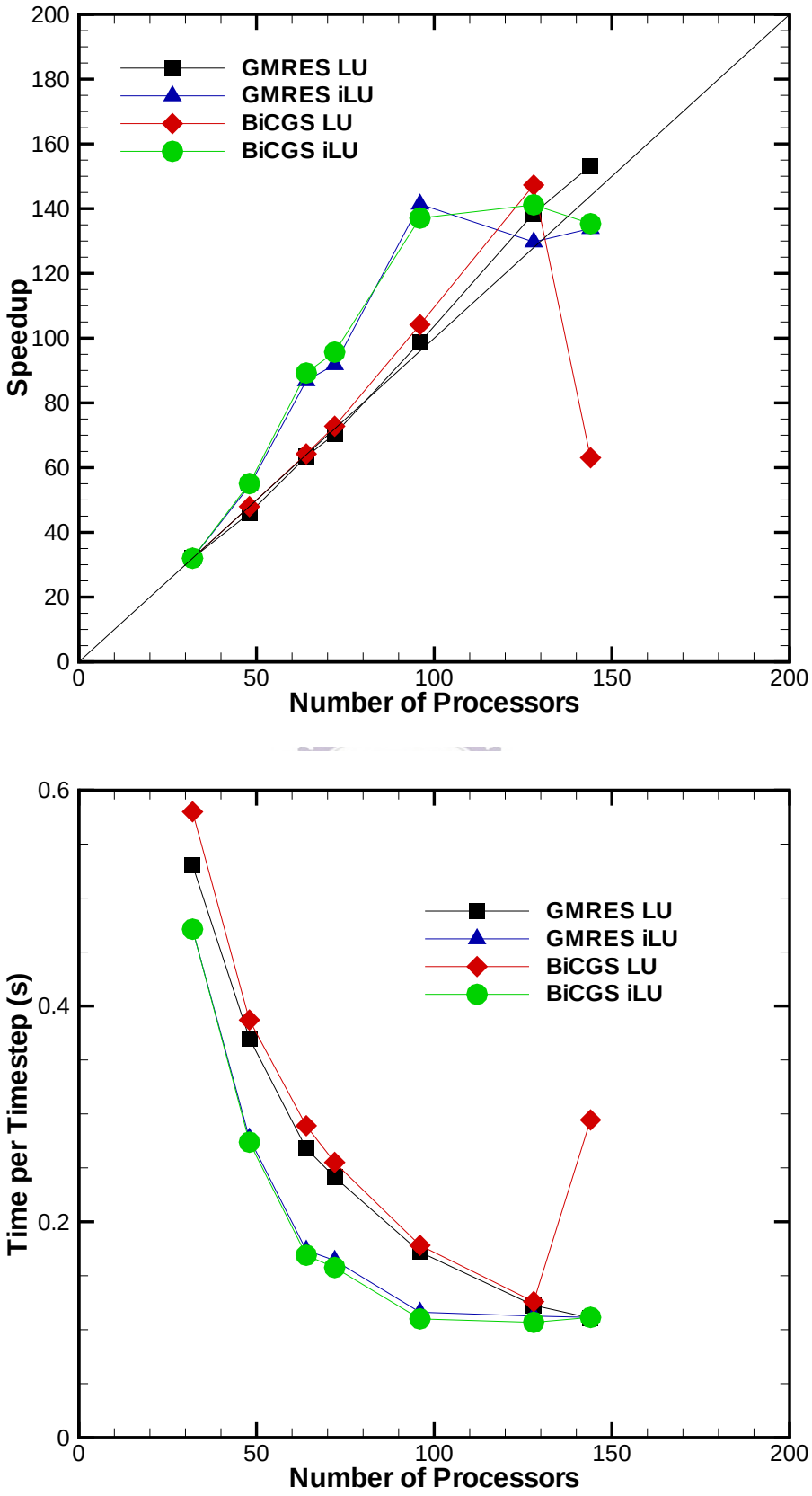

Figure 3.7: The parallel performance including (a) speedup analysis and (b) runtime per time step as a function of the number of processors

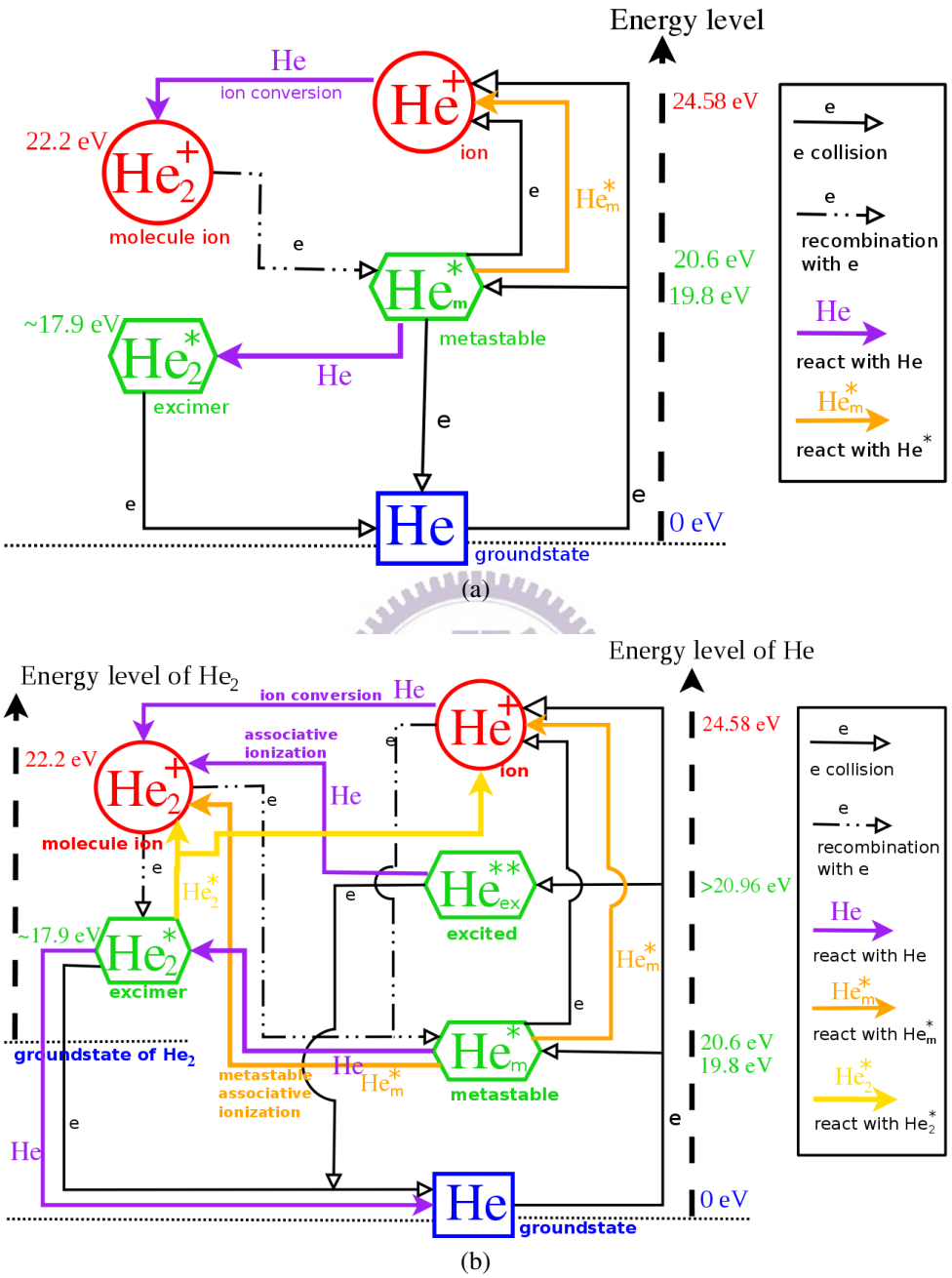

Figure 4.1: Schematic diagram of (a) simple and (b) complicated helium plasma chemistry based on the magnitude of energy level.

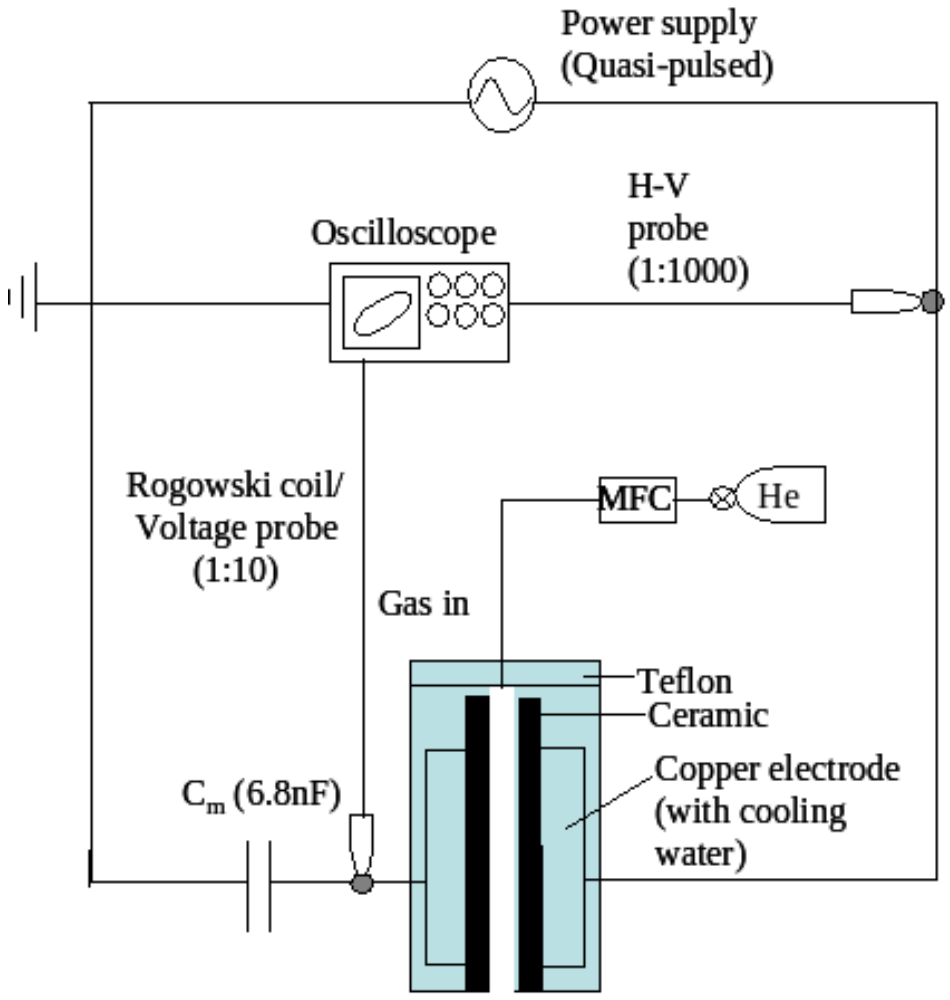

Figure 4.2: Schematic diagram of (a) simple and (b) complicated helium plasma chemistry based on the magnitude of energy level.

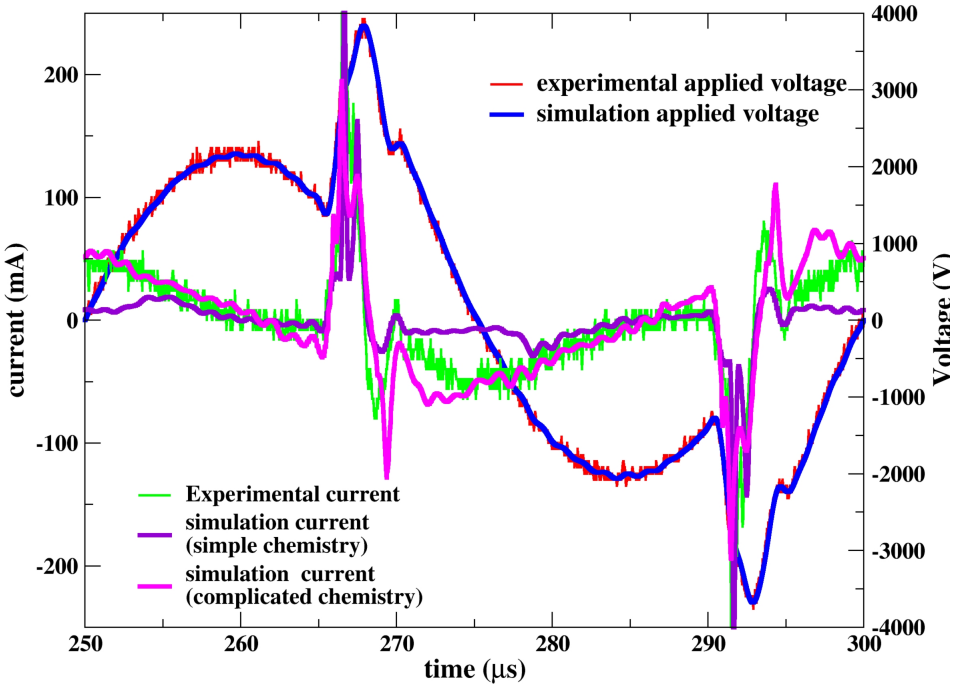

Figure 4.3: Comparison of simulated and measured discharge currents in a quasi-pulse AC cycle (20 kHz).

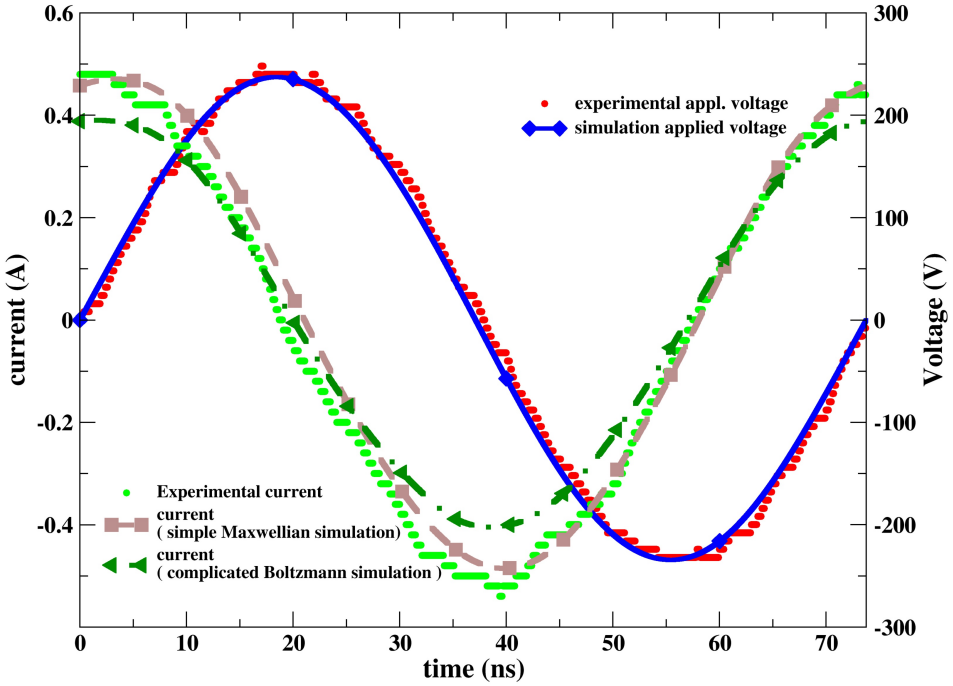

(a)

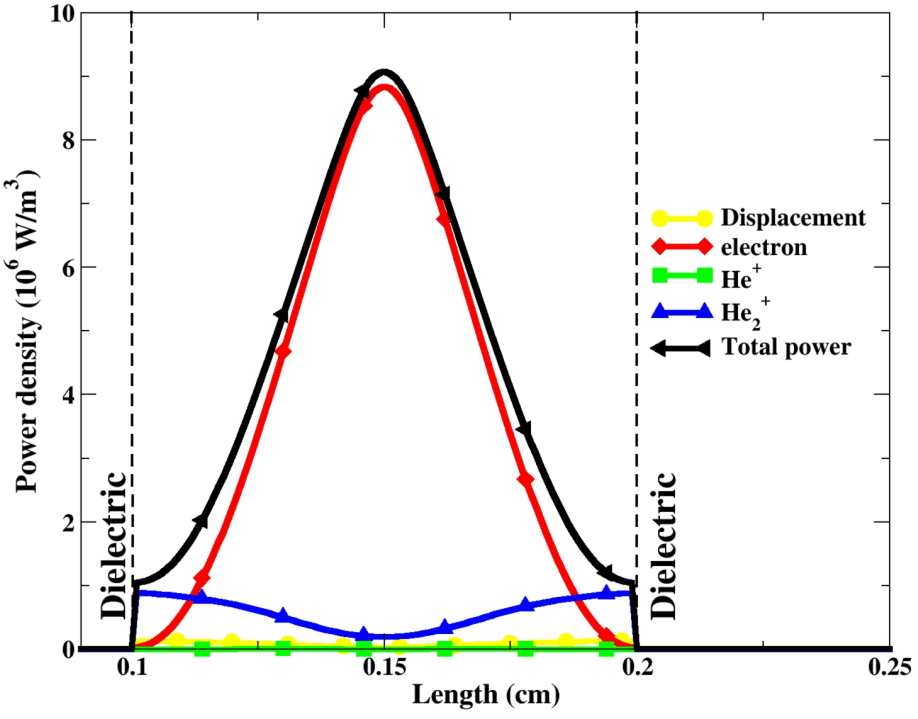

(b)

Figure 4.4: (a) Comparison between experimental current and simulation using the simple plasma chemistry. (b) Power absorption by various mechanisms.

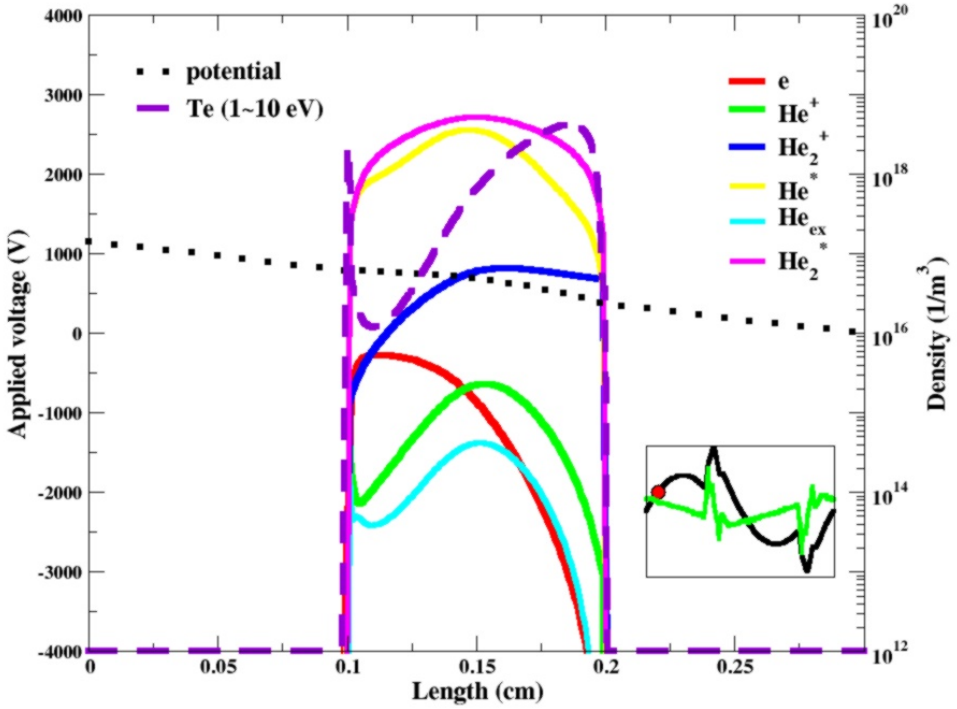

(a)

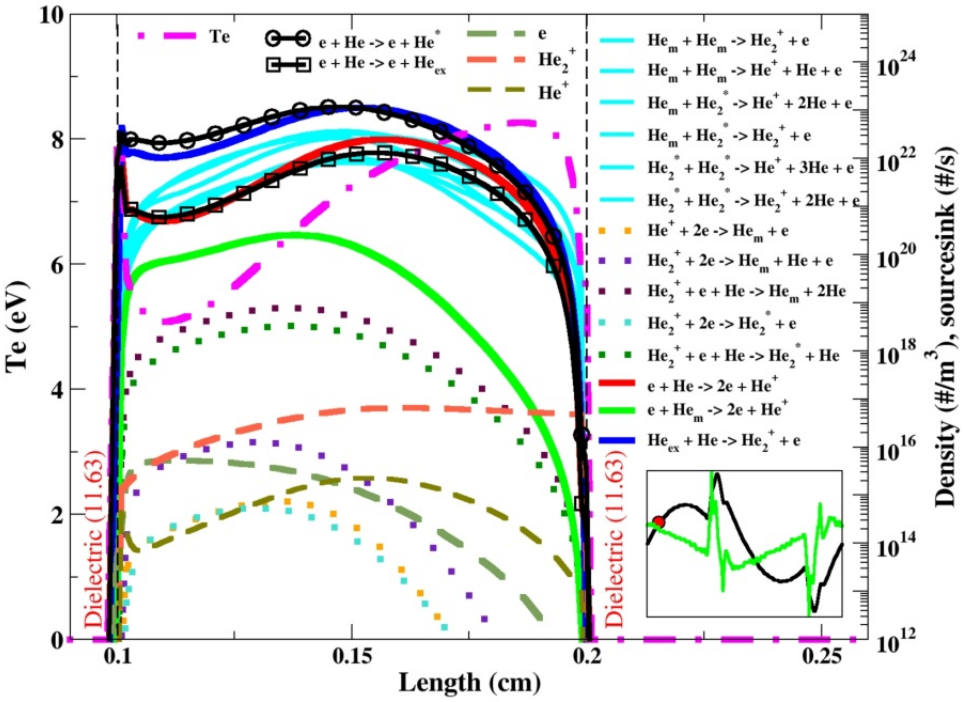

(b)

Figure 4.5: Snapshots of distribution of (a) plasma properties and (b) rate of generation of species in several reaction channels in region A (Long Townsend like) of a helium DBD driven by a quasi-pulse power source (20 kHz).

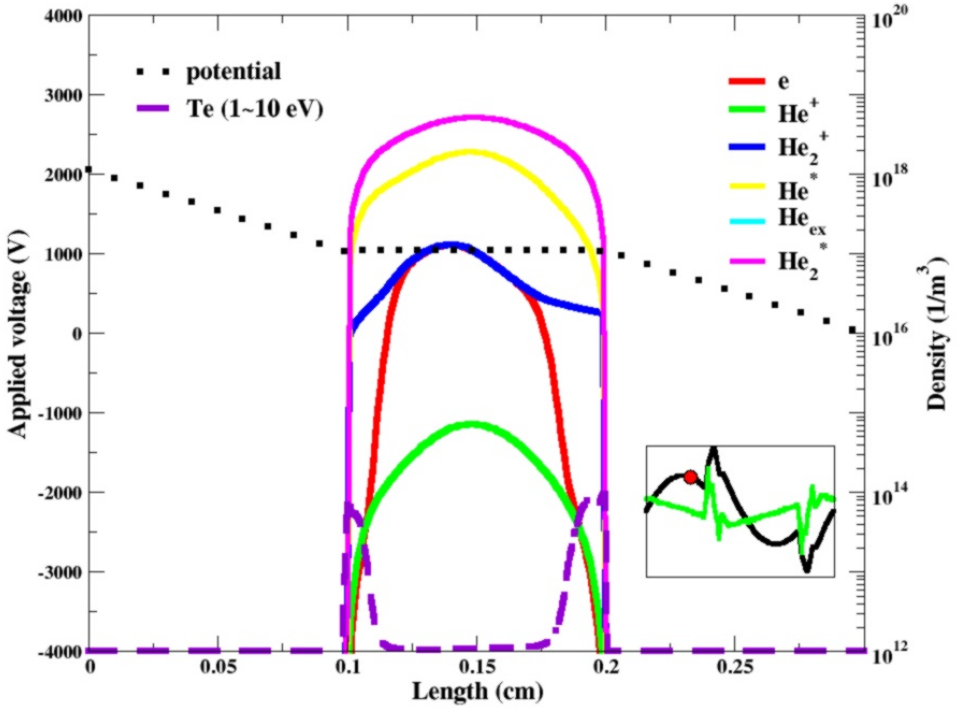

(a)

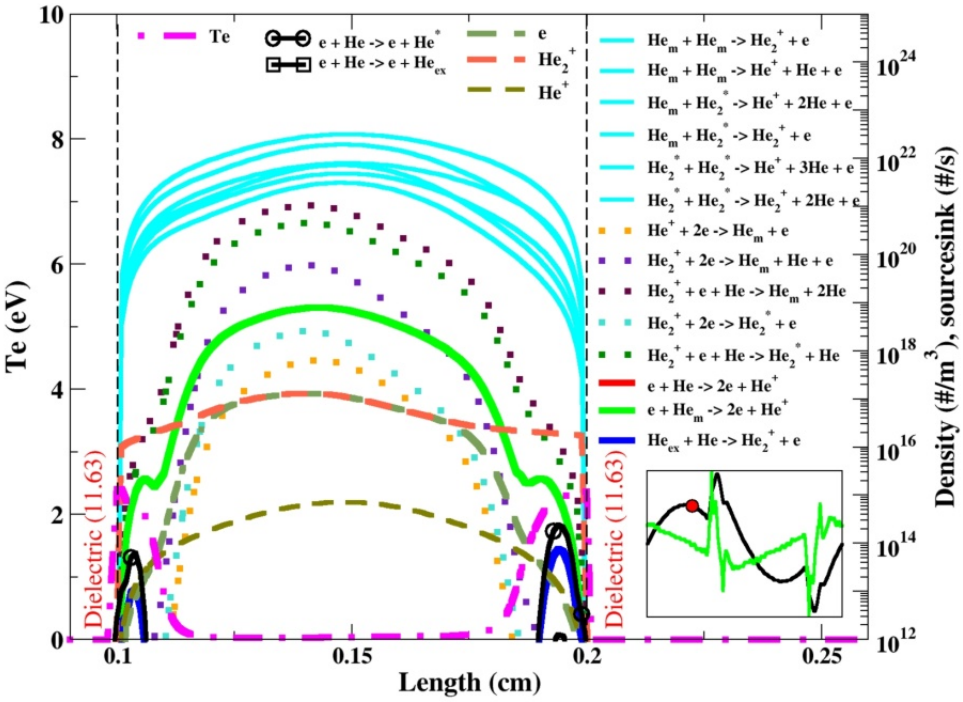

(b)

Figure 4.6: Snapshots of distribution of (a) plasma properties and (b) rate of generation of species in several reaction channels in region B (Dark current like) of helium DBD driven by a quasi-pulse power source (20 kHz)

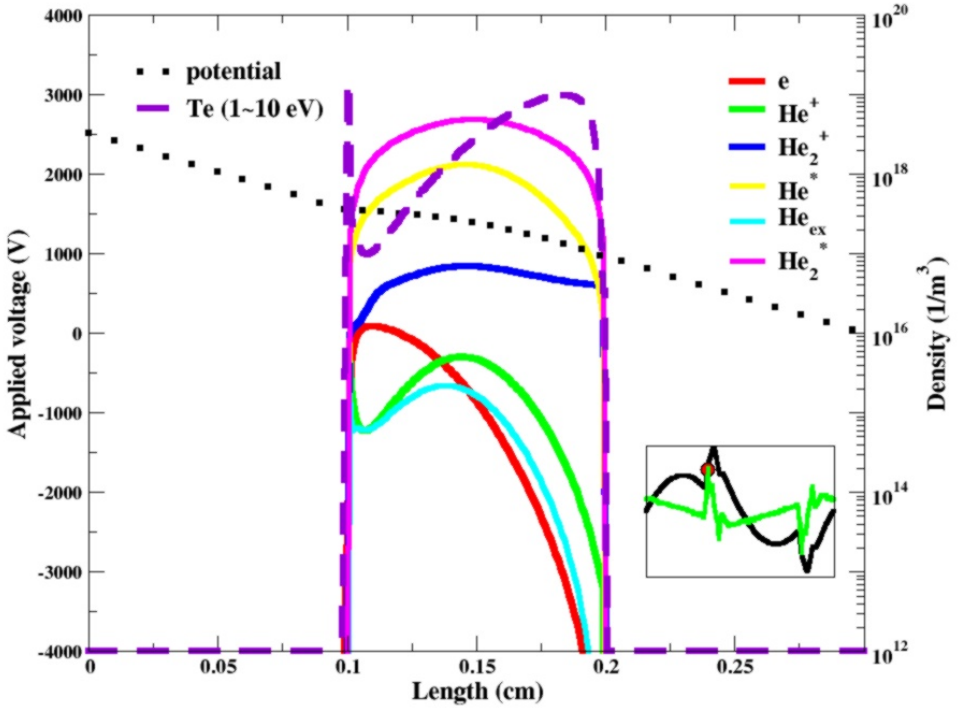

(a)

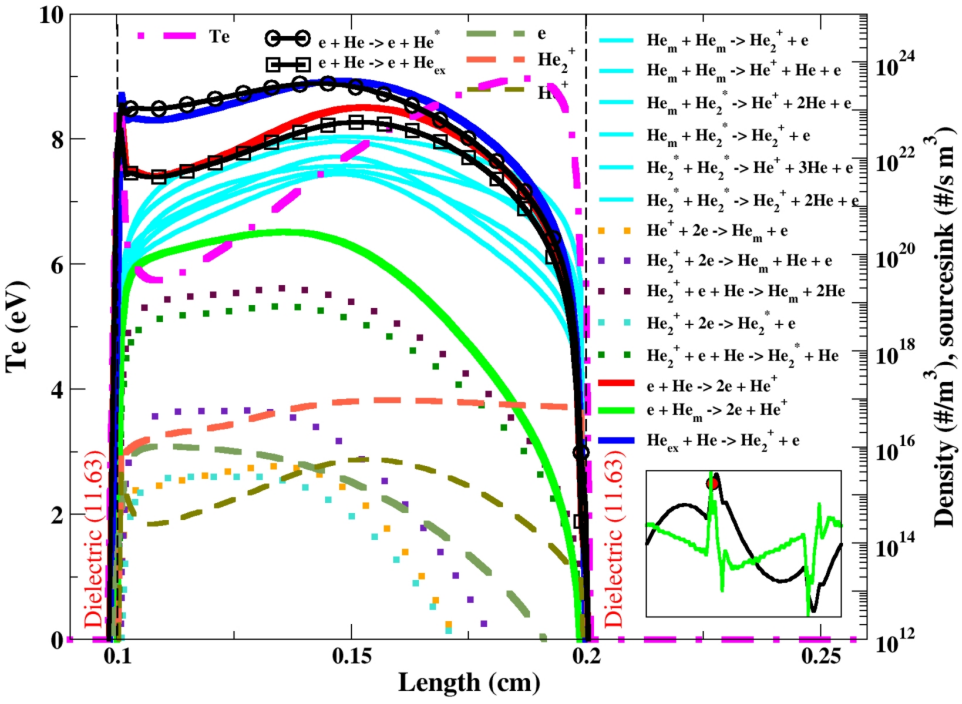

(b)

Figure 4.7: Snapshots of distribution of (a) plasma properties and (b) rate of generation of species in several reaction channels in region C (Primary short Townsend like) of a helium DBD driven by a quasi-pulse power source (20 kHz).

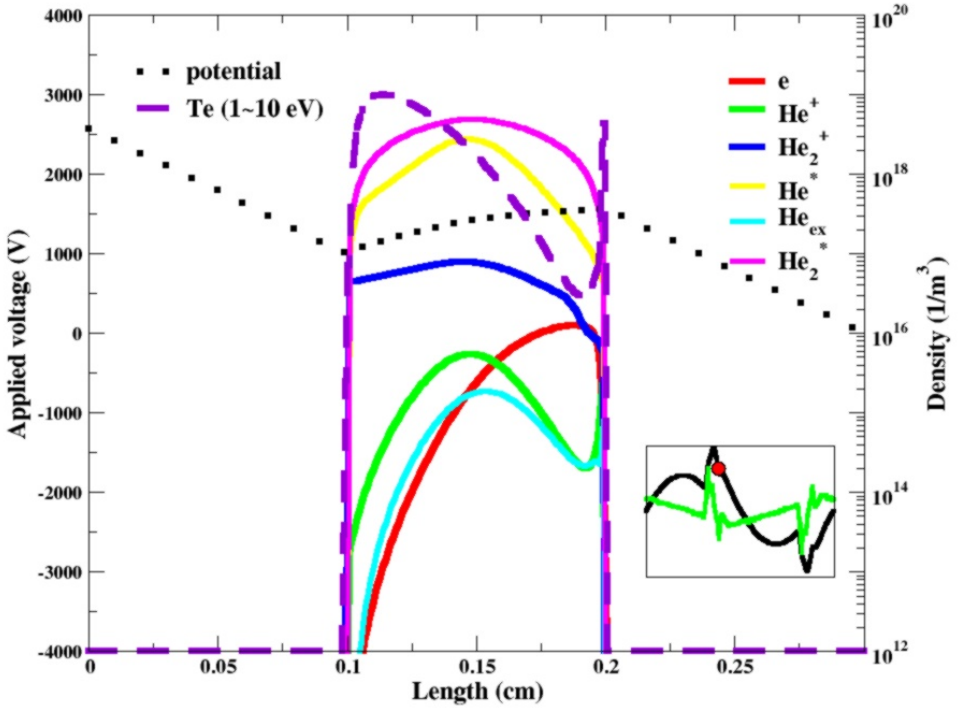

(a)

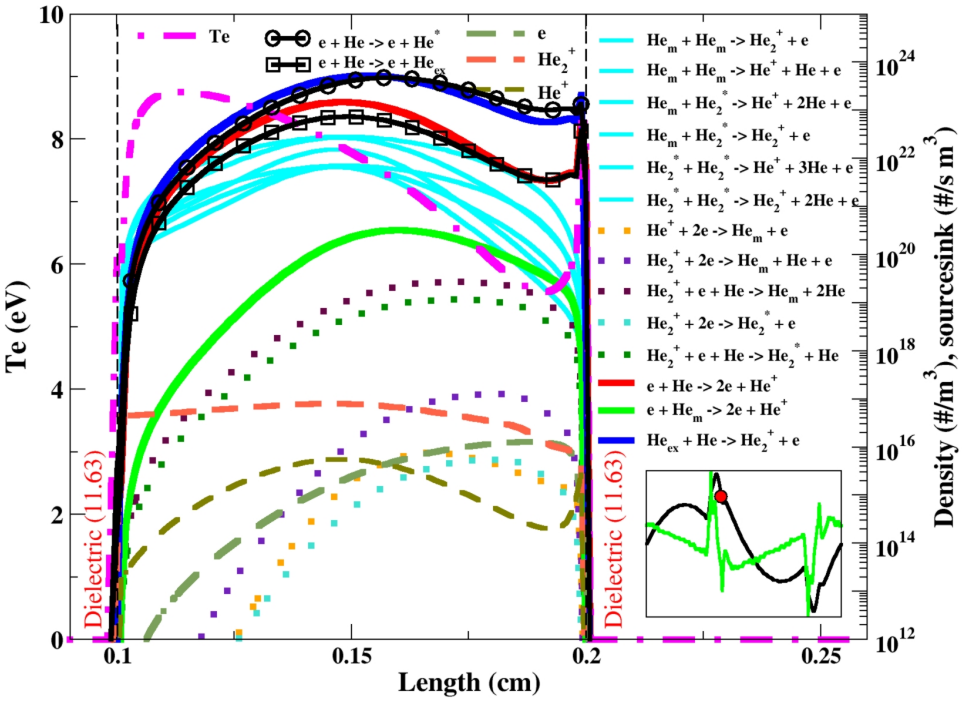

(b)

Figure 4.8: Snapshots of distribution of (a) plasma properties and (b) rate of generation of species in several reaction channels in region D (Secondary short Townsend like discharge) of a helium DBD driven by a quasi-pulse power source (20 kHz)

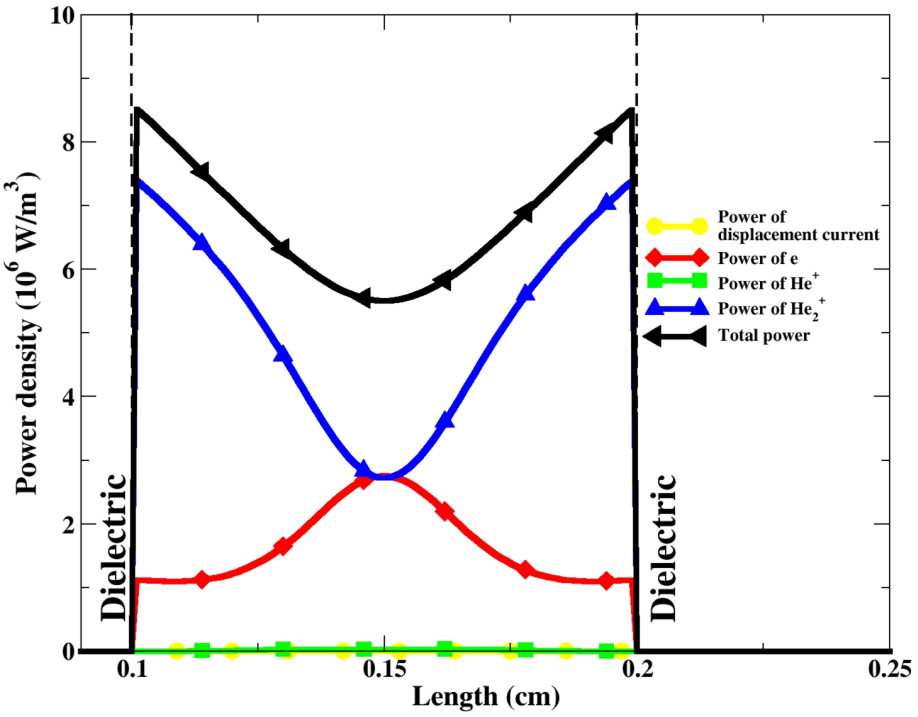

Figure 4.9: Time-average spatial power absorption by various mechanisms.

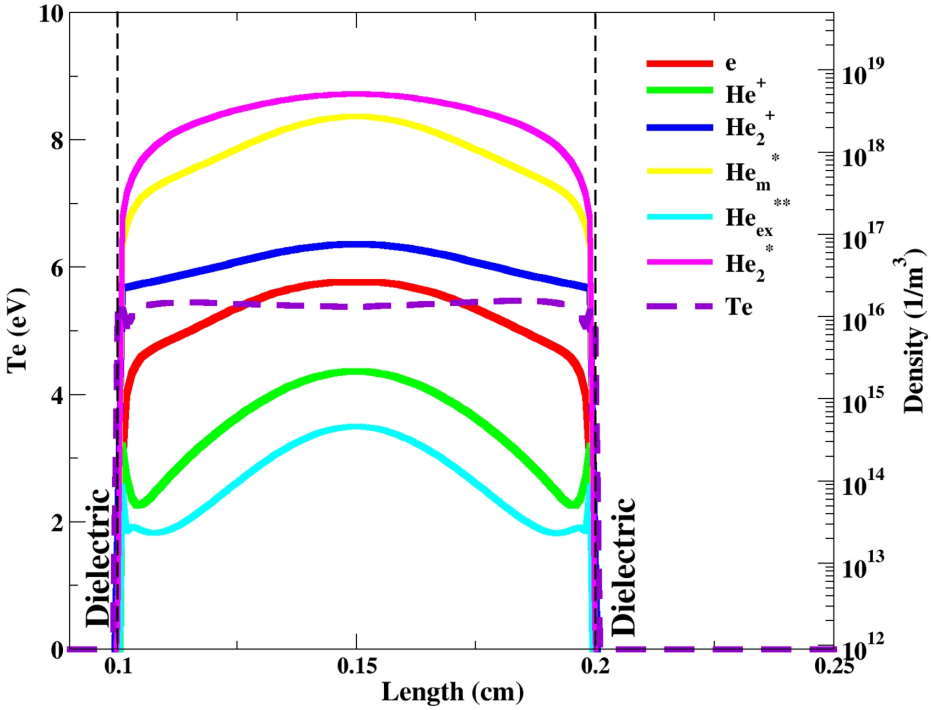

Figure 4.10: Spatial profiles of cycle-averaged discharge parameters

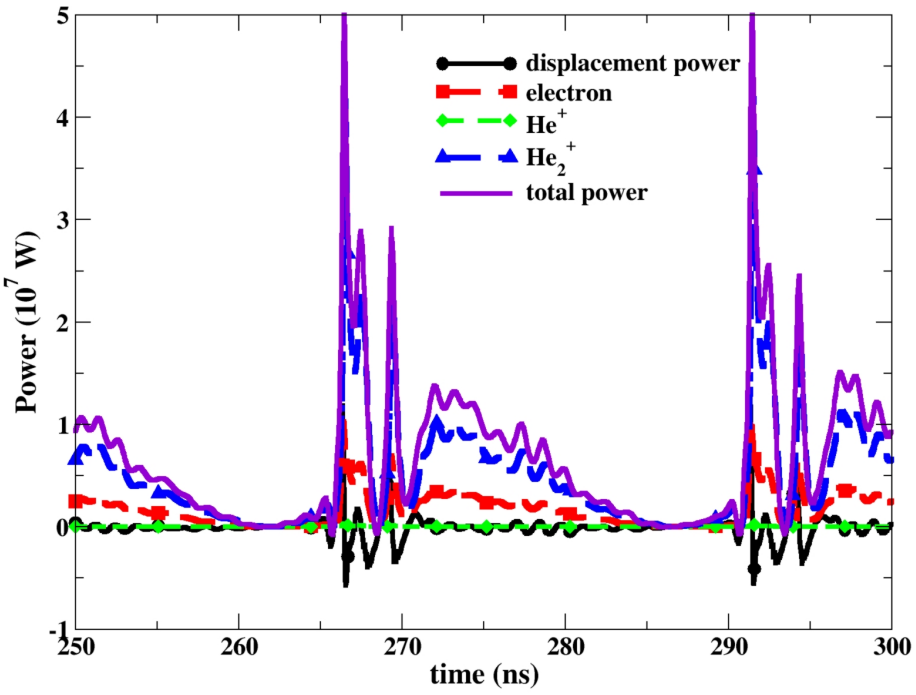

Figure 4.11: Spatial-average temporal power absorption by various mechanisms.

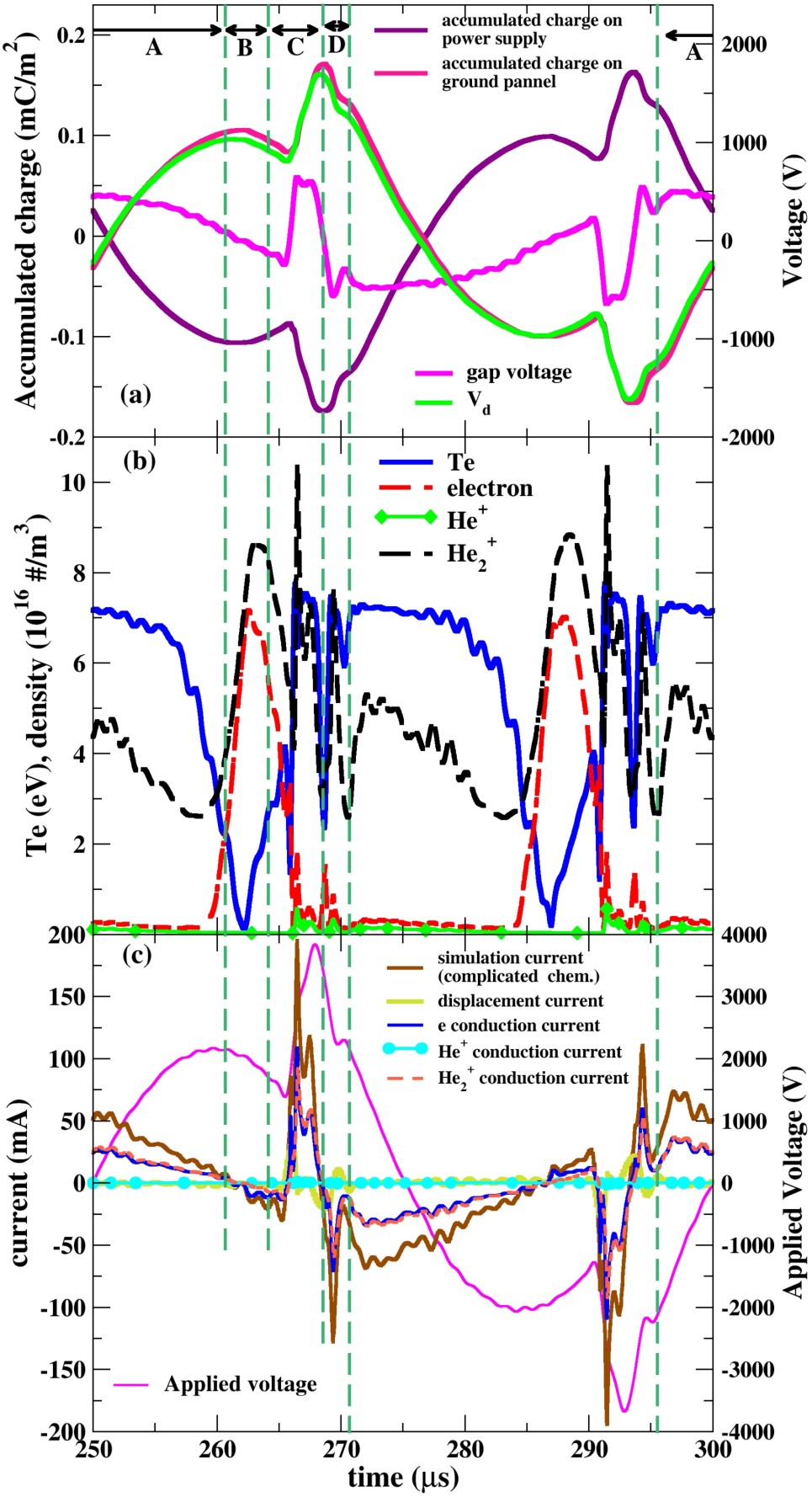

Figure 4.12: Temporal variation of spatial-average plasma properties (20 kHz).

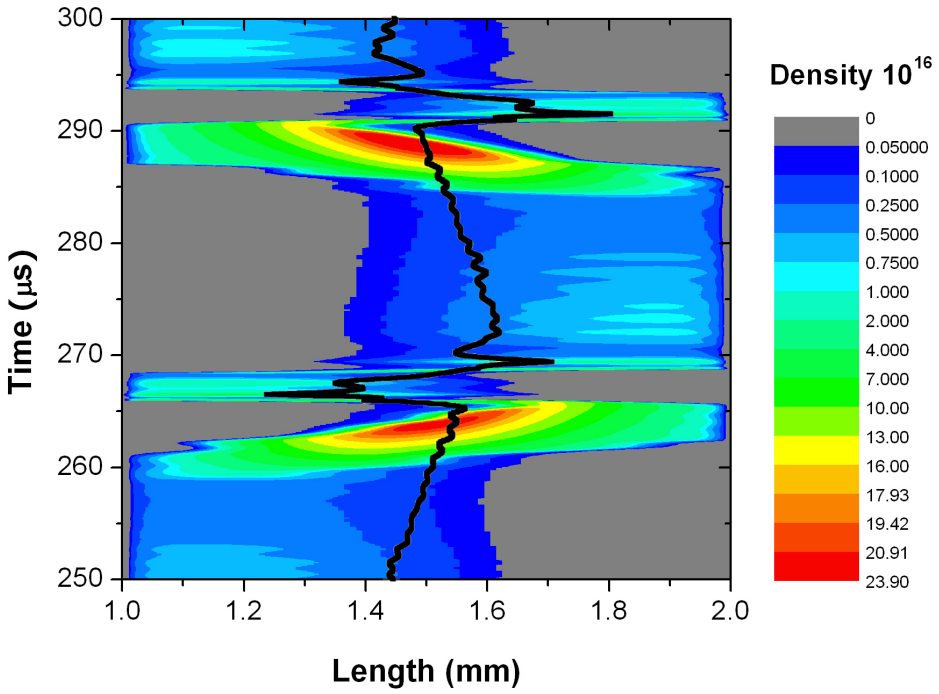

Figure 4.13: Phase diagram of electron number density distribution.

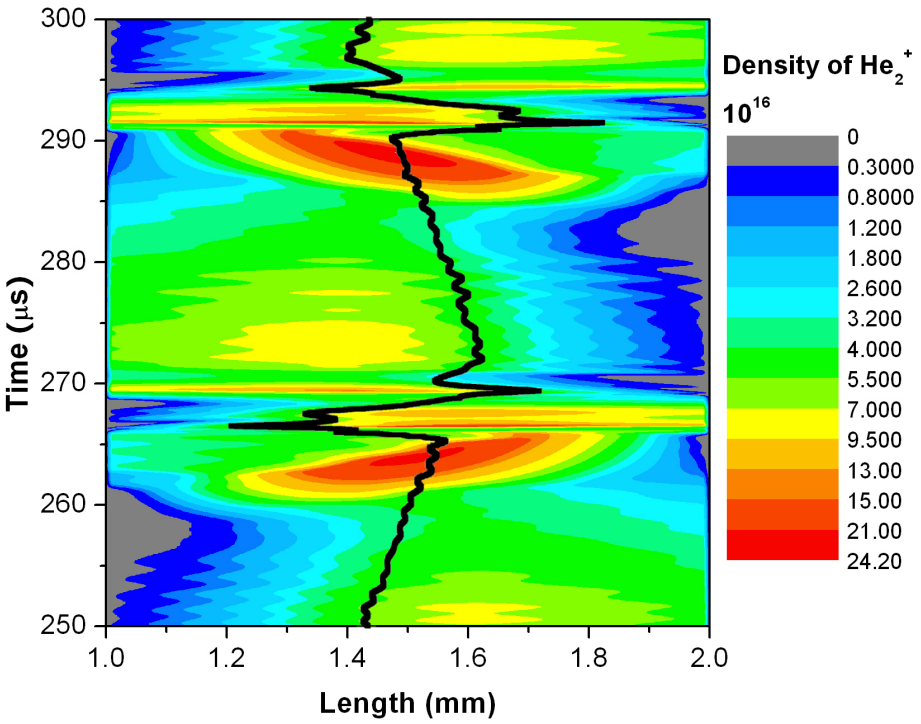

Figure 4.14: Phase diagram of He_2^+ number density distribution.

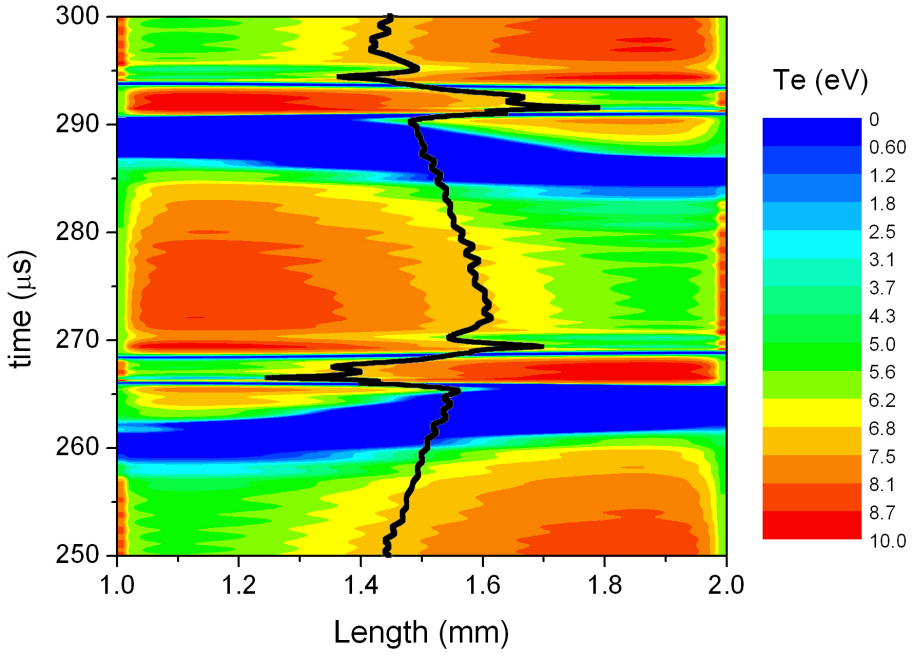

Figure 4.15: Phase diagram of electron temperature distribution.

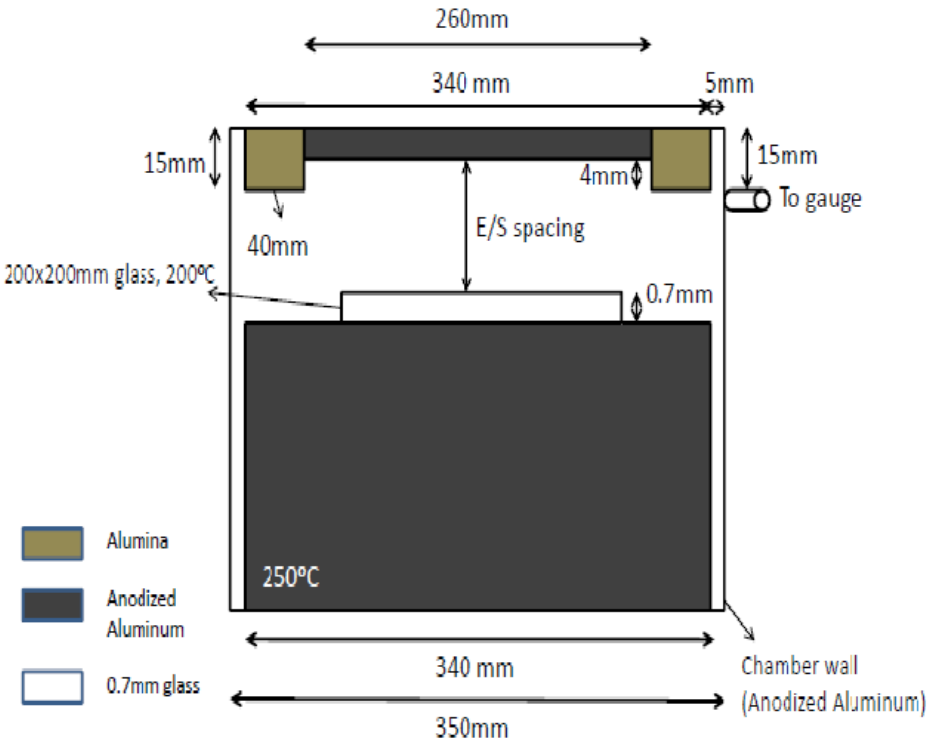

Figure 5.1: Sketch of the PECVD chamber

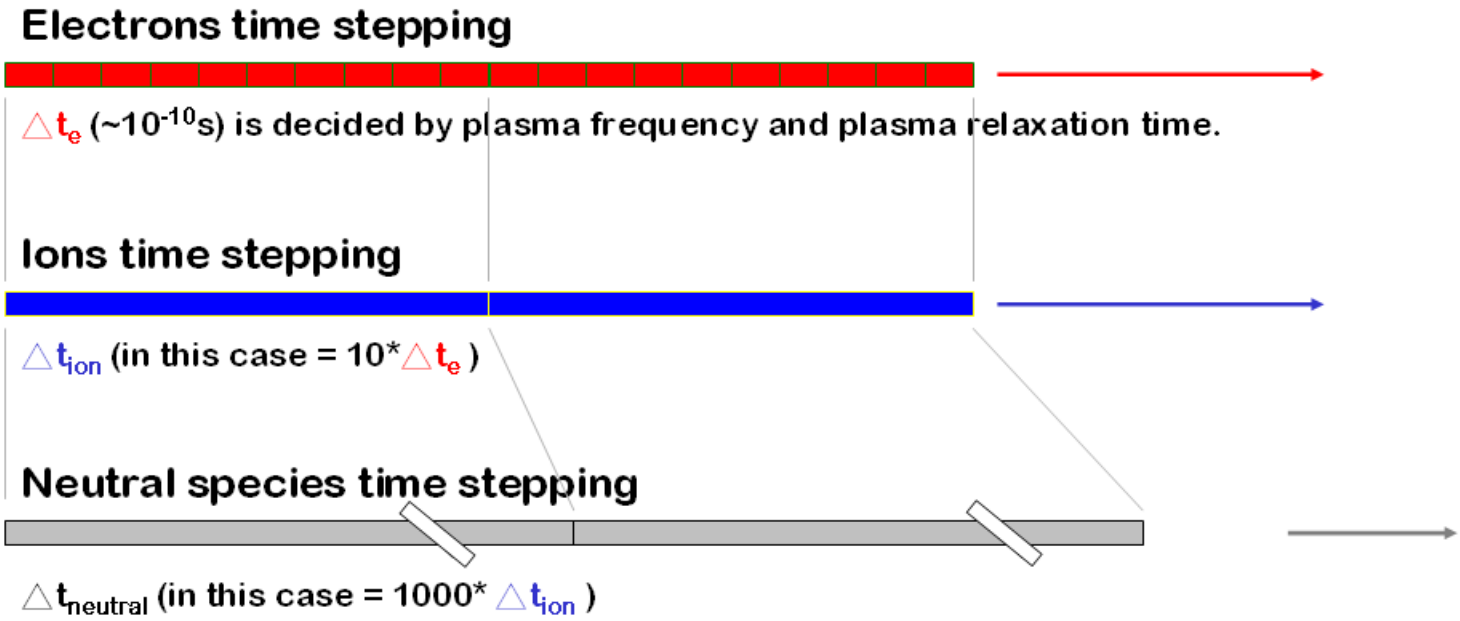

Figure 5.2: The sketch of special temporal marching scheme

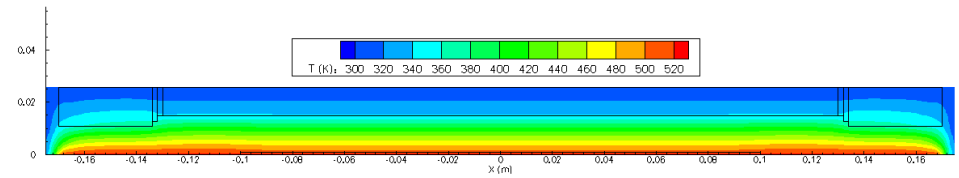

(a)

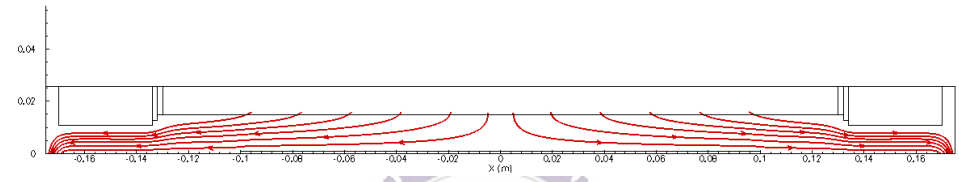

(b)

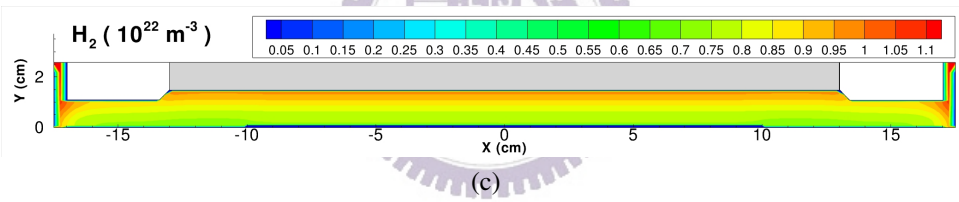

(c)

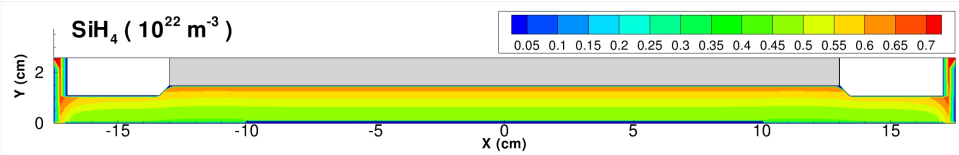

(d)

Figure 5.3: Fluid modeling initial conditions which are obtained form Navier-Stock equations solver include: (a) Gas temperature (b) Background gas flow velocity (c) H2 density distribution and (d) SiH4 density distribution.

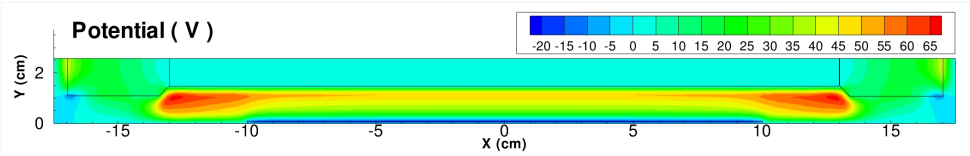

(a)

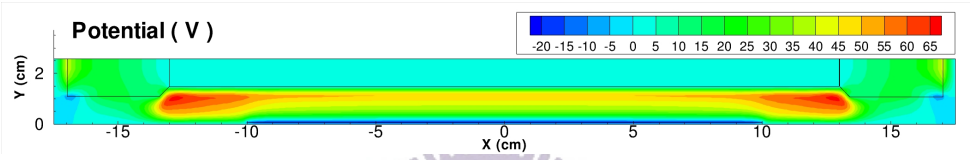

(b)

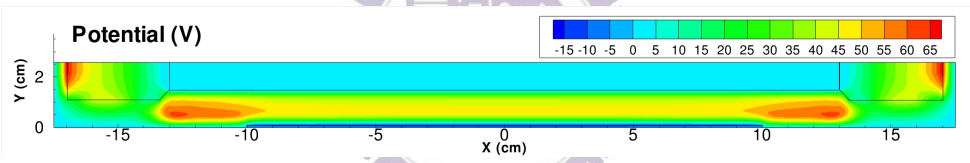

(c)

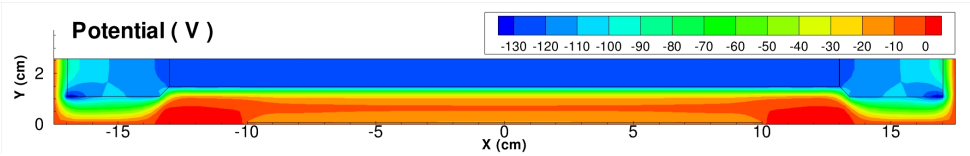

(d)

Figure 5.4: Plasma potential at difference phase of a RF cycle, where (a) $\phi = 0$ (b) $\phi = 0.5\pi$, $\phi = 1.5\pi$ and (d) $\phi = 2\pi$.

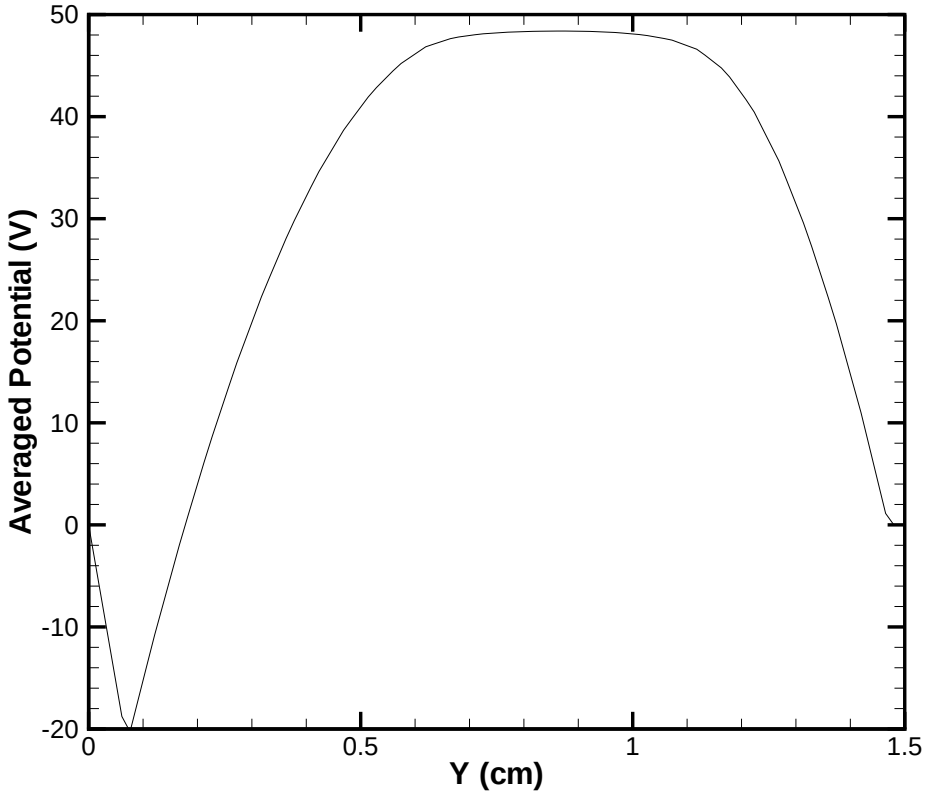

Figure 5.5: Cycle averaged potential profile across the electrode gap at the center of the chamber.

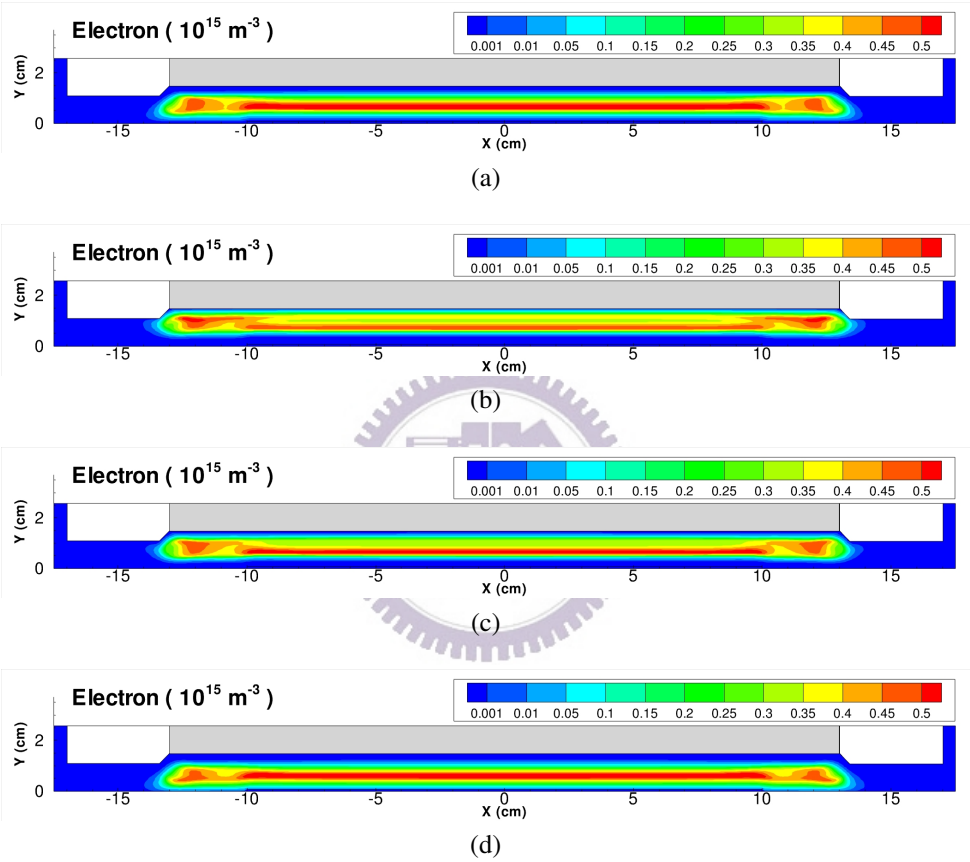

Figure 5.6: Electron density at difference phase of a RF cycle, where (a) $\phi = 0$ (b) $\phi = 0.5\pi$, $\phi = 1.5\pi$ and (d) $\phi = 2\pi$.

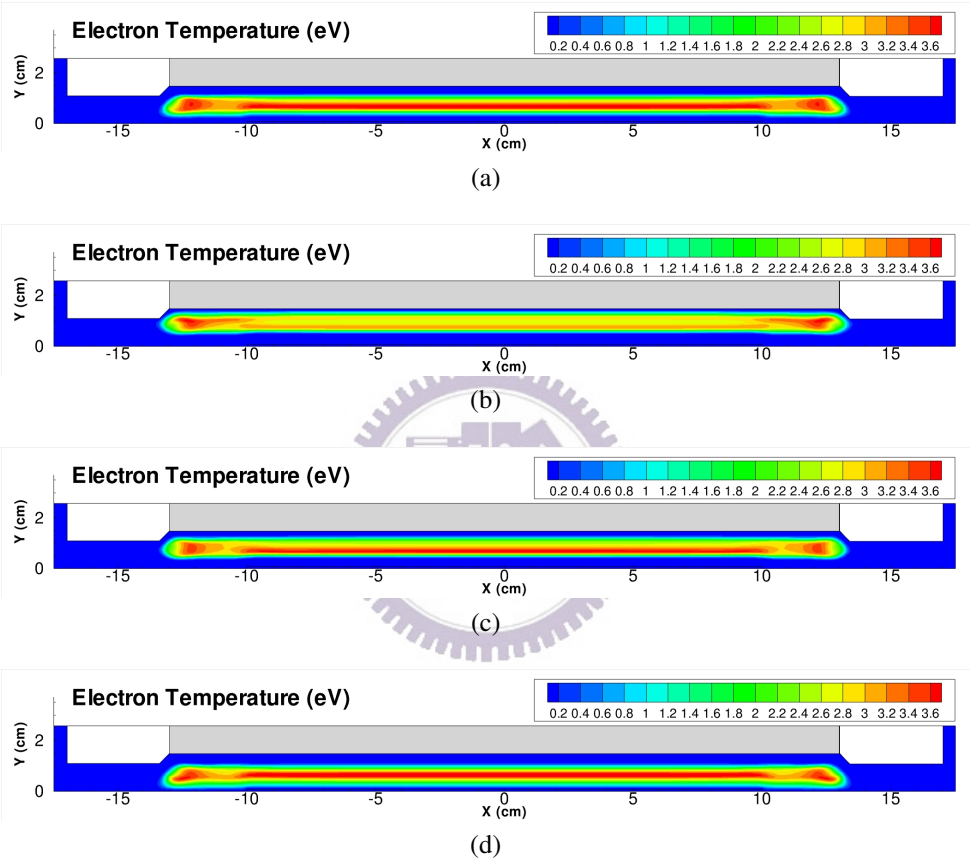

Figure 5.7: Electron temperature at difference phase of a RF cycle, where (a) $\phi = 0$ (b) $\phi = 0.5\pi$, $\phi = 1.5\pi$ and (d) $\phi = 2\pi$.

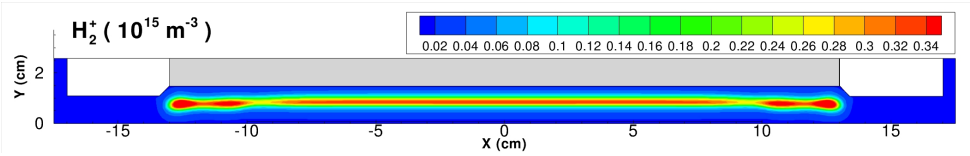

(a)

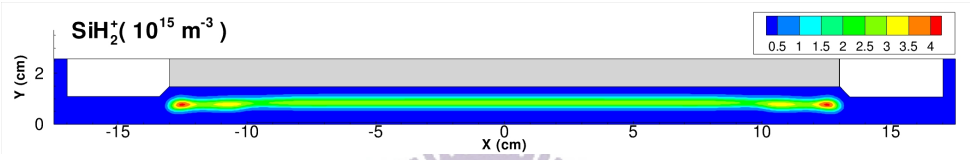

(b)

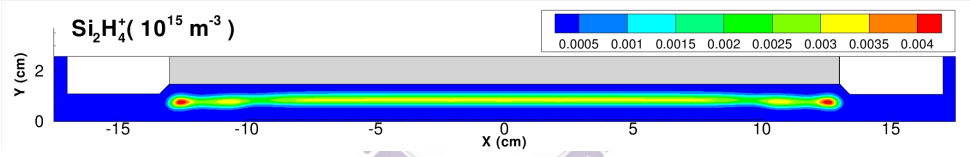

(c)

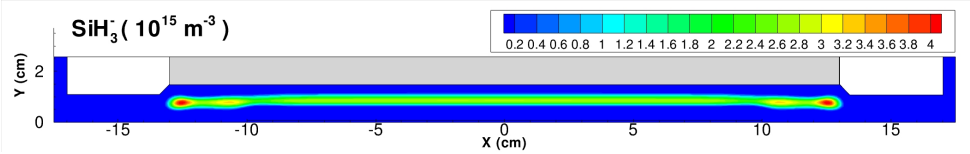

(d)

Figure 5.8: Ion species distributions include positive ions (a) H_2^+ (b) SiH_2^+ (c) $Si_2H_4^+$ and negative ion (d) SiH_3^-.

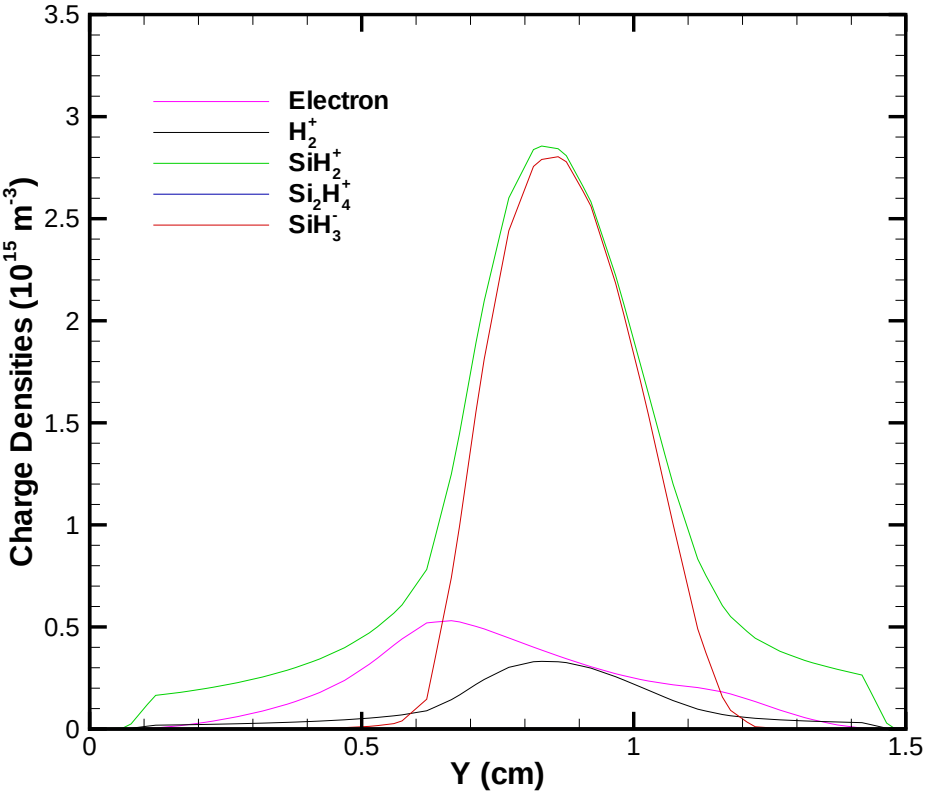

Figure 5.9: Cycle averaged charged densities profile across the electrode gap at the center of the chamber.

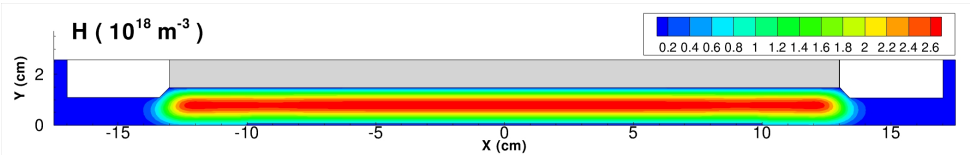

(a)

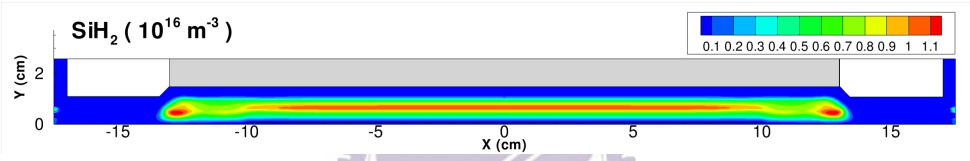

(b)

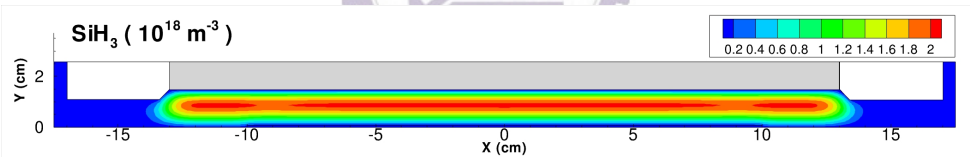

(c)

Figure 5.10: Important radical species relate to s-Si deposition, include(a) H(b) SiH_2 and (c) SiH_3.

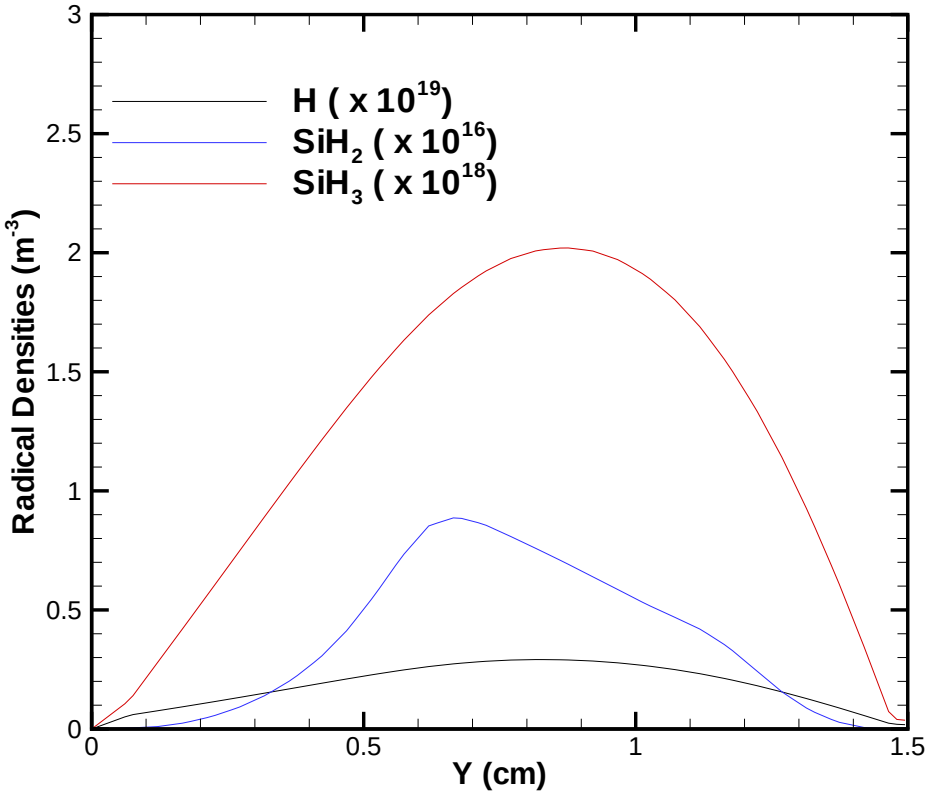

Figure 5.11: Cycle averaged radical densities profile across the electrode gap at the center of the chamber.

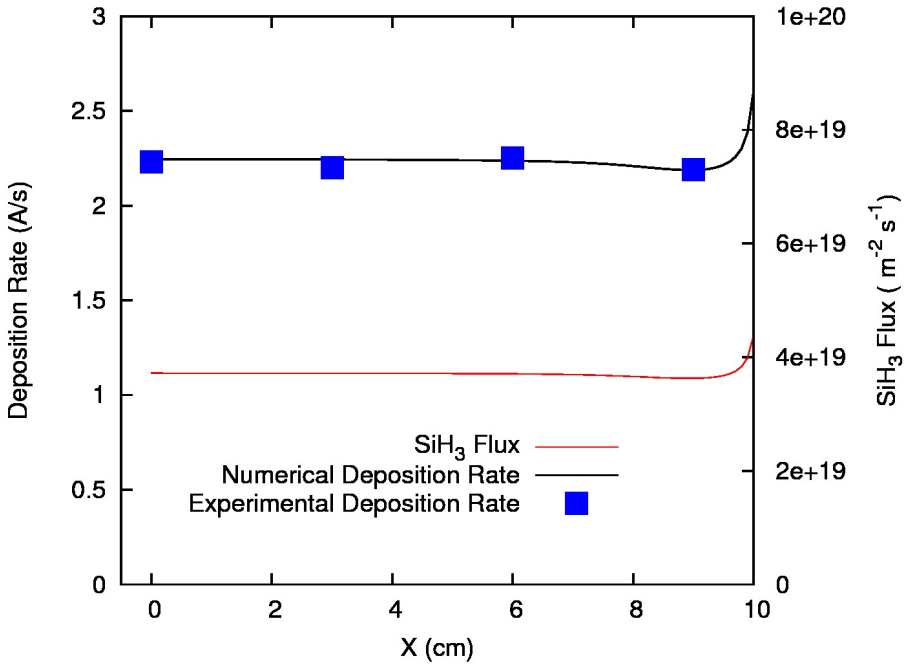

Figure 5.12: Comparison of deposition rate from numerical simulation and experiment data as well as SiH_3 flux to the subtract glass.

Table 3.1: Nitrogen plasma chemistry reaction channels.

No.	Reaction Channel	Threshold Energy (eV)	Rate Coefficient
1	$e + N_2 \rightarrow e + N_2$	0.00	cross section
2	$e + N_2 \rightarrow 2e + N_2^+$	15.58	cross section
3	$e + N_2 \rightarrow e + N_2(rot)$	0.02	cross section
4	$e + N_2 \rightarrow e + N_2(res)$	0.29	cross section
5	$e + N_2 \rightarrow e + N_2(v = 1)$	0.29	cross section
6	$e + N_2 \rightarrow e + N_2(v = 2)$	0.59	cross section
7	$e + N_2 \rightarrow e + N_2(v = 3)$	0.88	cross section
8	$e + N_2 \rightarrow e + N_2(v = 4)$	1.17	cross section
9	$e + N_2 \rightarrow e + N_2(v = 5)$	1.47	cross section
10	$e + N_2 \rightarrow e + N_2(v = 6)$	1.76	cross section
11	$e + N_2 \rightarrow e + N_2(v = 7)$	2.06	cross section
12	$e + N_2 \rightarrow e + N_2(v = 8)$	2.35	cross section
13	$e + N_2 \rightarrow e + N_2(A^3\Sigma_u^+)$	6.17	cross section
14	$e + N_2 \rightarrow e + N_2(B^3\Pi_g)$	7.35	cross section
15	$e + N_2 \rightarrow e + N_2(a'^1\Sigma_u^-)$	8.40	cross section
16	$e + N_2 \rightarrow e + N_2(C^3\Pi_u)$	11.03	cross section
17	$e + N_2^+ \rightarrow N_2$	0.0	$2.8 \times 10^{-13} (T_g/T_e)^{0.5}\, m^3 s^{-1}$
18	$e + N_4^+ \rightarrow N_2(C^3\Pi_u) + N_2$	0.0	$2.0 \times 10^{-12} (T_g/T_e)^{0.5}\, m^3 s^{-1}$
19	$N_2(vib) + N_2 \rightarrow 2N_2$	0.0	$1.0 \times 10^{-18} m^3 s^{-1}$
20	$N_2(a'^1\Sigma_u^-) + N_2(A^3\Sigma_u^+) \rightarrow e + N_4^+$	0.0	$5.0 \times 10^{-17} m^3 s^{-1}$
21	$N_2(a'^1\Sigma_u^-) + N_2(a'^1\Sigma_u^-) \rightarrow e + N_4^+$	0.0	$2.0 \times 10^{-16} m^3 s^{-1}$
22	$N_2(a'^1\Sigma_u^-) + N_2 \rightarrow 2N_2$	0.0	$2.0 \times 10^{-19} m^3 s^{-1}$
23	$N_2(a'^1\Sigma_u^-) + N_2 \rightarrow N_2(B^3\Pi_g) + N_2$	0.0	$2.0 \times 10^{-19} m^3 s^{-1}$
24	$N_2(A^3\Sigma_u^+) + N_2(A^3\Sigma_u^+) \rightarrow N_2 + N_2(C^3\Pi_u)$	0.0	$3.0 \times 10^{-16} m^3 s^{-1}$
25	$N_2(A^3\Sigma_u^+) + N_2(A^3\Sigma_u^+) \rightarrow N_2 + N_2(B^3\Pi_g)$	0.0	$7.7 \times 10^{-17} m^3 s^{-1}$
26	$N_2(C^3\Pi_u) + N_2 \rightarrow N_2(a'^1\Sigma_u^-) + N_2$	0.0	$1.0 \times 10^{-17} m^3 s^{-1}$
27	$N_2(B^3\Pi_g) + N_2 \rightarrow N_2(A^3\Sigma_u^+) + N_2$	0.0	$5.0 \times 10^{-17} m^3 s^{-1}$
28	$N_2(a'^1\Sigma_u^-) \rightarrow N_2 + h\nu 177nm$	0.0	$1.0 \times 10^2 s^{-1}$
29	$N_2(A^3\Sigma_u^+) \rightarrow N_2 + h\nu 293nm$	0.0	$5.0 \times 10^{-1} s^{-1}$
30	$N_2(B^3\Pi_g) \rightarrow N_2(A^3\Sigma_u^+) + h\nu 1045nm$	0.0	$1.5 \times 10^5 s^{-1}$
31	$N_2(C^3\Pi_u) \rightarrow N_2(B^3\Pi_g) + h\nu 336nm$	0.0	$2.7 \times 10^7 s^{-1}$

Table 4.1: Summary of simple and complicated helium plasma chemistry.

No	Reaction Type	Reaction Channels	Complicated	Simple	Threshold Energy(eV)
00	Momentum transfer	$e^- + He \rightarrow e^- + He$	BOLSIG+	BOLSIG+	0
01	e-impact excitation (2S)	$e^- + He \rightarrow e^- + He^*_{meta}\,(^3S_1)$	BOLSIG+	$2.308 \times 10^{-16} T_e^{0.31} exp(\frac{-2.297 \times 10^5}{T_e})$	19.82
02	e-impact excitation (2S)	$e^- + He \rightarrow e^- + He^*_{meta}\,(^1S_1)$	BOLSIG+		20.61
03	e-impact excitation (23P)	$e^- + He \rightarrow e^- + He^{**}\,(23P)$	BOLSIG+		0
04	e-impact excitation (21P)	$e^- + He \rightarrow e^- + He^{**}\,(21P)$	BOLSIG+		0
05	e-impact excitation (3SPD)	$e^- + He \rightarrow e^- + He^{**}\,(3SPD)$	BOLSIG+		0
06	e-impact excitation (4SPD)	$e^- + He \rightarrow e^- + He^{**}\,(4SPD)$	BOLSIG+		0
07	e-impact excitation (5SPD)	$e^- + He \rightarrow e^- + He^{**}\,(5SPD)$	BOLSIG+		0
08	e-impact ionization	$e^- + He \rightarrow 2e^- + He^+$	BOLSIG+	$2.584 \times 10^{-18} T_e^{0.68} exp(\frac{-2.854 \times 10^5}{T_e})$	24.58
09	e-impact ionization	$e^- + He^*_{meta} \rightarrow 2e^- + He^+$	BOLSIG+	$4.611 \times 10^{-16} T_e^{0.6} exp(\frac{-5.546 \times 10^4}{T_e})$	4.78
10	e-impact de-excitation	$e^- + He^*_{meta} \rightarrow e^- + He$	2.9×10^{-15}	$1.099 \times 10^{-17} T_e^{0.31}$	-19.8
11	e-impact dissociation	$e^- + He^*_2 \rightarrow e^- + 2He$	3.8×10^{-15}	$1.268 \times 10^{-18} T_e^{0.71} exp(\frac{-3.945 \times 10^4}{T_e})$	-17.9
12	e-ion recombination	$2e^- + He^+ \rightarrow e^- + He^*_{meta}$	6×10^{-32}		-4.78
13	e-ion dissociative recombination	$2e^- + He^+_2 \rightarrow e^- + He^*_{meta} + He$	2.8×10^{-32}	$5.386 \times 10^{-13} T_e^{-0.5}$	0
14	e-ion dissociative recombination	$e^- + He^+_2 + He \rightarrow He^*_{meta} + 2He$	3.5×10^{-39}		0
15	e-ion recombination	$2e^- + He^+_2 \rightarrow e^- + He^*_2$	1.2×10^{-33}		0
16	e-ion recombination	$e^- + He^+_2 + He \rightarrow He^*_2 + He$	1.5×10^{-39}		0
17	Hombeck-Molnar associative ionization	$He^{**} + He \rightarrow e^- + He^+_2$	1.5×10^{-17}		0
18	Metastable-metastable associative ionization	$He^*_{meta} + He^*_{meta} \rightarrow e^- + He^+_2$	2.03×10^{-15}		-18.2
19	Metastable-metastable ionization	$He^*_{meta} + He^*_{meta} \rightarrow e^- + He^+ + He$	8.7×10^{-16}	2.7×10^{-16}	-15.8
20	ion conversion	$He^+ + 2He \rightarrow He^+_2 + He$	6.5×10^{-44}	$2.584 \times 10^{-18} T_e^{0.68} exp(\frac{1 \times 10^{45}}{T_e})$	0
21	Metastable-induced association	$He^*_{meta} + 2He \rightarrow He^*_2 + He$	1.9×10^{-46}	1.3×10^{-45}	0
22	Metastable-induced dissociative ionization	$He^*_{meta} + He^*_2 \rightarrow e^- + He^+ + 2He$	5×10^{-16}		-13.5
23	Metastable-induced ionization	$He^*_{meta} + He^*_2 \rightarrow e^- + He^+_2 + He$	2×10^{-15}		-15.9
24	Dimer-induced dissociative ionization	$He^*_2 + He^*_2 \rightarrow e^- + He^+ + 3He$	3×10^{-16}		-11.3
25	Dimer-induced ionization	$He^*_2 + He^*_2 \rightarrow e^- + He^+_2 + 2He$	1.2×10^{-15}		-13.7
26	He-atom induced dissociation	$He^*_2 + He \rightarrow 3He$	4.9×10^{-22}		0

Table 5.1: Silane/Hydrogen plasma chemistry reaction channels.

No.	Reaction	Rate Coefficient	Threshold Energy(eV)
01	$SiH_4 + e^- \rightarrow SiH_2^+ + 2H + 2e^-$	cross section	11.9
02	$Si_2H_6 + e^- \rightarrow Si_2H_4^+ + 2H + 2e^-$	cross section	10.2
03	$SiH_4 + e^- \rightarrow SiH_4^{(1\sim3)} + e^- \rightarrow SiH_4 + e^-$	cross section	0.11
04	$SiH_4 + e^- \rightarrow SiH_4^{(2\sim4)} + e^- \rightarrow SiH_4 + e^-$	cross section	0.27
05	$SiH_4 + e^- \rightarrow SiH_3 + H + e^-$	cross section	8.3
06	$SiH_4 + e^- \rightarrow SiH_2 + 2H + e^-$	cross section	8.3
07	$Si_2H_6 + e^- \rightarrow SiH_3 + SiH_2 + H$	cross section	7.0
08	$SiH_4 + e^- \rightarrow SiH_3^- + H$	cross section	
09	$H_2 + e^- \rightarrow H_2^+ + 2e^-$	cross section	15.4
10	$H_2^{(v=0)} + e^- \rightarrow H_2^{(v\neq0)} + e^- \rightarrow H_2^{(v=0)} + e^-$	cross section	0.54
11	$H_2^{(v=0)} + e^- \rightarrow H_2^{(v\neq0)} + e^- \rightarrow H_2^{(v=0)} + e^-$	cross section	1.08
12	$H_2^{(v=0)} + e^- \rightarrow H_2^{(v\neq0)} + e^- \rightarrow H_2^{(v=0)} + e^-$	cross section	1.62
13	$H_2 + e^- \rightarrow H + H + e^-$	cross section	8.9
14	$H + SiH_4 \rightarrow SiH_3 + H_2$	$3.39e^{-19}$	
15	$H + Si_2H_6 \rightarrow Si_2H_5 + H_2$	$1.38e^{-18}$	
16	$H+ Si_2H_6 \rightarrow SiH_3 + SiH_4$	$1.11e^{-18}$	
17	$H + Si_nH_{2n+2} \rightarrow Si_nH_{2n+1} + H_2$	$2.4\times10^{-10}\times\exp(-1250/T_{gas})$	
18	$H_2 + SiH_2 \rightarrow SiH_4$	$3.2\times e^{-18}$	
19	$SiH_2 + SiH_4 \rightarrow Si_2H_6$	$5.45\times e^{-16}$	
20	$SiH_2 + Si_2H_6 \rightarrow Si_3H_8$	$6.6\times e^{-16}$	
21	$SiH_2 + Si_nH_{2n+2} \rightarrow Si_{n+1}H_{2n+4}$	$4.2\times10^{-10}\times[1-(1+0.0033p_0)^{-1}]$	
22	$SiH_3 + SiH_3 \rightarrow SiH_4 + SiH_2$	$1.5\times e^{-16}$	
23	$SiH_3^- + SiH_2^+ \rightarrow SiH_3 + SiH_2$	$1.2\times e^{-13}$	
24	$SiH_3^- + Si_2H_4^+ \rightarrow SiH_3 + 2SiH_2$	$1.0\times e^{-13}$	
25	$SiH_3^- + H_2^+ \rightarrow SiH_3 + H_2$	$4.8\times e^{-13}$	
26	$Si_2H_5 + Si_2H_5 \rightarrow Si_4H_{10}$	$1.5\times e^{-16}$	

Reference

Balay, Satish, Gropp, William D., McInnes, Lois C., and Smith, Barry F. "PETSc home page.", 2001. http://www.mcs.anl.gov/petsc.

Bartnikas, R., Radu, I., and Wertheimer, M.R. "Dielectric Electrode Surface Effects on Atmospheric Pressure Glow Discharges in Helium." *Plasma Science, IEEE Transactions on* 35, 5: (2007) 1437–1447. 10.1109/TPS.2007.902797.

Bhandarkar, U V, Swihart, M T, Girshick, S L, and Kortshagen, U R. "Modelling of silicon hydride clustering in a low-pressure silane plasma." *Journal of Physics D: Applied Physics* 33, 21: (2000) 2731. http://stacks.iop.org/0022-3727/33/i=21/a=311.

Birdsall, CK, and Langdon. *Plasma Physics via Computer Simulation (Series on Plasma Physics)*. Taylor & Francis, 1991. http://www.amazon.ca/exec/obidos/redirect?tag=citeulike09-20&path=ASIN/0750301171.

Bleecker, K. De, Bogaerts, A., Goedheer, W., and Gijbels, R. "Investigation of growth mechanisms of clusters in a silane discharge with the use of a fluid model." *Plasma Science, IEEE Transactions on* 32, 2: (2004a) 691–698. 10.1109/TPS.2004.826095.

Bleecker, Kathleen De, Bogaerts, Annemie, Gijbels, Renaat, and Goedheer, Wim. "Numerical investigation of particle formation mechanisms in silane discharges." *Physical Review E* 69, 5: (2004b) 056,409. http://link.aps.org/doi/10.1103/PhysRevE.69.056409.

Boltzmann, Ludwig. *Sitzungsberichte der Akademie der Wissenschaften , Wien , II* 66: (1872) 275.

Bukowski, J. D., Graves, D. B., and Vitello, P. "Two-dimensional fluid model of an inductively coupled plasma with comparison to experimental spatial profiles." *Journal of Applied Physics* 80, 5: (1996) 2614. http://link.aip.org/link/JAPIAU/v80/i5/p2614/s1&Agg=doi.

Cai, Xiao-chuan, Casarin, Mario A., Elliott, Frank W., and Widlund, Olof B. "Overlapping Schwarz algorithms for solving Helmholtz's equation." In *Contemporary Mathematics*. American Mathematical Society, 1998a, 391–399.

———. "Overlapping Schwarz algorithms for solving Helmholtz's equation." In *Contemporary Mathematics*. American Mathematical Society, 1998b, 391–399.

Cai, Xiao-chuan, Gropp, William D., and Keyes, David E. "A comparison of some domain decomposition and ILU preconditioned iterative methods for nonsymmetric elliptic problems." In *in Fifth International Symposium on Domain Decomposition Methods for Partial Differential Equations*. 1994, 477–504.

Chirokov, A, Khot, S N, Gangoli, S P, Fridman, A, Henderson, P, Gutsol, A F, and Dolgopolsky, A. "Numerical and experimental investigation of the stability of radio-frequency (RF) discharges at atmospheric pressure." *Plasma Sources Science and Technology* 18, 2: (2009) 025,025. http://iopscience.iop.org/0963-0252/18/2/025025.

Choi, Y.H., Kim, J.H., and Hwang, Y.S. "One-dimensional discharge simulation of nitrogen DBD atmospheric pressure plasma." *Thin Solid Films* 506-507: (2006) 389–395. http://www.sciencedirect.com/science/article/B6TW0-4H2PJDV-8/2/a9b909fa527abb5b848a2c447d2594fb.

van Dijk, Jan, Peerenboom, Kim, Jimenez, Manuel, Mihailova, Diana, and van der Mullen, Joost. "The plasma modelling toolkit Plasimo." *Journal of Physics D: Applied Physics* 42, 19: (2009) 194,012. http://iopscience.iop.org/0022-3727/42/19/194012.

FumiyoshiTochikubo, TakumaChiba, and TsuneoWatanabe. "Structure of Low-Frequency Helium Glow Discharge at Atmospheric Pressure between Parallel Plate Dielectric Electrodes." *Japanese Journal of Applied Physics* 38: (1999) 5244–5250. http://jjap.ipap.jp/link?JJAP/38/5244/.

Gallagher, Alan. "Model of particle growth in silane discharges." *Physical Review E* 62, 2: (2000) 2690. http://link.aps.org/doi/10.1103/PhysRevE.62.2690.

Gogolides, Evangelos, and Sawin, Herbert H. "Continuum modeling of radio-frequency glow discharges. I. Theory and results for electropositive and electronegative gases." *Journal of Applied Physics* 72, 9: (1992) 3971–3987. http://link.aip.org/link/?JAP/72/3971/1.

Golubovskii, Yu B, Maiorov, V A, Behnke, J, and Behnke, J F. "Modelling of the homogeneous barrier discharge in helium at atmospheric pressure." *Journal of Physics D: Applied Physics* 36, 1: (2003) 39–49. http://iopscience.iop.org/0022-3727/36/1/306.

Grubert, G. K., Becker, M. M., and Loffhagen, D. "Why the local-mean-energy approximation should be used in hydrodynamic plasma descriptions instead of the local-field approximation." *Physical Review E* 80, 3: (2009) 036,405. http://link.aps.org/doi/10.1103/PhysRevE.80.036405.

Hagelaar, Gerjan. "BOLSIG+ : user-friendly solver for electron Boltzmann equation.", 2009. http://www.laplace.univ-tlse.fr/groupes-de-recherche/groupe-de-recherche-energetique/projets-en-cours/bolsig-resolution-de-l-equation-de/article/bolsig-resolution-de-l-equation-de?lang=fr.

Hu, Meng-Hua. personal communication, 2010.

Hwang, Feng-Nan, and Cai, Xiao-Chuan. "A parallel nonlinear additive Schwarz preconditioned inexact Newton algorithm for incompressible Navier-Stokes equations." *J. Comput. Phys.* 204, 2: (2005) 666–691.

Jung, Mi-Hee, and Choi, Ho-Suk. "Surface treatment and characterization of ITO thin films using atmospheric pressure plasma for organic light emitting diodes." *Journal of Colloid and Interface Science* 310, 2: (2007) 550–558. http://www.sciencedirect.com/science/article/B6WHR-4N1T1S4-B/2/8d37a2614096bbbaac14d98b8022b287.

Kanazawa, S, Kogoma, M, Moriwaki, T, and Okazaki, S. "Stable glow plasma at atmospheric pressure." *Journal of Physics D: Applied Physics* 21, 5: (1988) 838. http://stacks.iop.org/0022-3727/21/i=5/a=028.

Kim, HS, Kang, WS, Kim, GH, and Hong, SH. "Plasma Flow Characteristics in a Spray-Type Dielectric Barrier Discharge Reactor." *IEEE TRANSACTIONS ON PLASMA SCIENCE* 37, 6: (2009) 773–784. http://apps.isiknowledge.com/full_record.do?product=WOS&colname=WOS&search_mode=CitingArticles&qid=49&SID=S1FfG8I@ee3dipihlE9&page=1&doc=5.

Kolobov, VI, and Arslanbekov, RR. "Simulation of electron kinetics in gas discharges." *IEEE TRANSACTIONS ON PLASMA SCIENCE* 34, 3: (2006) 895–909. http://apps.isiknowledge.com/full_record.do?product=WOS&search_mode=GeneralSearch&qid=3&SID=S1FfG8I@ee3dipihlE9&page=8&doc=71.

Kushner, Mark J. "Hybrid modelling of low temperature plasmas for fundamental investigations and equipment design." *Journal of Physics D: Applied Physics* 42, 19: (2009) 194,013. http://iopscience.iop.org/0022-3727/42/19/194013.

Lieberman, Michael A., and Lichtenberg, Allan J. *Principles of Plasma Discharges and Materials Processing*. Wiley-Interscience, 1994, 1 edition.

Lin, Ming-Chang. personal communication, 2010.

Lymberopoulos, D.P., and Economou, D.J. "Two-dimensional simulation of polysilicon etching with chlorine in a high density plasma reactor." *Plasma Science, IEEE Transactions on* 23, 4: (1995) 573–580. 10.1109/27.467977.

Mangolini, L, Anderson, C, Heberlein, J, and Kortshagen, U. "Effects of current limitation through the dielectric in atmospheric pressure glows in helium." *Journal of Physics D: Applied Physics* 37, 7: (2004) 1021–1030. http://iopscience.iop.org/0022-3727/37/7/012.

Martens, T., Bogaerts, A., Brok, W. J. M., and van der Mullen, J. J. A. M. "Modeling study on the influence of the pressure on a dielectric barrier discharge microplasma." *Journal of Analytical Atomic Spectrometry* 22, 9: (2007a) 1033–1042. http://dx.doi.org/10.1039/b704903j.

Martens, Tom, Bogaerts, Annemie, Brok, Wouter, and van Dijk, Jan. "Computer simulations of a dielectric barrier discharge used for analytical spectrometry." *Analytical and Bioanalytical Chemistry* 388, 8: (2007b) 1583–1594. http://dx.doi.org/10.1007/s00216-007-1269-0.

Massines, Francoise, Rabehi, Ahmed, Decomps, Philippe, Gadri, Rami Ben, Segur, Pierre, and Mayoux, Christian. "Experimental and theoretical study of a glow discharge at atmospheric pressure controlled by dielectric barrier." *Journal of Applied Physics* 83, 6: (1998) 2950. http://link.aip.org/link/JAPIAU/v83/i6/p2950/s1&Agg=doi.

Messmer, Peter, and Bruhwiler, David L. "A parallel electrostatic solver for the VORPAL code." *Computer Physics Communications* 164, 1-3: (2004) 118–121. http://www.sciencedirect.com/science/article/B6TJ5-4CX71G2-3/2/53b90ac363afd6f2d7ba3c3d7c58cd9d.

Meyyappan, M. *Computational Modeling in Semiconductor Processing*. Artech House Publishers, 1994.

Nienhuis, G. J. *Plasma models for silicon deposition*. Ph.D. thesis, Utrecht University, Nieuwegein, The Netherlands, 1998.

Nienhuis, G. J., Goedheer, W. J., Hamers, E. A. G., van Sark, W. G. J. H. M., and Bezemer, J. "A self-consistent fluid model for radio-frequency discharges in SiH[sub 4]–H[sub 2] compared to experiments." *Journal of Applied Physics* 82, 5: (1997) 2060. http://link.aip.org/link/JAPIAU/v82/i5/p2060/s1&Agg=doi.

Nieter, Chet, and Cary, John R. "VORPAL: a versatile plasma simulation code." *Journal of Computational Physics* 196, 2: (2004) 448–473. http://www.sciencedirect.com/science/article/B6WHY-4B954G3-1/2/675d7d4de2f99f1448034cb90ce46f8e.

Park, Jaeyoung, Henins, I., Herrmann, H. W., Selwyn, G. S., and Hicks, R. F. "Discharge phenomena of an atmospheric pressure radio-frequency capacitive plasma source." *Journal of Applied Physics* 89, 1: (2001) 20. http://link.aip.org/link/JAPIAU/v89/i1/p20/s1&Agg=doi.

Phelps, Arthur V., and Brown, Sanborn C. "Positive Ions in the Afterglow of a Low Pressure Helium Discharge." *Physical Review* 86, 1: (1952) 102. http://link.aps.org/doi/10.1103/PhysRev.86.102.

Pitaevskii, L. P., and Lifshitz, E.M. *Physical Kinetics: Volume 10*. Butterworth-Heinemann, 1981.

Riley, M. E., Greenberg, K. E., Hebner, G. A., and Drallos, P. "Theoretical and experimental study of low-temperature, capacitively coupled, radio-frequency helium plasmas." *Journal of Applied Physics* 75, 6: (1994) 2789. http://link.aip.org/link/JAPIAU/v75/i6/p2789/s1&Agg=doi.

Saad, Youcef, and Schultz, Martin H. "GMRES: a generalized minimal residual algorithm for solving nonsymmetric linear systems." *SIAM J. Sci. Stat. Comput.* 7, 3: (1986) 856–869.

Salabas, A, Gousset, G, and Alves, L L. "Two-dimensional fluid modelling of charged particle transport in radio-frequency capacitively coupled discharges." *Plasma Sources Science and Technology* 11, 4: (2002) 448–465. http://iopscience.iop.org/0963-0252/11/4/312.

Schade, K., Stahr, F., Kuske, J., Röhlecke, S., Steinke, O., Stephan, U., and Dekkers, H.F.W. "High temperature line electrode assembly for continuous substrate flow VHF PECVD." *Thin Solid Films* 502, 1-2: (2006) 59–62. http://www.sciencedirect.com/science/article/B6TW0-4HVDYJ1-2/2/7cf791c89774f442faf701bd5d8b1929.

Scharfetter, D.L., and Gummel, H.K. "Large-signal analysis of a silicon Read diode oscillator." *Electron Devices, IEEE Transactions on* 16, 1: (1969) 64–77.

Shang, Wanli, Wang, Dezhen, and Zhang, Yuantao. "Radio frequency atmospheric pressure glow discharge in α and γ modes between two coaxial electrodes." *Physics of Plasmas* 15, 9: (2008) 093,503. http://link.aip.org/link/PHPAEN/v15/i9/p093503/s1&Agg=doi.

Vahedi, V, DiPeso, G, Birdsall, C K, Lieberman, M A, and Rognlien, T D. "Capacitive RF discharges modelled by particle-in-cell Monte Carlo simulation. I. Analysis of numerical

techniques." *Plasma Sources Science and Technology* 2, 4: (1993) 261. http://stacks.iop.org/0963-0252/2/i=4/a=006.

Ventzek, Peter L. G., Sommerer, Timothy J., Hoekstra, Robert J., and Kushner, Mark J. "Twodimensional hybrid model of inductively coupled plasma sources for etching." *Applied Physics Letters* 10.1063/1.109963.

van der Vorst, H. A. "Bi-CGSTAB: A Fast and Smoothly Converging Variant of Bi-CG for the Solution of Nonsymmetric Linear Systems." *SIAM Journal on Scientific and Statistical Computing* 13, 2: (1992) 631–644. http://link.aip.org/link/?SCE/13/631/1.

Walsh, J. L., Shi, J. J., and Kong, M. G. "Contrasting characteristics of pulsed and sinusoidal cold atmospheric plasma jets." *Applied Physics Letters* 88: (2006) 1501. http://adsabs.harvard.edu/abs/2006ApPhL..88q1501W.

Wang, Qi, Sun, Jizhong, and Wang, Dezhen. "Numerical analysis of two homogeneous discharge modes at atmospheric pressure with a self-consistent model." *Physics of Plasmas* 16, 4: (2009) 043,503. http://link.aip.org/link/PHPAEN/v16/i4/p043503/s1&Agg=doi.

Wang, Qiang, Economou, Demetre J., and Donnelly, Vincent M. "Simulation of a direct current microplasma discharge in helium at atmospheric pressure." *Journal of Applied Physics* 100, 2: (2006) 023,301. http://link.aip.org/link/JAPIAU/v100/i2/p023301/s1&Agg=doi.

White, R D, Robson, R E, Schmidt, B, and Morrison, Michael A. "Is the classical two-term approximation of electron kinetic theory satisfactory for swarms and plasmas?" *Journal of Physics D: Applied Physics* 36, 24: (2003) 3125–3131. http://iopscience.iop.org/0022-3727/36/24/006.

Yuan, Xiaohui, and Raja, Laxminarayan L. "Role of trace impurities in large-volume noble gas atmospheric-pressure glow discharges." *Applied Physics Letters* 81, 5: (2002) 814. http://link.aip.org/link/APPLAB/v81/i5/p814/s1&Agg=doi.

Yuan, Xiaohui, and Raja, L.L. "Computational study of capacitively coupled high-pressure glow discharges in helium." *Plasma Science, IEEE Transactions on* 31, 4: (2003) 495–503. 10.1109/TPS.2003.815479.

List of Publications

Journals: (*corresponding author)

1. S. S. Liaw*, C. C. Yang, R. T. Liu, and **J. T. Hong**, "Turing model for the patterns of lady beetles", Phys. Rev. E, 64, 041909, 2001.

2. K.-H. Hsu, P.-Y. Chen, **C.-T. Hung**, L.-H. Chen and J.-S. Wu*, "Development of a parallel Poisson's equation solver with adaptive mesh refinement and its application in field emission prediction," **Computer Physics Communications**, Vol. 174, pp. 948-960, 2006.

3. P.-Y. Chen, K.-H. Hsu, Y.-L. Hsu, K.-W. Cheng, **C.-T. Hung**, J.-S. Wu* and J.-P. Yu, "Modeling of the integrated magnetic focusing and gated field-emission device with single carbon nanotube," **Journal of Vacuum Science and Technology-B**, Vol. 25, Issue 1, pp. 74-81, 2007. This article was selected for the **Virtual Journal of Nanoscale Science & Technology** - January 15, 2007, Volume 15, Issue 2. http://www.vjnano.org

4. J.-S. Wu*, K.-H. Hsu, F.-L. Li, **C.-T. Hung** and S.-Y. Jou, "Development of a parallelized 3D electrostatic PIC-FEM code and its applications," **Computer Physics Communications**, Vol. 177, pp. 98-101, 2007. (SCI)

5. **C.-T. Hung**, M.-H. Hu, J.-S. Wu* and F.-N. Hwang, "A New Paradigm for Solving Plasma Fluid Modeling Equations," **Computer Physics Communications**, Vol. 177, pp. 138-139, 2007. (SCI)

6. A. Aliat, **C.-T. Hung**, C.-J. Tsai and J.-S. Wu*, "Effect of Free Electrons on Nanoparticle Charging in a Wire-Tube Negative Corona Discharge", **Applied Physics Letter**, 93, 154103, 2008. This article was selected for the **Virtual Journal of Nanoscale Science & Technology** - October 27, 2008, Volume 18, Issue 17. http://www.vjnano.org

7. A. Aliat, **C.-T. Hung**, C.-J. Tsai and J.-S. Wu*, "Modelling Nanoparticle Charging in the Positive and Negative Direct Current Air Corona Chargers," **Journal of Physics D: Applied Physics**, Vol. 42 (2009), 125206 (10 pp).

8. **C.-T. Hung**, Y.-M. Chiu, F.-N. Hwang, J.-S. Wu*, "Development of a Parallel Implicit Solver of Fluid Modeling Equations for Gas Discharges," **Computer Physics Communications** (accepted on June 2, 2010).

9. Y.-M. Chiu, **C.-T. Hung**, F.-N. Hwang, M.-H. Chiang, J.-S. Wu*, S.-H. Chen, "Effect of Plasma Chemistry on the Simulation of Helium Atmospheric-Pressure Plasmas," **Computer Physics Communications** (accepted in June 2010).

10. K.-W. Cheng, **C.-T. Hung**, M.-H. Chiang, F.-N. Hwang, J.-S. Wu*, "One-dimensional Simulation of Nitrogen Dielectric Barrier Discharge Driven by a Quasi-Pulsed Power Source and Its Comparison with Experiments," **Computer Physics Communications** (accepted in June 2010).

11. Matthew R. Smith*, **Chieh-Tsan Hung**, Kun-Mo Lin, J.-S. Wu and Jen-Perng Yu, "Development of a semi-implicit fluid modeling code using finite-volume method based on Cartesian grids," **Computer Physics Communications** (accepted in June 2010).

12. M.R. Smith, K.-M. Lin, **C.-T. Hung**, Y.-S. Chen and J.-S. Wu*, "Development of an Improved Spatial Reconstruction Technique for the HLL Method and Its Applications," **Journal of Computational Physics** (under 2^{nd} review; resubmitted on July 5, submitted on February 27, 2010).

13. **C.-T. Hung**, Y.-M. Chiu, M.-H. Chiang, J.-S. Wu*, F.-N. Hwang, Y.-C. Wang and Shiaw-Huei Chen, "Investigation of Helium Dielectric Barrier Discharge Driven by a Realistic Distorted-Sinusoidal Voltage Power Source," **Plasma Chemistry and Plasma Processing** (submitted on April 27, 2010).

14. S.-Y. Jou, **C.-T. Hung**, Y.-M. Chiu, J.-S. Wu*, B.-Y. Wei, "Enhancement of VUV Emission from a Coaxial Xenon Excimer Ultraviolet Lamp Driven by Distorted Bipolar Square Voltages," **Plasma Sources Science and Technology** (submitted on May 13, 2010).

Invited Conference Papers:

1. **C.-T. Hung**, M.-H. Hu and J.-S. Wu*, "Fluid Modeling of a Plasma Backlight Source for

LCD Panel," **4th International Conference on Quantum Enginerring**, Tainan, TAIWAN, July 8, 2006. (invited paper & poster)

2. J.-S. Wu*, K.-H. Hsu, F.-L. Li, **C.-T. Hung** and S.-Y. Jou, "Development of a Parallelized 3D PIC-FEM Code and Its Applications," **Conference on Computational Physics**, Geongju, KOREA, August 28-September 1, 2006. (invited speech) (http://ccp2006.postech.edu/),

3. **C.-T. Hung**, M. H. Hu, Y. M. Chiu, K. M. Lin, Y. C. Wang, J. S. Wu*, and F. N. Hwang, "Non-Thermal Plasma Simulation Using Parallel 2D Fluid Modeling Code," **Workshop on High Performance Simulation of Physical Systems**, HPSPS'09, March 2-5 (2009), Kaohsiung, Taiwan. (invited speech)

International Conference Papers (include those which are invited papers in previous section): (*corresponding author)

1. J.-S. Wu*, K.-H. Hsu and **C.-T. Hung**, "On the Performance Improvement of a Pallelized 3-D PIC-FEM Code," **ICOPS-2006**, Traverse City, Michigan, USA, June 4-8, 2006.

2. **C.-T. Hung**, M.-H. Hu and J.-S. Wu*, "Fluid modeling of a plasma backlight source for LCD panel," **4thInternational Conference on Quantum Engineering Science**, pp. 53-56, Tainan, TAIWAN, July 8, 2006. (invited paper & poster)

3. J.-S. Wu*, K.-H. Hsu, F.-L. Li and **C.-T. Hung**, "Development of a Parallelized 3D PIC-FEM Code and Its Applications," **Conference on Computational Physics**, Geongju, KOREA, August 28-September 1, 2006 (invited speech).

4. **C.-T. Hung**, M.-H. Hu, J.-S. Wu* and F.-N. Hwang, "A New Paradigm for Solving Plasma Fluid Modeling Equations," **Conference on Computational Physics**, Geongju, KOREA, August 28-September 1, 2006.

5. K.-H. Hsu, **C.-T. Hung**, F.-L. Li and J.-S. Wu*, "Development of a Parallelized 3D PIC-FEM Code and Its Applications," **25th International Symposium on Rarefied Gas Dynamics**, St. Petersburg, RUSSIA, July 21-28, 2006.

6. Y.-L. Hsu, C.-H. Chiang, J.-S. Wu, Y.-M. Lee and **C.-T. Hung**, "MD Simulations of Collisions between Two Nanoscale Argon Droplets," **25th International Symposium on Rarefied Gas Dynamics**, St. Petersburg, RUSSIA, July 21-28, 2006.

7. **C.-T. Hung**, M.-H. Hu, Y.-M. Chiu, J.-S. Wu and F.-N. Hwang, "Development of a Parallel 2D Fluid Modeling Code for Non-thermal Plasma Simulations," **26th International Symposium on Rarefied Gas Dynamics**, July 21-25, 2008, Kyoto University, Kyoto, Japan.

8. A. Aliat, C.-J. Tsai, **C.-T. Hung** and J.-S. Wu, "Effect of Free Electrons on Nanoparticle Charging in a Negative Direct Current Corona Charger," **26th International Symposium on Rarefied Gas Dynamics**, July 21-25, 2008, Kyoto University, Kyoto, Japan.

9. **C.-T. Hung**, M.-H. Hu, Y.-M. Chiu, K.-M. Lin, Y.-C. Wang, and J.-S. Wu*, "Non-Thermal Plasma Simulation Using Parallel Fluid Modeling Code," **HPC-Asia 2009**, March 2-5 (2009), Kaohsiung, Taiwan. (Invited speaker).

10. **Chieh-Tsan Hung**, Feng-Nan Hwang, Yuan-Min Chiu and J.-S. Wu*, "Development of a Parallel Implicit Numerical Solver of Fluid Modeling Equations for Gas Discharges," **The Sixth Asia-Pacific International Symposium on the Basic and Application of Plasma Technology (APSPT-6)**, Hsinchu, Taiwan, December 14-16, 2009.

11. S.-Y. Jou, **C.-T. Hung**[1], Y.-M. Chiu, J.-S. Wu* and B.-Y. Wei, "Simulation of Excimer Ultraviolet (EUV) Emission from a Xenon Excimer Ultraviolet Lamp Using Pulsed Voltage Power," **The Sixth Asia-Pacific International Symposium on the Basic and Application of Plasma Technology (APSPT-6)**, Hsinchu, Taiwan, December 14-16, 2009.

12. **Chieh-Tsan Hung**, Yuan-Ming Chiu, Feng-Nan Hwang and J.-S. Wu*, "Development of an Implicit Solver of Fluid Modeling Equations for Gas Discharges," **Conference on Computational Physics (CCP) 2009**, Kaohsiung, Taiwan, December 15-19, 2009.

13. Matthew R. Smith*, **Chieh-Tsan Hung**, Kun-Mo Lin, J.-S. Wu and Jen-Perng Yu, "Development of a semi-implicit fluid modeling code using finite-volume method based on Cartesian grids," **Conference on Computational Physics (CCP) 2009**, Kaohsiung, Taiwan, December 15-19, 2009.

14. S.-Y. Jou, **C.-T. Hung**, Y.-M. Chiu, J.-S. Wu* and B.-Y. Wei, "Enhancement of VUV Emission from a Xenon Excimer Ultraviolet Lamp Using Pulsed Voltage Waveform," **Conference on Computational Physics (CCP) 2009**, Kaohsiung, Taiwan, December 15-19, 2009.

15. **Chieh-Tsan Hung**, Yuan-Ming Chiu, Yin-Chi Wang, Feng-Nan Hwang and J.-S. Wu*, "One-dimensional Simulation of Nitrogen Dielectric Barrier Discharge Driven by a Quasi-pulsed Power Source," **Conference on Computational Physics (CCP) 2009**, Kaohsiung, Taiwan, December 15-19, 2009.

16. M.-H. Hu, **C.-T. Hung**, J.-S. Wu*, Y.-S. Chen, J.-P. Yu, "Simulation of Helium Atmospheric-pressure Plasma Jet Impinging on a Flat Plate," **Conference on Computational Physics (CCP) 2009**, Kaohsiung, Taiwan, December 15-19, 2009.

17. Ying-Ming Chiu, **Chieh-Tsan Hung**, Feng-Nan Hwang, J.-S. Wu* and Shiaw-Huei Chen, "Effect of plasma chemistry on the simulation of helium atmospheric-pressure plasmas," **Conference on Computational Physics (CCP) 2009**, Kaohsiung, Taiwan, December 15-19, 2009.

18. **Chieh-Tsan Hung**, Jong-Shinn Wu*, Meng-Hua Hu, Yuan-Ming Chiu, Feng-Nan Hwang, "Development and Validation of a Parallel 1D/2D Fluid Modelling Code for Non-thermal Plasma Simulation," **The 22ndInternational Conference on Parallel Computational Fluid Dynamics**, Kaohsiung, Taiwan, May 17-21, 2010.

Thesis:

1. **Chieh-Tsan Hung**, "Development of a Parallelized Fluid Modeling Code and Its Applications in Low-temperature Plasmas," Ph.D. Dissertation, National Chiao Tung University, Hsinchu, Taiwan, 2010.

2. **Chieh-Tsan Hung**, "Numerical Simulation of Inductively Coupled Plasma Source Using Acetylene Gas," M.S. Dissertation, National Tsing Hua University, Hsinchu, Taiwan, 2004.